Microscopic conductivity and ultrafast photocurrents in chalcogenides from 2D to 3D and beyond

By

Kateryna Kushnir

A Dissertation

submitted to the faculty of the

WORCESTER POLYTECHNIC INSTITUTE

in partial fulfillment of the requirements for the

Degree of Doctor of Philosophy

in

Physics

June 2021

Dr. Lyubov V. Titova

Thesis Director

Dr. Douglas Petkie

Committee Member

Dr. Alex Zozulya

Committee Member

Dr. Ronald Grimm

External Committee Member

Dr. Pratap M. Rao

External Committee Member

Abstract

The subject of this thesis is the dynamics of charge carriers and optical excitations in semiconducting chalcogenides, specifically compounds that contain sulfur or selenium. Chalcogenides are fascinating, as they display a wide array of properties that are attractive for both solar energy conversion and optoelectronics. With band gaps in the visible and near infrared, they strongly absorb light in the visible range, resulting in the excitation of charge carriers with long lifetimes and high mobility. Some of these materials exhibit room temperature ferroelectricity and ferroelasticity, pronounced nonlinear optical effects, and topologically protected surface states. Their properties can be further tailored by their structure and dimensionality, from bulk, three-dimensional (3D) materials to nanocrystals and inherently two-dimensional (2D) van der Waals materials. 2D chalcogenides are particularly appealing, as they feature enhanced light-matter interactions due to reduced dielectric screening, confinements of charge carriers in individual layers, and no dangling bonds at their surfaces. They are flexible and can be deposited on a variety of substrates.

This thesis discusses photoexcited carrier dynamics in a number of 2D and 3D chalcogenides: GeS, GeSe, SnSe, SnS_2, PbS, Bi_2S_3, and $(Bi_{1-x}In_x)_2Se_3$. Of them, 2D GeSe and GeS have strongly anisotropic electronic and optical properties, owing to robust room temperature ferroelectric polarization in the layers. 2D $(Bi_{1-x}In_x)_2Se_3$ undergoes a transition from a topological to trivial band insulator behavior with the indium content increasing from zero to a few percent, and exhibits pronounced changes in its carrier density, mobility, and response to photoexcitation. Another 2D chalcogenide, SnS_2, was investigated as a possible photoanode material due to its high optical absorption and mobility. Additionally, we discovered that it also exhibits intriguing nonlinear effects upon photoexcitation that result in the emission of terahertz (THz) radiation. Finally, the polycrystalline (quasi-3D) chalcogenides PbS and Bi_2S_3 were investigated as photovoltaic and photodetector materials. Polycrystalline films

are easy to deposit and more cost effective for large scale manufacturing, but, unlike bulk single crystals, can suffer from deleterious effects of grain or domain boundary defects.

For all of these materials, their potential applications in photonic and optoelectronic devices require a detailed understanding of the optical excitation, microscopic photoconductivity, dynamics of optically injected charge carriers and photoexcitations, and their dependence on chemical structure and morphology. Relevant photophysical processes, such as free carrier absorption, carrier scattering, trapping, recombination, and interactions between the optically injected carriers and lattice vibrational modes, occur over sub-picosecond to nanoseconds time scales, and often have characteristic energies in the THz range (0.1 - 30 THz or 4 - 120 meV). The all-optical techniques in the THz spectroscopy toolbox use broadband, picosecond-duration, phase-stable THz pulses to probe the dynamics of low-energy excitations in materials and microscopic photoconductivity without a reliance on electrical contacts, and are therefore ideally suited for investigating photophysics in bulk as well as nanoscale systems.

In this thesis we have used three experimental THz spectroscopic approaches: 1) time domain THz spectroscopy, which probes intrinsic free carriers, low energy phonons, and other low energy excitations, 2) time-resolved THz spectroscopy, which measures microscopic transient photoconductivity following optical excitation, and 3) THz emission spectroscopy, which provides a window into nonlinear optical properties and ultrafast photocurrents. With these techniques, we have demonstrated generation of ultrafast shift currents, or bias-free bulk photovoltaic effects, in 2D GeSe and GeS. We have observed the scattering of optically excited carriers from bulk conduction band states into two distinct sets of high mobility topological surface states in 2D Bi_2Se_3, and showed that the dynamics of the photoexcited free carriers are affected by these twin domain boundaries and are sensitive to the disorder introduced by indium substitution in 2D $(Bi_{0.75}In_{0.25})_2Se_3$ and $(Bi_{0.50}In_{0.50})_2Se_3$. We have also characterized the lifetimes of free photoexcited carriers, their mobility, and their interactions with interfaces and boundaries in 2D SnS_2 and GeS, and in polycrystalline Bi_2S_3 and PbS. Our experiments

uncovered the dynamics of photoexcitation over sub-picosecond to nanosecond time scales, and revealed the relationship between structure and optoelectronic properties in studied 2D and 3D chalcogenide materials. We have set the stage for their applications in efficient photovoltaic, photoelectrochemical and optoelectronic devices.

To

my loving husband, Michael, and my parents, Tamara and Yurii, for their endless support and patience, and for never letting me give up.

Acknowledgments

I have had the pleasure of knowing and working with many people during my time at the Worcester Polytechnic Institute, all of whom I am indebted to.

I would like to express my deepest gratitude to my advisor, Lyubov Titova, for her guidance, support, and encouragement over the last five years. I have been lucky to have had her, not just as a supervisor, but as a person who expanded my mind to improve my scientific skills and taught me patience. I appreciate the way she made me work on my weaknesses and focus on my strengths.

I would also like to express my appreciation to my thesis committee members; Prof. Douglas Petkie, who listened to all my lab complaints and made a humongous effort to move our lab to a new building. Prof. Alex Zozulya, who taught me how to properly ask questions and find solutions. Prof. Pratap Rao, who trusted and encouraged my experimental inquiries and shared his lab with me. Prof. Ronald Grimm, who excited me every time he came into the lab with his crazy ideas and enthusiasm. I thank all of them for their guidance, valuable advice, encouraging words, and personal attention. They have been there for me from the very beginning and given me constant support.

Special thanks also to Dr. Teng Shi for the countless discussions about science and life, for her support as a lab mate and friend. Erika Colin for her kind support and lunch discussions. As well as all the undergraduate students with whom I have worked: Erin Morissette, Patrick Fitzgerald, Ryan Hanna, Andrew Mendizabal, Alexis Buzzell, Taylor Trottier, Benjamin Dringoli, Megan Varney, Shaniah Greene, Leticia Damian Melendez, Emma Burton, and others. I am very grateful to the new students that recently joined our lab and been very patient with me and very kind to agree to edit my thesis, Javery Mann and Andrew Fitzgerald. It was a huge pleasure to work with such amazing people.

I am also thankful for many great collaborations that resulted in good friends: Mariam

Masroor Shalmani, Binod Giri, Julia Martin, Deborah Oyewole and others. Thank you for your support and motivation to forge ahead in my research work.

Thank you to my parents Tamara and Yurii and my brother Mykolay for their love and support through my whole academic path. Without their efforts, encouragement, and sacrifices I would not be here. I have saved the last word for my dear and beloved husband, Michael, who has been my best friend and stood by my side in good and bad times during all these years, making them the best of my life. I am thankful for sharing my life with you. There are not enough words to express my heartfelt appreciation for always encouraging me to pursue my dreams. Your encouragement and support has provided me with strength to complete this task.

Contents

List of Figures

List of my Publications

[1] Zhehao Zhu, Satish Kumar Iyemperumal, **Kushnir, Kateryna**, Alexander D Carl, Lite Zhou, Drew R Brodeur, Ronald L Grimm, Lyubov V Titova, N Aaron Deskins, and Pratap M Rao. Enhancing the solar energy conversion efficiency of solution-deposited Bi_2S_3 thin films by annealing in sulfur vapor at elevated temperature. *Sustainable Energy & Fuels*, 1(10):2134–2144, 2017. 51, 63, 83, 127

[2] **Kushnir, Kateryna**, Mengjing Wang, Patrick D. Fitzgerald, Kristie J. Koski, and Lyubov V. Titova. Ultrafast zero-bias photocurrent in GeS nanosheets: Promise for photovoltaics. *ACS Energy Letters*, 2(6):1429–1434, 2017. 9, 45, 78, 106, 128, 129

[3] **Kushnir, Kateryna**, Kefan Chen, Lite Zhou, Binod Giri, Ronald L Grimm, Pratap M Rao, and Lyubov V Titova. Dynamics of photoexcited carriers in polycrystalline PbS and at PbS/ZnO heterojunctions: Influence of grain boundaries and interfaces. *The Journal of Physical Chemistry C*, 122(22):11682–11688, 2018. 51, 63, 127

[4] Guangjiang Li, **Kushnir, Kateryna**, Yongchang Dong, Sergii Chertopalov, Apparao M Rao, Vadym N Mochalin, Ramakrishna Podila, and Lyubov V Titova. Equilibrium and non-equilibrium free carrier dynamics in 2d $Ti_3C_2T_x$ mxenes: Thz spectroscopy study. *2D Materials*, 5(3):035043, 2018. 128

[5] **Kushnir, Kateryna**, Ying Qin, Yuxia Shen, Guangjiang Li, Benjamin M. Fregoso, Sefaattin Tongay, and Lyubov V. Titova. Ultrafast zero-bias surface photocurrent in germanium selenide: Promise for terahertz devices and photovoltaics. *ACS Applied Materials and Interfaces*, 11(5):5492–5498, 2019. 9, 106, 126

[6] Binod Giri, Maryam Masroor, Tao Yan, **Kushnir, Kateryna**, Alexander D Carl, Curtis Doiron, Haochuan Zhang, Yanyan Zhao, Arthur McClelland, Geoffrey A Tompsett,

et al. Balancing light absorption and charge transport in vertical SnS_2 nanoflake photoanodes with stepped layers and large intrinsic mobility. *Advanced Energy Materials*, 9(31):1901236, 2019. 51, 69, 70, 71, 72, 73, 74, 120

[7] Teng Shi, **Kushnir, Kateryna**, Zhengtianye Wang, Stephanie Law, and Lyubov V Titova. Photoexcited free carrier dynamics in Bi_2Se_3, $(Bi_0 \cdot 75\, In_0 \cdot 25)_2Se_3$, and $(Bi_0 \cdot 50\, In_0 \cdot 50)_2Se_3$: from topological to band insulator. *ACS Photonics*, 7(10):2778–2786, 2020. 51, 54, 55, 56, 58, 59, 61, 64, 65, 66, 127

[8] DO Oyewole, OK Oyewole, **Kushnir, K**, T Shi, OV Oyelade, SA Adeniji, B Agyei-Tuffour, K Evans-Lutterodt, LV Titova, and WO Soboyejo. Pressure and thermal annealing effects on the photoconversion efficiency of polymer solar cells. *AIP Advances*, 11(4):045304, 2021. 128

List of Abbreviations

THz	:	Terahertz
2D	:	Two Dimensional
3D	:	Three Dimensional
THz-TDS	:	THz Time Domain Spectroscopy
TRTS	:	Time Resolved Terahertz Spectroscopy
TES	:	THz Emission Spectroscopy
SHG	:	Second Harmonic Generation
OR	:	Optical Rectification
PCA	:	Photoconductive Antenna
PDE	:	Photon Drag Effect
MBE	:	Molecular Beam Epitaxy
ARPES	:	Angle-Resolved Photoemission Spectroscopy
SS	:	Surface states
TI	:	Topological Insulator
BI	:	Band Insulator
QWS	:	Quantum Well States
QL	:	Quintuple Layer
AFM	:	Atomic Force Microscope
XRD	:	X-ray diffraction
SEM	:	Scanning Electron Microscopy
CB	:	Conduction Band
VB	:	Valence Band
PEC	:	Photoelectrochemistry
PL	:	Photoluminescence

CVT	:	Chemical vapor transport
CSS	:	Close space sublimation
TEM	:	Transmission electron microscopy
SEM	:	Scanning electron microscopy
EDX	:	Energy dispersive X-ray
SILAR	:	Successive ionic layer adsorption and reaction
TRMPC	:	Time-resolved Microwave Photoconductivity
BPVE	:	Bulk Photovoltaic Effect
FWHM	:	Full Width at Half Maximum
GO	:	Graphene Oxide

Chapter 1

Introduction

Chalcogenides are compounds and alloys of chalcogens: sulfur (S), selenium (Se), and tellurium, (Te). The metal chalcogenide family displays a wide range of electronic and optical properties that are of interest to both fundamental science and practical applications in areas as varied as solar energy conversion, light sources and detectors, thermoelectrics, and chemical sensors. Metal chalcogenides are typically semiconductors with band gaps in the visible and infrared ranges. The wide variety of their properties is further expanded by their ability to create nanoscale structures, such as nanocrystals, nanowires, and two-dimensional (2D) van der Waals systems, in which optical, mechanical, electronic, and other properties depend critically on dimensionality and processes that occur at interfaces. In this work, we will focus on the electronic and optical properties of select semiconducting nanoscale sulfides and selenides, specifically: nanocrystalline lead and bismuth sulfides (PbS, Bi_2S_3) and 2D layered germanium sulfide (GeS), germanium selenide (GeSe), and tin disulfide (SnS_2). We will also investigate a transition from a topological to band insulator in 2D selenide $(Bi_{1-x}In_x)_2Se_3$ as a function of bismuth-indium concentrations. With the exception of PbS, these nanoscale materials are made of non-toxic, earth-abundant elements. The chalcogenides studied here are characterized by high carrier mobility and band gaps in the visible to near-infrared range, and they show promise for a wide spectrum of applications, such as (opto)electronics, energy storage and conversion, catalysis, biomedicine, and sensors.

Many of these applications require a detailed understanding of microscopic photoconductivity, the dynamics of optically excited carriers, and interactions with crystal lattice structures. Spectroscopy with broadband, phase-stable, picoseconds duration terahertz (THz)

pulses enables investigation of these processes over a broad spectral range and with a sub-picosecond time resolution. A major advantage of this technique is its ability to measure the electric field of THz probe pulses, retaining both the amplitude and phase information. As a result, complex, frequency-resolved dielectric function, or equivalently optical conductivity, can be extracted without the need to apply Kramers-Kronig relations. THz time-domain spectroscopy, TDS, provides intrinsic, static properties of the studies' material in the THz range. Time-resolved THz spectroscopy, TRTS, allows following the time evolution of the complex dielectric function or optical conductivity following optical excitation with sub-picosecond time resolution. Finally, in THz emission spectroscopy, TES, the photoexcited sample itself is the source of THz emission, and the emitted THz waveform is analyzed to gather information about the processes responsible for the emission such as optical rectification, ultrafast currents, and charge transfer processes.

Using THz-TDS, TRTS, and TES, we can uncover new aspects of chalcogenides' optoelectronic properties and establish their relationships with structure and morphology. We have found that nanocrystalline chalcogenides have a strong optical absorption and sufficiently long lifetimes of photoexcited carriers, which is necessary for heterojunction solar cells. We for the first time measured the effects of annealing on carrier lifetime in Bi_2S_3 nanocrystal films, and studied the role of grain boundaries and interfaces in polycrystalline PbS.

Like other members of the 2D material family, 2D chalcogenides exhibit distinct properties that arise from the confinement of charge carriers in individual layers and light-matter interactions that are enhanced due to reduced dielectric screening [1, 2]. The distinctive characteristics of 2D GeS and GeSe stem from their highly anisotropic distorted orthorhombic crystal structure, and they include room temperature ferroelectricity in individual layers as well as strong in-plane anisotropy of electronic and optical properties that can be controlled by external fields and strains. Here, we demonstrate that these materials exhibit bias-free surface photocurrent, suggesting applications in next generation photovoltaics as the novel efficient sources of THz radiation. We discovered that the exceptionally high mo-

bility and long lifetime of photoexcited carriers make vertically aligned 2D SnS_2 nanosheets excellent candidates for photoanodes, and we used THz spectroscopy to determine nanosheet dimensions that resulted in optimal device performance. We also found that above band gap photoexcitation of a single-crystalline, multilayer SnS_2 results in emission of THz radiation. The exact origin of this effect is yet to be elucidated, but our preliminary studies point to a complicated interplay between free carriers and optical excitation of phonon modes that break inversion symmetry and enable second order nonlinear processes. Finally, in the case of $(Bi_{1-x}In_x)_2Se_3$, we studied the evolution of photoexcited carrier dynamics as changes in chemical composition resulted in a transition from a topological to band insulator. These experiments illustrate the wide range of optoelectronic properties that can be achieved in nanostructured chalcogenide materials, and they lay the foundations for future studies and applications of chalcogenides in the next generation of photovoltaic, electronic, and photonic devices.

This Thesis is outlined as follows: in Chapter 2, we introduce the experimental techniques that were used to study chalcogenide materials. Specifically, we will provide an overview of the generation and detection of broadband THz pulses, introduce THz-TDS, TRTS, and TES experiments, and discuss the phenomenological models that were applied to analyze experimental intrinsic and photoinduced complex THz conductivity. Chapter 3 details TRTS studies of ultrafast carrier dynamics in GeS nanoribbons, $(Bi_{1-x}In_x)_2Se_3$ thin-films across the transition from topological to band insulators, and single crystalline SnS_2 compared to arrays of vertical SnS_2 nanoflakes. We also discuss the effects of annealing on the optical properties of Bi_2S_3 nanocrystals and investigate the role of the boundaries in photoexcited carrier dynamics in polycrystalline PbS and in PbS/ZnO heterojunction structures. In Chapter 4, we present the evidence for an in-plane zero-bias photocurrent in response to above band gap excitation in GeS, GeSe, and SnS_2. Finally, Chapter 5 presents the outlook for continued investigations of photoexcited carrier dynamics in nanostructured chalcogenide materials.

Chapter 2

Experimental Methods

THz radiation occupies a range from approximately 0.1 to 30 THz, lying between the infrared and the microwave ranges in the electromagnetic spectrum [4], as shown in Fig.2.1. Since the first demonstration of THz-TDS in the late 1980s [5, 6], THz science and technology has rapidly matured. Its domain of applications now includes materials science, information technology and high speed wireless communications [4], biomedical imaging and genetic diagnostics [7, 8], non-destructive evaluation, homeland security through imaging and sensing of explosives, weapons and drugs [9], quality control of food and agricultural products, and global environmental monitoring [4, 10].

Frequency of 1 THz corresponds to a wavenumber of 33 cm^{-1}, a wavelength of 300 μm, a photon energy of 4.1 meV, thermal energy of 50 K, and a period of 1 ps. The energy of a photon with a frequency of 1 THz is smaller than the characteristic thermal energy of $k_bT = 25\ meV$ at room temperature, and far smaller than the typical bandgap energy of a semiconductor. Thus, THz spectroscopy has become a valuable tool for condensed matter physics and materials science as it is well suited to probe low-energy processes and excitations, such as free carrier absorption, carrier scattering [11, 12, 13, 14, 15], plasma formation in semiconductors [16], lattice vibrations in solids [17], exciton orbital transitions [18], and energy gaps of Bardeen–Cooper–Schrieffer superconductors [19].

The aim of this chapter is to describe the methods used to generate and detect THz radiation using femtosecond optical pulses. It also provides a detailed description of the THz-TDS, TRTS, and TES techniques that were used to study 2D and nanocrystalline chalcogenides.

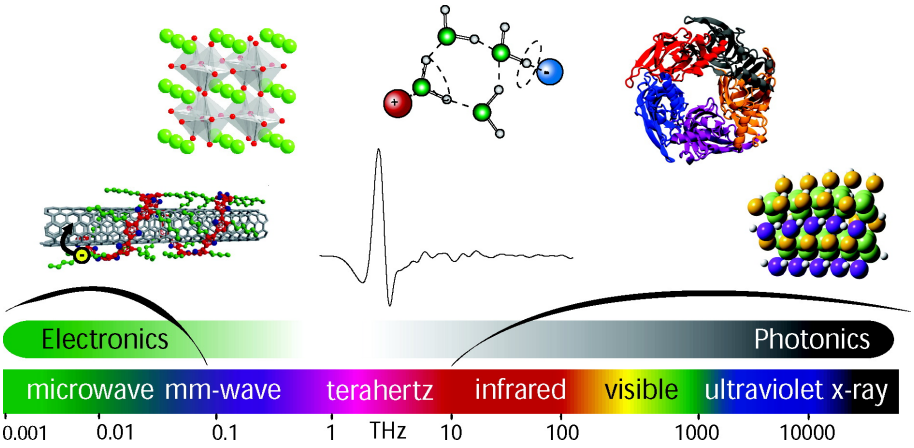

Figure 2.1: Electromagnetic spectrum showing the THz range, in THz units. This figure is reprinted from [3] with permission.

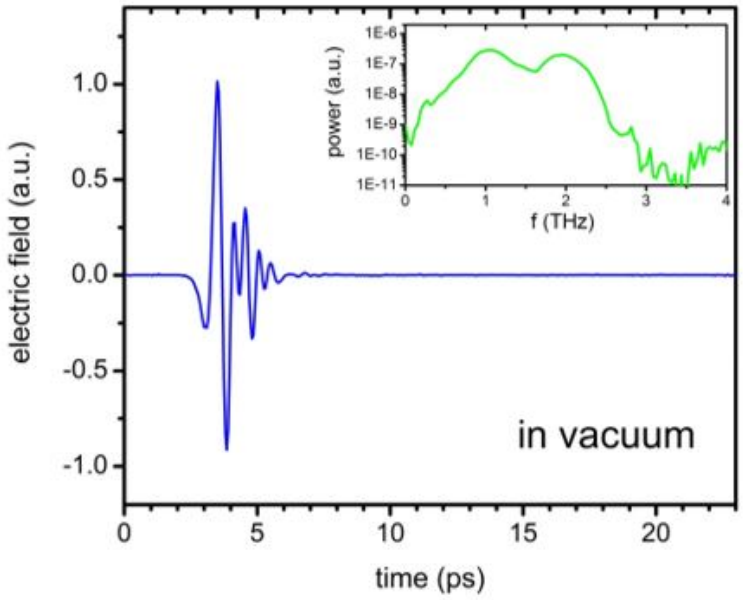

Figure 2.2: Typical THz pulse generated in ZnTe crystal in vacuum. Enclosed power spectrum of the THz pulse (measured in the Ultrafast Spectroscopy Laboratory, University of Alberta, PI F.A. Hegmann).

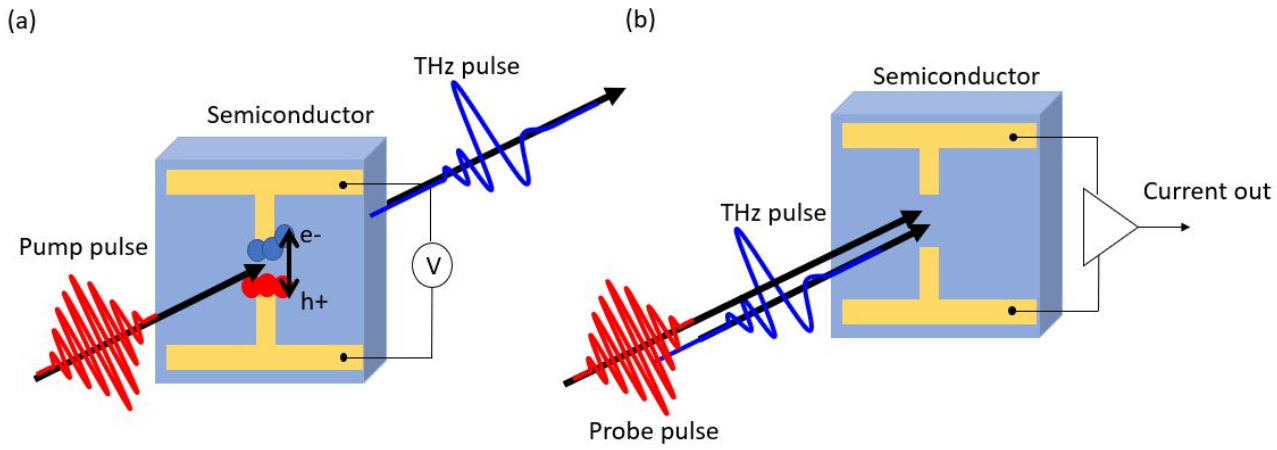

Figure 2.3: Illustration of a biased Hertzian dipole antenna on a semiconductor (blue material) pumped by a NIR fs pulse. (a) demonstrates its use as a source, and (b) as a detector of THz pulses.

2.1 THz generation and detection

An example of a broadband THz pulse used in spectroscopic applications is shown in Fig. 2.2. It is a nearly single-cycle electromagnetic transient with a duration of several picoseconds and a corresponding bandwidth that extends up to $\sim 3\ THz$. A number of techniques to generate broadband THz pulses using ultrashort optical pulses have been developed over the past three decades. In this section, we will describe the four most common approaches: photoconductive antennas, optical rectification in a nonlinear medium, plasma ionization in air, and spintronic emitters.

2.1.1 Photoconductive antennas

Auston et al. were the first to use a photoconductive antenna to generate THz pulses in 1984 [20]. Since then, photoconductive antennas remain widely used as THz sources and detector devices due to their excellent performance, low cost, and relative simplicity.

A photoconductive antenna consists of a pair of parallel electrodes with a small gap on a semiconducting substrate. One of the most common types of photoconductive antennas is

the Hertzian dipole antenna, where two metallic electrodes with an applied bias voltage form a dipole with a gap separated by $5 - 10\ \mu m$, as illustrated in Fig. 2.3 (a).

To generate a THz pulse, a short, above-bandgap optical pulse photoexcites carriers in a semiconductor. The carriers are accelerated by the DC bias and then recombine. This creates a transient current $J(t)$, which emits an electromagnetic pulse with an electric field directly proportional to the time derivative of the current, $E(t) \propto \partial J(t)/\partial t$, in the far field. If the excitation pulse has a sub-picosecond duration, the emitted pulse has frequency components in the THz range. It is collected and collimated by an attached lens (typically, Si).

To detect the generated THz radiation, another photoconductive antenna is used. In the detector, the optical sampling pulse and a THz pulse are both focused into the gap between the electrodes, but this time without an applied DC bias (Fig. 2.3 (b)). The optical pulse photoexcites the carriers in the semiconductor. When the THz pulse is present, it drives the charges from one side of the antenna to the other. The resulting current and current direction are proportional to the amplitude and instantaneous direction of the THz electric field, respectively. The optical pulse is much shorter than the THz pulse and coherently gates the detection by photoexcitation. The THz pulse is then reconstructed in the time domain by measuring the detector current while varying the time delay between the optical and THz pulses. In general, shorter optical pulses and carrier lifetimes are advantageous for higher bandwidth. For example, it has been reported that THz radiation in a low temperature grown $GaAs$ photoconductive emitter reaches 30 THz frequency with a 12 fs laser pulse [21]. Typically, photoconductive antennas have a bandwidth of $\sim 6\ THz$.

2.1.2 Nonlinear crystals

Another popular method of generating THz radiation is to use nonlinear crystals. As shown in Fig. 2.4, shining an optical pump pulse with photon energy below band gap on the crystal with a strong second order nonlinear response drives polarization oscillation, which acts as a source of electromagnetic waves. This second order nonlinear effect is called optical

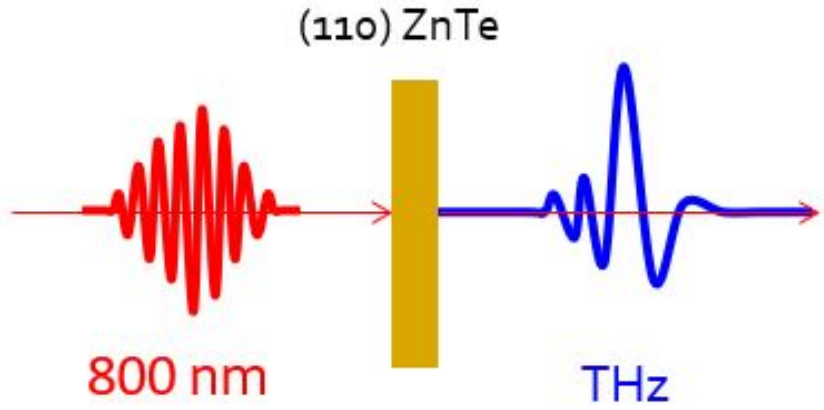

Figure 2.4: Generation of THz pulses by optical rectification in ZnTe crystal.

rectification.

The polarization response $P(t)$ of a material to an applied electric field is described by:

$$P(t) \propto \chi^{(1)}E(t) + \chi^{(2)}E^2(t) + \chi^{(3)}E^3(t) + ... \tag{2.1}$$

where $\chi^{(n)}$ is the n^{th} order of electric susceptibility and $E(t)$ is the applied electric field. Higher order responses result from anharmonic acceleration of charges along the bonds within the material in response to external electric fields. Optical rectification is a second order process, originating from $P^{(2)} = \chi^{(2)}E^2(t)$ - a nonlinear term. If the incident optical beam has two frequency components, $E_1 = E_0\cos(\omega_1 t)$ and $E_2 = E_0\cos(\omega_2 t)$, the second order nonlinear polarization will look like:

$$P^{(2)}(t) = \chi^{(2)}E^2(t) = \frac{\chi^{(2)}E_0^2}{2}[\cos(\omega_1 - \omega_2)t + \cos(\omega_1 + \omega_2)t] \tag{2.2}$$

where the first term corresponds to the difference frequency and the second term corresponds to the sum frequency generation. In a special case of $\omega_1 = \omega_2$, the difference frequency term yields a quasi-DC polarization, or optical rectification. Since an ultrafast laser pulse with sub-picosecond duration contains a range of frequencies, difference frequency mixing between the various frequency components results in the emission of an electromagnetic pulse

that follows the excitation pulse envelope and has frequency components in the THz range. This process also requires phase matching, or matching between the wave vectors of the fundamental and second order waves. In the far field, $E_{THz} \propto \partial^2 \overrightarrow{P}(t)/\partial t^2$ [22]. For example, a Gaussian profile laser pulse with a center frequency of 800 nm wavelength and a pulse width of 100 fs will contain optical wavelengths spanning a range of approximately 795 nm - 805 nm, which gives us the frequency bandwidth defined by the pulse envelope of $\sim 4.4\ THz$ [23].

There is a set of criteria that a crystal should satisfy to be an efficient THz source. The crystal should be non-centrosymmetric, with a large second order susceptibility $\chi^{(2)}$ or, equivalently, electro-optic coefficient ($r_{ijk} = -\frac{2\chi^{(2)}_{ijk}(-\omega,\omega,0)}{n_i^2 n_j^2}$, [24]). To avoid absorption losses in the crystal, it should be transparent in both the optical and the THz frequency ranges. In the THz range, the effective bandwidth of generated THz pulses is often limited by the infrared active phonon resonances. Finally, phase-matching conditions must be satisfied: the optical pulse and the induced THz pulse have to propagate in phase in order for the THz pulse to be coherently amplified. The largest possible THz pulse amplitude will be produced when the optical group index matches the phase index of the center frequency of the THz bandwidth [25].

ZnTe crystals are one of the most common THz sources due to their relatively high electro-optic coefficient ($r_{41} = 3.9\ pm/V$ at $\omega_{THz} = 0$ [26]), large band gap ($\sim 2.25\ eV$), and little phonon absorption in the range from $0.2 - 3$ THz. Of critical importance is that the phase matching of this crystal is satisfied for 800 nm laser pulses and collinear propagation of THz pulses is achieved [25]. Terahertz generation is maximized for a (110) ZnTe crystal when the optical pulse polarization is along the (111) direction. Other non-linear crystals used for THz generation by optical rectification include GaAs, CdTe [27], GaP [28], GaSe [29, 30], and organic crystals such as DAST (4-Dimethylamino-N-methyl-4-Stilbazolium Tosylate) [31, 32]. As discussed in Chapter 4, one of the potential applications of 2D chalcogenides GeS, GeSe and SnS_2 is as new efficient THz sources [33, 34] based on an ultrafast shift current, a

process that occurs in response to the above band gap excitation but is governed by the same nonlinear material properties [35, 36].

Another THz source is $LiNbO_3$ [37], which has a high nonlinear optical coefficient of $r_{33} \sim 20\ pm/V$ [38]. Its major drawback is a large phase mismatch between the optical pump pulse and the generated THz pulse, resulting in THz radiation being emitted into a cone in a Cherenkov geometry [39]. Hebling et al. [40] proposed to achieve phase matching between optical excitation and emitted THz radiation in $LiNbO_3$ by tilting the optical pulse front to coincide with the Cherenkov emission angle. With this approach, intense THz pulses with peak electric fields reaching 1 MV/cm have been generated and applied to study nonlinear processes in the THz range [41].

Non-linear crystals, such as ZnTe, GaP, and others, are also used to detect THz pulses using a free-space electro-optic detection based on the Pockel's effect, as illustrated in Fig. 2.5 [25]. In the absence of the THz pulse, a linearly polarized sampling beam traverses the detector crystal with an unchanged polarization state. It is then converted to a circularly polarized beam by the quarter wave plate and split by the Wollaston prism into two equally intense beams with orthogonal linear polarizations. In this case, balanced photodiodes placed behind the Wollaston prism measure zero differential signal. The THz electric field induces birefringence in the detector crystal that is proportional to the THz electric field. If an optical beam passes through the crystal at the same time as the THz pulse, its polarization state is changed to elliptical, with the ellipticity proportional to the THz electric field. Changes in THz-induced ellipticity are detected as a non-zero (positive or negative, depending on THz electric field direction) differential signal measured by the balanced photodiodes. For small changes, the differential signal is proportional to the THz electric field. By changing the delay time between the THz pulse and the optical pulse, the entire THz waveform (Fig. 2.2) can be reconstructed. Like in the case of photoconductive antennae, this results in coherent detection of THz pulses. Using an optical chopper in the THz generation beam and lock-in detection, a signal-to-noise ratio of up to 1000:1 can be achieved.

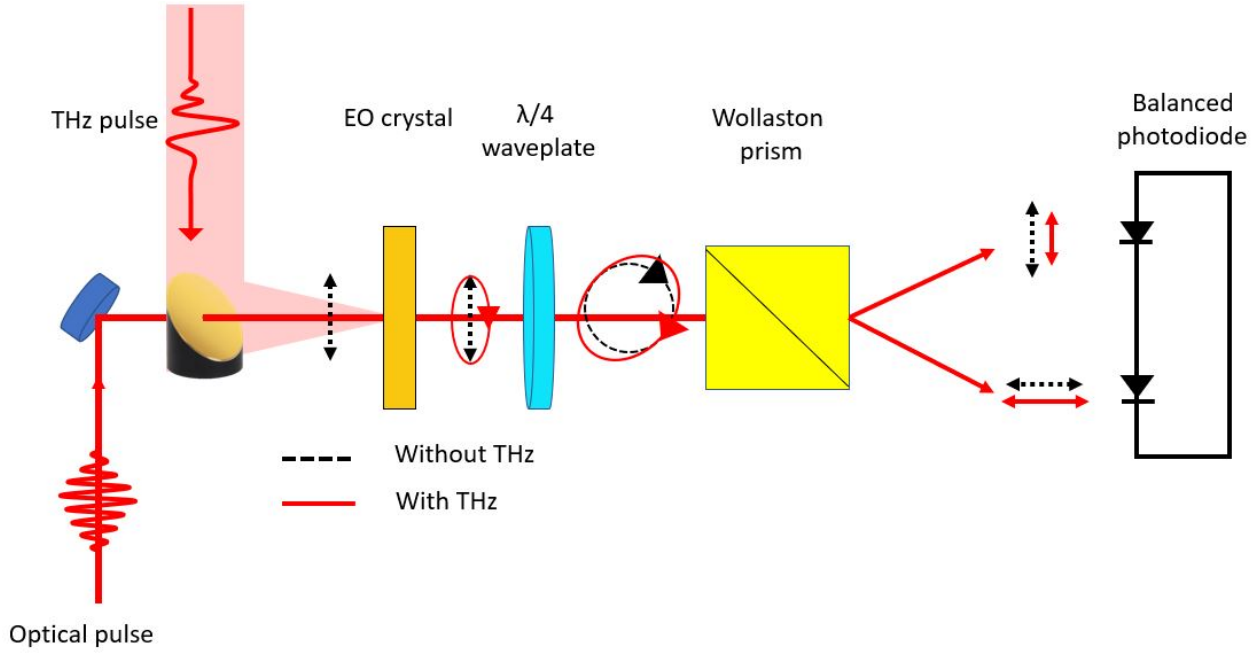

Figure 2.5: Schematic of free space electro-optic detection for the detection of THz pulses.

In this work, a 1 mm-thick (110) ZnTe crystal was used as a THz source for the spectroscopy measurements in $0.2 - 2.5$ THz range. The THz pulse polarization was oriented parallel to the (110) direction for electro-optic detection.

2.1.3 Air Plasma

In recent years, a new method of generating THz pulses without the need for solid state materials, biased electrodes, or forward propagating signal collection has emerged. It is known as air plasma THz generation. Air plasma generates ultrabroadband THz pulses with a bandwidth encompassing the entire THz range up to $\sim 100\ THz$, with peak electric fields surpassing 1 MV/cm [42, 43, 44]. THz generation is achieved by focusing a laser pulse with a center frequency ω along its second harmonic 2ω in air or a gas cell. Ultra-high optical fields at the focus ionize gas, and the free electrons respond to an asymmetric two color laser field inducing transverse currents that vary on the time scales of the laser pulse envelope [45].

The detection of the ultra-broadband THz pulses is achieved in air and other gases due to a third order nonlinear susceptibility, and can be explained as a four wave mixing process

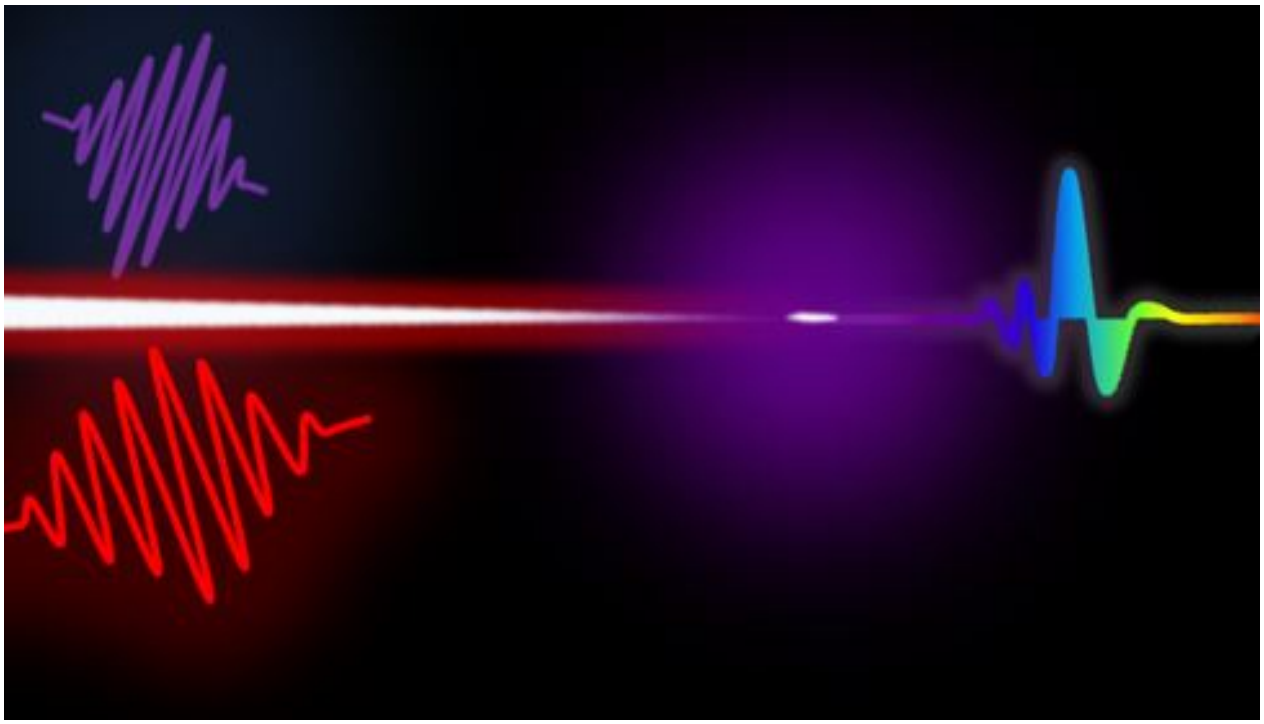

Figure 2.6: Generation of THz pulses via a two color laser induced plasma.

[46, 47**?**]. Implementation of plasma THz generation requires intense laser pulses from an amplified laser system. ABCD detection relies on a high voltage signal with a square waveform to provide a modulated biased field over the air sensor. While it is difficult to implement, a plasma THz system has superior intensity and bandwidth, making it an attractive option for THz spectroscopy.

2.1.4 Spintronic Emitters

Over the last few years, a conceptually new approach for THz generation has been explored. Contrary to most solid-state emitters, which solely exploit physics related to electron charge, it instead relies on three fundamental spintronic and photonic phenomena in magnetic metal multilayers: ultrafast photoinduced spin currents, the inverse spin-Hall effect, and a broadband Fabry–Pérot resonance. This new approach has the potential to combine various benefits in one device: large bandwidth, large THz field amplitude at low pump power, easy operation, scalability, and low cost.

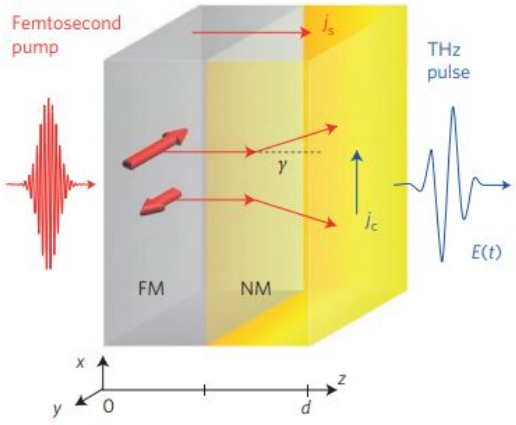

Figure 2.7: Principle of operation of a spintronic THz emitter. This figure is reprinted from [48] with permission.

A basic principle of THz spintronic emitters is shown on the Fig. 2.7, where a bilayer structure consisting of ferromagnetic and non-ferromagnetic metal thin films is excited by a femtosecond laser pulse. Electrons are excited in the metals to states above the Fermi energy, thereby changing their band velocity and scattering rate. The ferromagnetic layer is magnetized in-plane, antiparallel to the y axis. Because the ferromagnetic and non-ferromagnetic layers have different transport properties, a net current along the axis is launched. In addition, because the product of the density, band velocity, and lifetime of spin-up (majority) electrons in ferromagnetic metals (such as Fe, Co and Ni) is significantly higher than that of the spin-down (minority) electrons, the z current is strongly spin-polarized. On entering the non-ferromagnetic layer, spin–orbit coupling deflects spin-up and spin-down electrons in opposite directions by a mean angle γ. This inverse spin-Hall effect converts the longitudinal (z-directed) spin current density j_s into an ultrafast transverse (x-directed) charge current density $j_c = \gamma j_s$, thereby acting as a source of THz radiation[48].

2.2 THz Time-Domain Spectroscopy (THz-TDS)

THz-TDS relies on coherent detection of THz pulses in the time domain. Applying Fourier transformation to the waveforms thus yields the amplitude and phase of all the spectral components that comprise a THz pulse. Comparing the amplitude and phase of all the spectral components of a THz probe pulse that has been transmitted through or reflected off a sample to those of the reference THz pulse allows extraction of complex optical functions over the entire accessible bandwidth. This is a critical advantage of THz-TDS over other spectroscopic modalities, such as IR-UV-Vis spectroscopies, where measurements of intensity are carried out in the frequency domain and phase information is not accessible. A simplified diagram of a THz-TDS spectrometer operating in transmission geometry is shown in Fig. 2.8. A beam from a femtosecond laser (such as a Ti:Sapphire laser, which is used in the studies discussed here) is split into two beams: the THz generation and sampling beams. ZnTe nonlinear crystals are used for both generation and detection of the THz pulses. A series of parabolic mirrors are used to guide the THz pulses from the emitter to the sample, and then to the detector. A delay stage is used in the generation arm in order to vary the arrival time of the signal with respect to the optical pulse used for detection. By scanning the delay line, the electric field amplitude and phase of the THz waveform can be mapped out as a function of time. To achieve a high signal to noise ratio of $\sim$ 1000:1, the THz beam is modulated by an optical chopper, and the THz-induced modulation of the sampling beam is extracted by a lock-in amplifier. A LabVIEW code was written to collect the electric field amplitude as a function of time from a digital lock-in amplifier that measures the signal from the detector. The pulse information acquired in the time domain is transformed to the frequency domain using a Fourier transform, from which spectral information can then be obtained [49].

A wide variety of applications have resulted in a number of different configurations of THz spectrometers. Additionally, a full set of algorithms have been developed for extract-

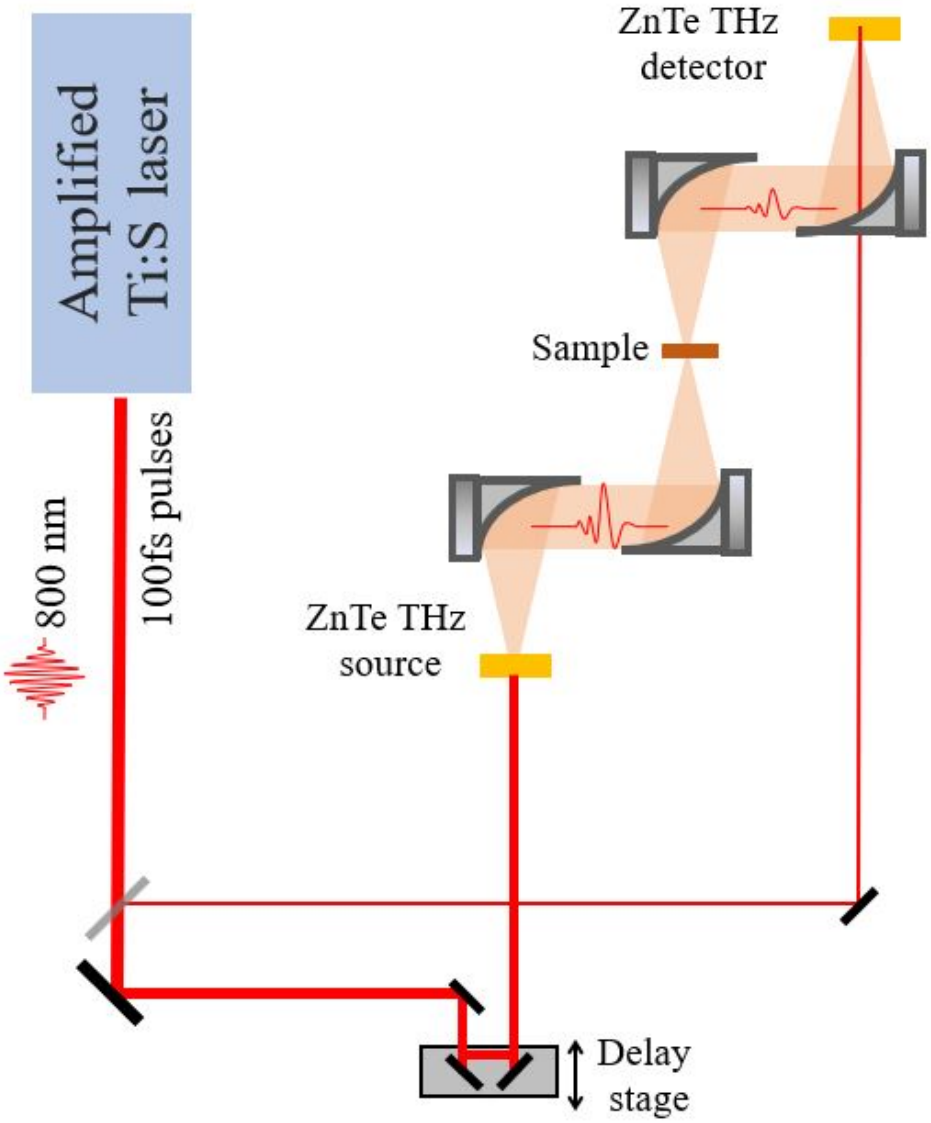

Figure 2.8: Pulsed THz wave generation and detection setup.

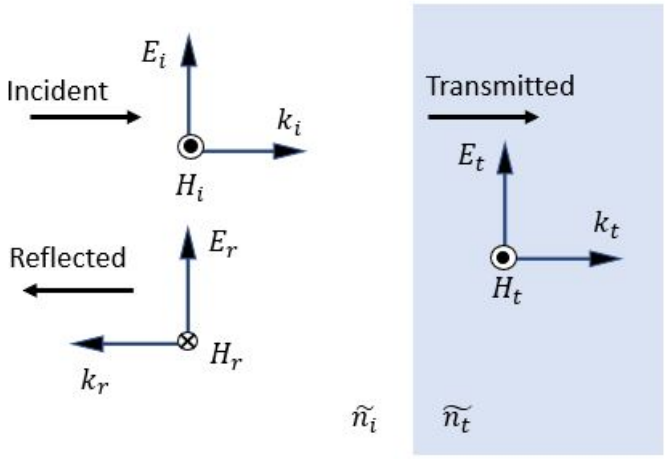

Figure 2.9: Transmission and reflection of light at an interface between two different refractive index mediums.

ing the complex, frequency-resolved optical functions such as refractive index, absorption coefficient, and complex conductivity without resorting to complex mathematical methods such as the Kramers-Kronig relations from experimental THz-TDS data [50, 51, 52]. Here, we review some of those which are particularly useful for experiments with thin films and nanostructures.

Propagation of THz waves through samples, their transmission and reflection, can all be analyzed using Fresnel equations. Let us consider an x-polarized beam propagating along the z direction in a normal incidence geometry as shown in Fig. 2.9. For simplicity, we assume that two media forming a planar interface are isotropic and described by the complex refractive indices $\tilde{n_i} = n_i + i\kappa_i$ and $\tilde{n_t} = n_t + i\kappa_t$, where n is the refractive index, and κ is the extinction coefficient. From the boundary conditions at the interface between two dielectrics, the tangential components of the electric and magnetic fields must be continuous:

$$E_i + E_r = E_t \tag{2.3}$$

$$H_i + H_r = H_t \tag{2.4}$$

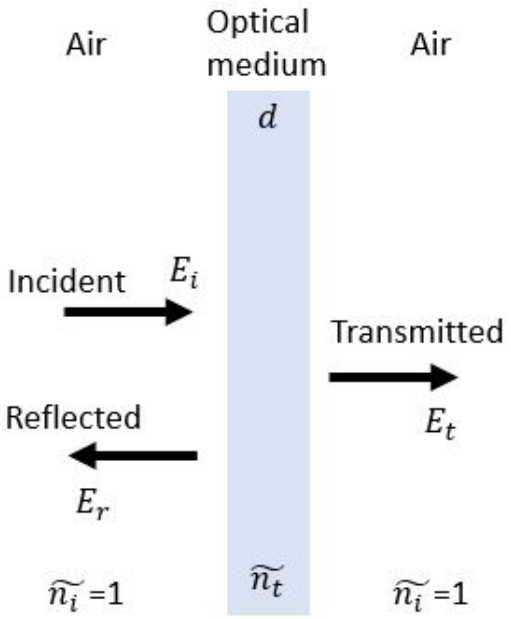

Figure 2.10: Incident, transmitted and reflected electric fields in a sample of thickness d.

where i, r, and t correspond to the incident, reflected, and transmitted light respectively. Using the relations between the electric and magnetic field $H = B/\mu$ and $E = \frac{c}{n}B$, where μ is permeability, c is speed of light and n is refractive index, we obtain the reflection and transmission coefficients:

$$\tilde{r} = \frac{E_r}{E_i} = \frac{\tilde{n_i} - \tilde{n_t}}{\tilde{n_i} + \tilde{n_t}} \tag{2.5}$$

$$\tilde{t} = \frac{E_t}{E_i} = \frac{2\tilde{n_i}}{\tilde{n_i} + \tilde{n_t}} \tag{2.6}$$

These equations describe the change in amplitude and phase of the electromagnetic radiation as it crosses an interface of a bulk material.

Now let us examine transmission of an electromagnetic wave through a parallel-plate sample with thickness d and refractive index n, such as a crystalline silicon wafer. The wafer is surrounded by air ($n_{air} = 1$), as shown in Fig. 2.10. The complex transmission function,

defined as the ratio between the transmitted field E_t and the incident field E_i, is represented by Eq. 2.7 for the first transmitted pulse:

$$\frac{E_t(\omega)}{E_i(\omega)} = T(\omega)e^{i\phi(\omega)} = t_{12}t_{21}\frac{P_2}{P_1} = \frac{4\tilde{n}}{(1+\tilde{n})^2}e^{i(\tilde{n}-1)\frac{\omega}{c}d} \tag{2.7}$$

In this equation, we take into account the complex Fresnel transmission coefficients at both interfaces, and an additional transmission factor $P = e^{i\frac{\omega}{c}nd}$ that accounts for propagation though the material. This results in both a phase shift term proportional to the real index of refraction (n), and an attenuation term proportional to the extinction coefficient (κ), the imaginary component of the complex index of refraction ($\tilde{n} = n + i\kappa$). Furthermore, the complex index of refraction is generally frequency dependent. Separating the real and imaginary parts of the refractive index in Eq. 2.7:

$$T(\omega)e^{i\phi(\omega)} = \frac{4\tilde{n}}{(1+\tilde{n})^2}e^{i(n-1)\frac{\omega}{c}d}e^{-\kappa\frac{\omega}{c}d} \tag{2.8}$$

The spectral phase $\phi(\omega) = (n-1)\frac{\omega}{c}d$ encodes important information about the optical properties of the material, in this case the refractive index, and the limit where the phase accumulated through the bulk of the crystal is much larger than the phase change occurring at the interface. It is possible to extract the index directly from the spectral phase analytically:

$$n(\omega) = \frac{\phi(\omega)c}{\omega d} + 1 \tag{2.9}$$

Eq. 2.8 also shows an attenuation term, the extinction coefficient $\kappa(\omega) = \frac{\alpha(\omega)c}{2\omega}$, which is proportional to the absorption coefficient. It in turn can be calculated as:

$$\alpha(\omega) = -\frac{2}{d}\log(\frac{(n+1)^2}{4n}T(\omega)) \tag{2.10}$$

Figures 2.11 and 2.12 illustrate such measurements. The experimental THz waveforms of the pulses that traveled through air and a 463 μm thick high resistivity silicon wafer are

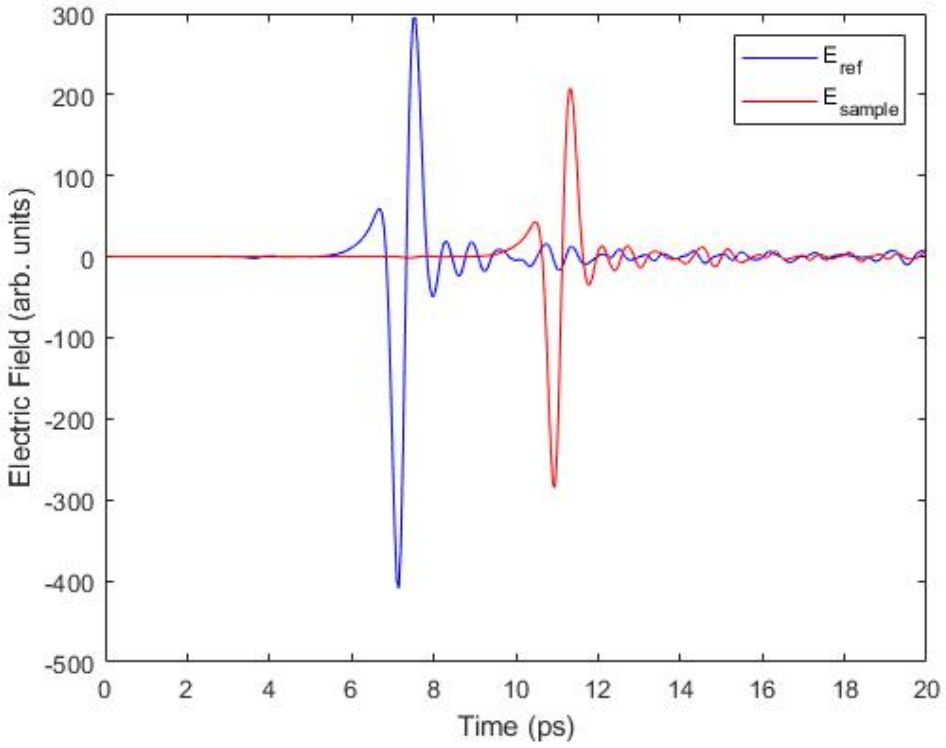

Figure 2.11: THz pulse that had propagated through air (blue, E_{ref}) and through a $463\mu m$ thick single crystalline Si wafer (red, E_{sample}). Recorded using Toptica TeraFlash THz TDS spectrometer in the Photonics Lab for Education and Application Prototypes at WPI.

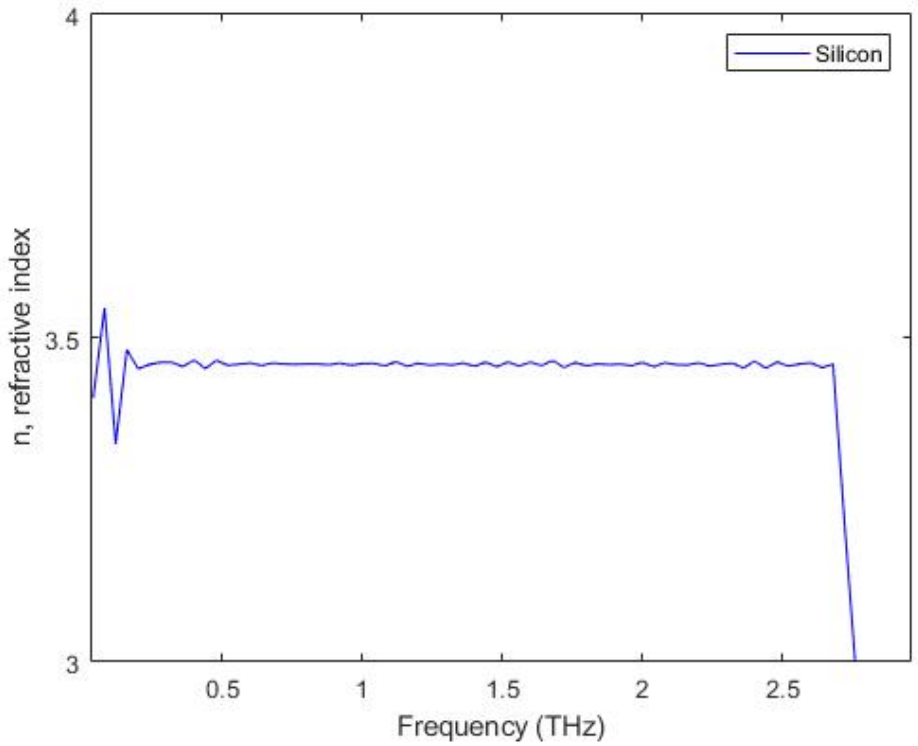

Figure 2.12: Refractive index of Si, extracted by analyzing waveforms in Fig. 2.11.

shown in Fig. 2.11. Analyzing the waveforms as described in this section, we obtain the frequency-resolved refractive index shown in Fig. 2.12. It shows good agreement with the literature value of $n = 3.46$, independent of frequency in the THz range [50]. However, due to the bandwidth limitations of our detector and low signal to noise ratio, we can see that at the low frequencies ($\leqslant 0.2\ THz$) and at the high frequencies ($\geqslant 2.7\ THz$) our signal becomes too noisy. Similarly, using Eq. 2.9 we are able to extract absorption of the material in the THz range; however, in the case of high resistivity silicon, the absorption is around zero. The Matlab scripts used for THz-TDS analysis are given in the Appendix A.

In some cases, it is more instructive to represent optical properties of materials determined by the THz-TDS in terms of complex optical conductivity. The relations between the complex refractive index, dielectric function, and complex conductivity are:

$$\tilde{n} = n + i\kappa$$

$$\alpha = \frac{2\kappa\omega}{c}$$

$$\tilde{\epsilon} = \epsilon_1 + i\epsilon_2 = \tilde{n}^2 = 1 + \frac{i\tilde{\sigma}}{\epsilon_0\omega}$$

$$\tilde{\sigma} = \sigma_1 + i\sigma_2$$

$$\epsilon_1 = n^2 - \kappa^2$$

$$\epsilon_2 = 2n\kappa$$

$$\sigma_1 = \epsilon_0\epsilon_2\omega$$

$$\sigma_2 = -\epsilon_0(\epsilon_1 - 1)\omega$$

2.3 Time-resolved THz spectroscopy (TRTS)

While THz pulses are recorded in the time domain, THz-TDS is not a time-resolved technique. The dielectric function obtained from the sample is static. However, a short duration and phase stability of THz pulses allows their use in a pump-probe technique, time-resolved THz spectroscopy (TRTS). This technique uses femtosecond optical pulses from the same laser to photoexcite the sample, guaranteeing a perfect synchronization with the probe THz pulses [53, 54, 55]. This technique is widely used to study the onset and evolution of ultrafast phenomena occurring at low energies on femtosecond to nanosecond time scales in a variety of material systems [17, 22, 53, 54, 55, 56, 57, 58, 59, 60, 61, 62, 63, 64, 65].

2.3.1 Experiment

As illustrated in Fig. 2.13, the TRTS setup is similar to a THz-TDS setup, with the addition of the femtosecond optical pump pulse, and a second delay line used to control the relative delay time between the THz probe pulse and optical pump pulse arrival at the sample. This way, the rise and fall of the induced photoconductivity can be mapped in time, with a resolution limited primarily by the width of the THz pulse. The power of this technique lies in the ability to map the dynamics of the broadband optical response functions, such as the complex optical conductivity, over THz frequencies as they evolve after photoexcitation.

The THz frequencies obtained in our setup are varied from $0.2 - 2.5\ THz$, which means that the size of the THz diffraction-limited spot is about $1.5\ mm$. This places restrictions on the pump pulse spot size, requiring it to be larger than the THz spot to achieve a uniform photoexcitation of the sample, so as to avoid experimental artifacts. In the setup used here, optical excitation of a 800 nm or 400 nm beam was delivered to the sample through a 5 mm aperture in a 2 inch diameter parabolic mirror that focused the THz probe pulses onto the sample. The optical pump and THz probe pulses are collinearly propagated to minimize temporal smearing.

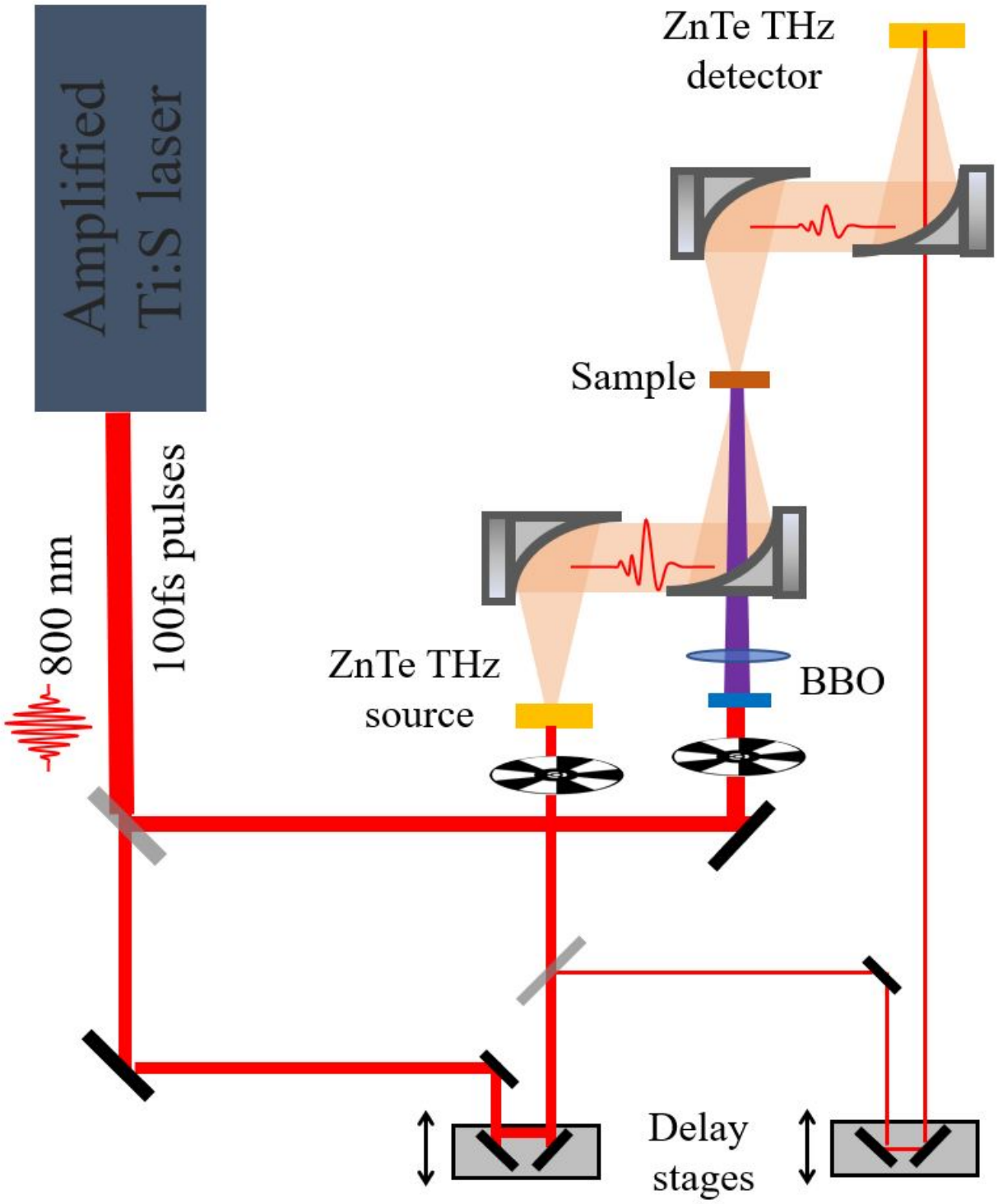

Figure 2.13: Schematic of the experimental setup for TRTS spectroscopy based on THz generation by optical rectification in ZnTe crystal and free-space electro-optic detection.

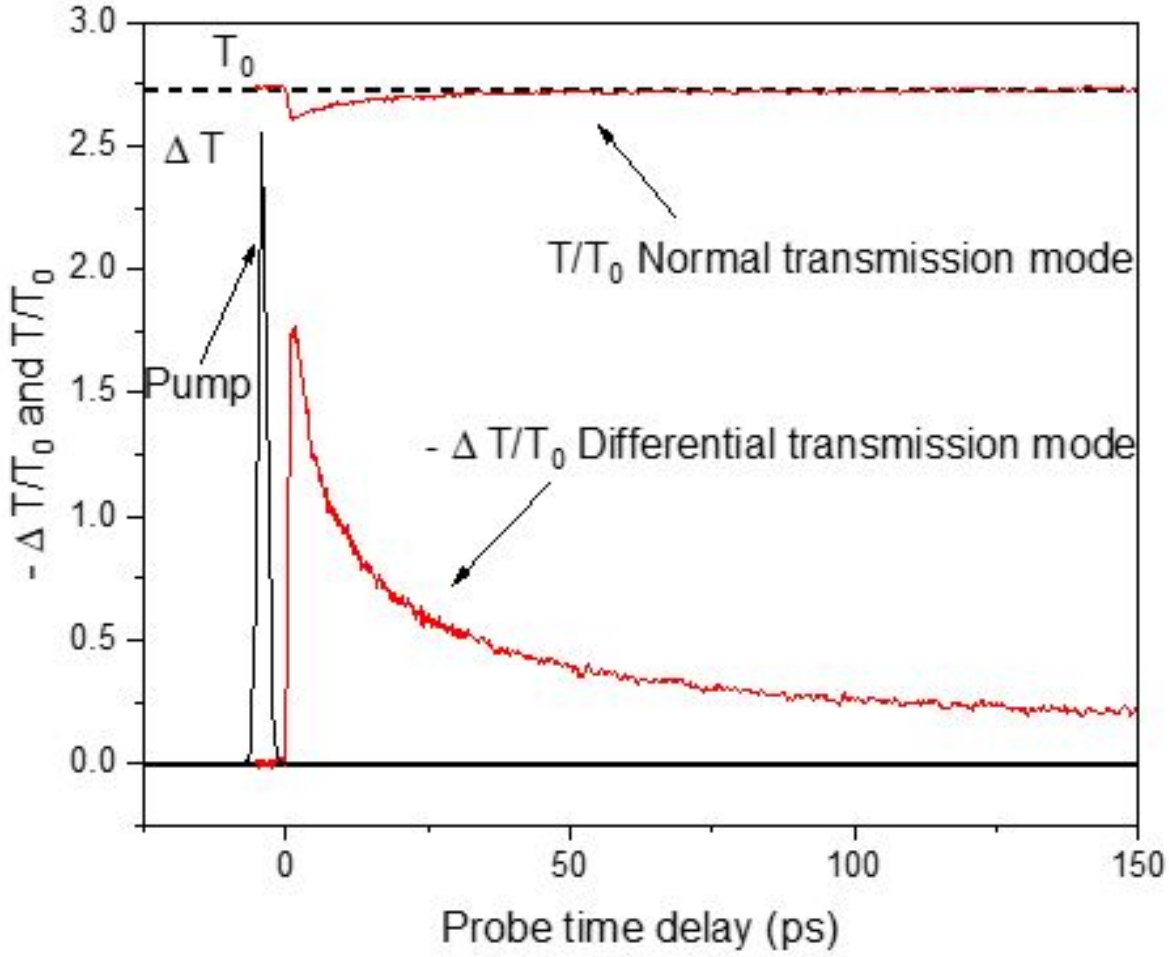

Figure 2.14: Example 1-D TRTS scan, showed in arbitrary units. GeSe crystal photoexcited by 100 fs, 400 nm pulses with 200 $\mu J/cm^2$ excitation fluence.

2.3.2 Data acquisition

When acquiring data in TRTS, it is possible to scan the probe delay line, the pump delay line, or both, resulting in either one-dimensional (1-D) or two-dimensional (2-D) data sets.

In a **(1-D) scan**, such as the one shown in Fig. 2.14, we monitor the photoexcitation-induced change in the peak to peak transmission of THz pulse through the sample as a function of the time delay between the pump and probe beams. Our focus is on monitoring the field amplitude attenuation as it traverses a photoconductive layer, neglecting the information carried by pump-induced phase change. When the pump pulse and THz probe overlap in

time at the sample, a change in transmission is observed due to pump-induced absorption, or bleaching. These scans provide information about the timescale associated with the onset of photoconductivity and the lifetime of that conductivity.

To perform such a scan, we first identify the maximum of the transmitted THz pulse, where all its frequency components are in phase. The arrival time of the pump pulse relative to the THz probe pulse is referred to as t_0. Transient changes in THz peak transmission is recorded by varying the time between the optical pump and THz probe. During the measurement, the pump beam is modulated by an optical chopper at 500 Hz (1/2 the repetition rate of the Ti:Sapphire amplifier, or blocking every second pump pulse), while the THz generation beam is chopped at 250 Hz. This way, the lock-in amplifier synchronized to the pump chopper then monitors the modulation of the THz peak electric field at the frequency of the pump chopper, effectively reading $-\Delta T(t) = T_{pump}(t) - T_0$. Here, T_0 is the THz transmission at negative pump-probe delay times, or prior to pump arrival. At the same time, reading the second lock-in amplifier synchronized to the THz generation beam chopper allows monitoring T_0. This technique using two lock-in technique allows simultaneous monitoring of the THz pulse peak and the pump induced change in its transmission, and thus calibration of $-\Delta T(t)/T_0$. This also allows us to eliminate systematic timing variations and provides a higher signal to noise ratio.

In a **(2-D) scan**, we collect information by recording the full THz waveform at a fixed pump delay time. This is done in a coherent way, allowing us to resolve the amplitude and phase. From the THz waveform, we obtain the photo-excited absorption coefficient and refractive index, and thus calculate conductivity. Not only can we measure the full waveform at a specific time fixed after photoexcitation, we can also create a 2-D map by continuously moving a delay stage with a small time step, limited only by the time duration of the optical pulse. In this way, induced photoconductivity can be mapped. The benefit of doing a full mapping is the possibility of extracting a 1-D scan simply by looking at the peak of a 2-D map. However, the main drawback of conducting this measurement is that taking the full

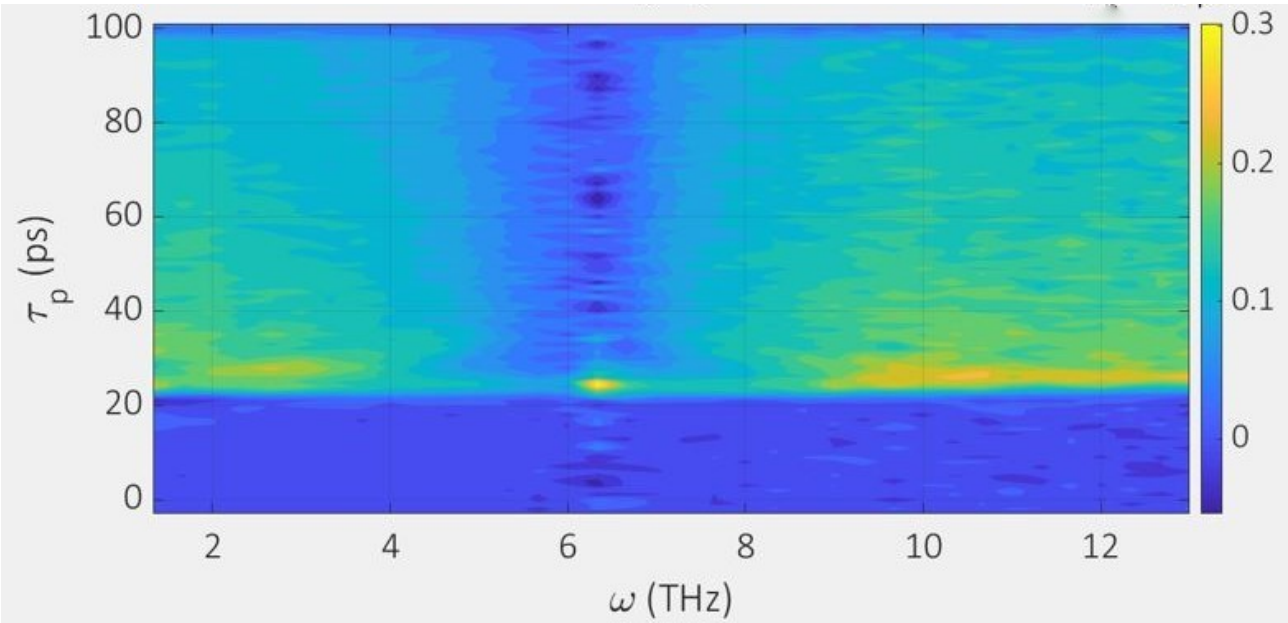

Figure 2.15: 2-D time resolved map of the differential change of the electric field amplitude in frequency domain represented by color in a SnS_2 sample, pumped with 50 $\mu J/cm^2$ fluence, 400 nm pulse. The first 20 ps delay time represents the time before photoexcitation; the higher delay times represents changes after the photoexcitation for the probe frequency up to 12 THz.

THz waveform for each pump-probe delay greatly increases the time needed to record the data, which could present a problem for unstable samples. As an example, the pump induced change in the THz field for a SnS_2 sample has been measured, pumped with $50\mu J/cm^2$ fluence at 400 nm pulses and is shown in Fig. 2.15. Here, the color scale shows the maximum (yellow) and minimum (dark blue) differential changes of the electric field.

It is worth examining the limitations of extracting photoinduced complex dielectric function or conductivity from full THz waveforms recorded at a fixed time after photoexcitation. Similar to the THz-TDS technique, where we are comparing a waveform transmitted through the sample and substrate to a waveform transmitted solely through the substrate, TRTS compares the waveform of the photoexcited sample to the waveform of THz pulse transmitted through the non-photoexcited sample. The step with which we record the points to construct the THz waveform also sets the frequency resolution, thus $\Delta f = 1/N\Delta t$. The resolution of the scan for the THz waveforms typically is not a limiting factor as long as it is below the

Nyquist frequency $f_c = 1/2\Delta t$. We are also limited by the delay stage step. For our measurements, we used $\Delta t = 20fs$ and $f_c = 2.5$ THz, which also corresponds to the max bandwidth of our ZnTe crystal. It is important to note the reflections, which may lead to Fabry-Perot etalon fringes in the frequency domain that interfere with data analysis. Cutting out the reflections will limit the scan duration up to approximately 10 ps, and the resolution obtained will be about 0.1 THz.

Finally, it is vital to consider artefacts introduced by recording the THz pulses transmitted through the photoexcited sample by scanning the delay between the THz sampling beam and both the THz generation beam and the optical pump (Fig. 2.13). In this case, each point in the THz probe pulse experiences a slightly different pump-probe time delay. If the conductivity is decaying on a time scale comparable to the THz pulse, earlier times in the THz waveform could experience higher conductivity than later times. This was first pointed out by the Schmuttenmaer group in 2001 [66]. This issue can be addressed by fixing the THz sampling beam and scanning the other two beams instead. By scanning the THz source beam, the delay between the sampling beam and the pump beam remains fixed, and each point in the detected THz waveform experiences the same pump-probe time delay. I have implemented this modification in the TRTS setup in the Ultrafast Optical and THz Spectroscopy Lab at WPI LEAP.

2.3.3 Data analysis in TRTS: extracting complex photoconductivity

In many cases, including all experiments described here, TRTS is used to investigate transient photoconductivity. In this situation, the choice of the complex optical conductivity to describe complex dielectric properties is natural. Two THz waveforms are needed to extract the transient conductivity of a material. Fig. 2.16 shows the THz pulse waveform $E_{pump}(t)$ transmitted through the photoexcited Si wafer 20 ps after photoexcitation with an 800 nm pulse, and $E_{ref}(t)$ through a sample that has not been photoexcited. The ratio of the Fourier

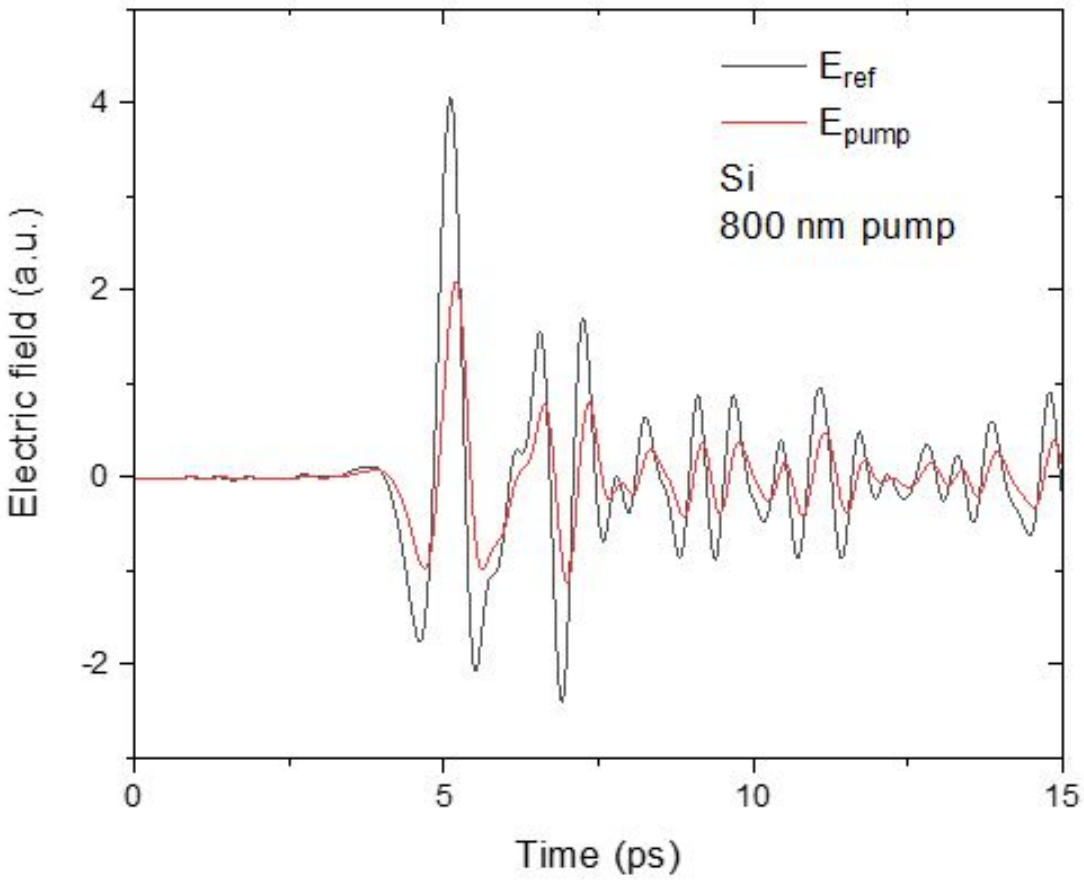

Figure 2.16: Time domain data for transient spectroscopy of Si photoexcited with an 800 nm pulses, 20 ps after excitation.

transforms of these two pulses provides the complex transmission function, which can be analytically related to the complex conductivity.

To simplify data analysis, we can assume that the thickness of the optically excited region in the sample is much smaller than the wavelength of THz radiation ($d \ll \lambda$ or $n_{sample}\omega d/c \ll 1$), and thickness d is much less than the overall sample thickness. If so, we can then use the thin-film approximation for the amplitude transmission of the electromagnetic radiation through a thin conducting film with conductivity $\tilde{\sigma}$ on a semi-infinite insulating substrate with refractive index N [53].

First, let's derive an expression for the complex transmission function through a thin

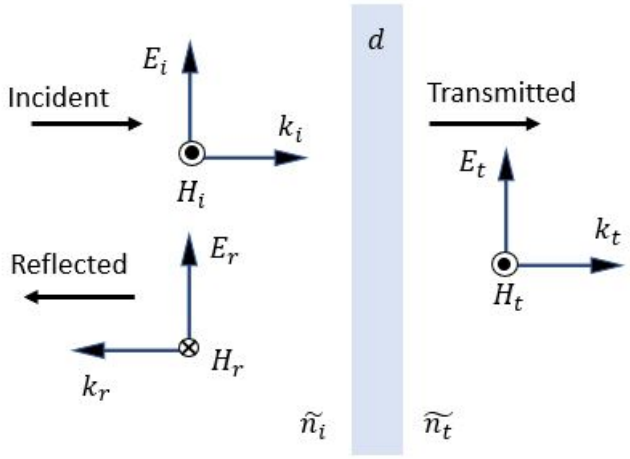

Figure 2.17: Electric and magnetic field vectors after reflection and transmission of an incident electromagnetic wave incident on a thin conducting film.

conducting film between two media with a real index of refraction, as shown in Fig. 2.17. In our experiment, the first media would be air and the second the semi-insulating dielectric substrate. The continuity equations describing the electric and magnetic fields at the boundary are given by:

$$\hat{n} \times (\vec{H_1} - \vec{H_2}) = \int_0^\infty \vec{J} dz = \vec{J} d \tag{2.11}$$

$$\hat{n} \times (\vec{E_1} - \vec{E_2}) = 0 \tag{2.12}$$

Eq. 2.11 and 2.12 could be simplified:

$$H_i - H_r - H_t = Jd \tag{2.13}$$

$$E_i + E_r - E_t = 0 \tag{2.14}$$

These are the same as the boundary equations used to derive the Fresnel transmission

and reflection coefficients at the boundary of a dielectric. The ratio H/E is also known as admittance, and can be rewritten as Y. Combining Eq.2.14, we can rewrite the expression for the transmitted electric field as:

$$E_t = \frac{1}{Y_1 + Y_2}(2Y_1 E_i - Jd) \tag{2.15}$$

Where $Y_1 = \frac{H_i + H_r}{E_i + E_r}$ and $Y_2 = \frac{H_t}{E_t}$. Solving for the transmission coefficient $t = E_t/E_i$ and using the relationship between conductivity and current density $J = \tilde{\sigma} E_t$, we obtain:

$$\tilde{t} = \frac{2Y_1}{Y_1 + Y_2 + \sigma d} \tag{2.16}$$

Making the substitution $Y_a = \frac{N_a}{Z_0}$, where N_a is the index of refraction of the medium and $Z_0 = 377\Omega$ is the impedance of free space, we reach our final expression for the transmission through a thin conducting film, known as the Tinkham equation [67].

$$\tilde{t}_{film} = \frac{2}{N + 1 + Z_0 d\tilde{\sigma}} \tag{2.17}$$

Using the transmission coefficient for the unexcited dielectric substrate $t_{subs} = \frac{2}{N+1}$, we obtain the transmission function for a photoexcited layer with respect to the background unexcited substrate.

$$\tilde{T}(\omega) = \frac{t_{film}}{t_{subs}} = \frac{\tilde{E}_{pump}(\omega)}{\tilde{E}_{ref}(\omega)} = \frac{N + 1}{N + 1 + Z_0 d\tilde{\sigma}(\omega)} \tag{2.18}$$

For deeply penetrating excitation, the distance traversed through the unexcited substrate is sufficiently different from the excited substrate that an additional phase factor must be added. In this case, the thin film equation is written as:

$$\tilde{T}(\omega) = \frac{t_{film}}{t_{subs}} = \frac{\tilde{E}_{pump}(\omega)}{\tilde{E}_{ref}(\omega)} = \frac{N + 1}{N + 1 + Z_0 d\tilde{\sigma}(\omega)} e^{-iNd\frac{\omega}{c}} \tag{2.19}$$

The Tinkham equation can also be used in the reflection geometry:

$$\tilde{R}(\omega) = R(\omega)e^{-i\phi\omega} = \frac{r_{film}}{r_{subs}} = \frac{\tilde{E}_{pump}(\omega)}{\tilde{E}_{ref}(\omega)} = \frac{1 - N - Z_0 d\tilde{\sigma}(\omega)}{N + 1 + Z_0 d\tilde{\sigma}(\omega)} \frac{1+N}{1-N} \tag{2.20}$$

The phase shift in the THz pulse will be small if the complex conductivity is predominantly real. For Drude conductivity, this is satisfied if $\omega\tau < 1$, such that $\tilde{\sigma} \approx \sigma_{DC} = ne\mu$. The negative differential transmission can then be related to the pump-induced change in conductivity $\Delta\sigma$:

$$-\Delta T(t)/T_0 = \frac{T_0 - T_{pump}}{T_0} = 1 - \frac{N+1}{N+1+Z_0 d\sigma} \tag{2.21}$$

This equation can be solved to obtain conductivity:

$$\sigma(t) = \frac{N+1}{Z_0 d}\left(-\frac{\Delta T}{T_0}\right)\left(\frac{1}{1+\frac{\Delta T}{T_0}}\right) \tag{2.22}$$

For small modulations $|\Delta T/T_0| < 20\%$

$$\sigma \approx \frac{N+1}{Z_0 d}\left(-\frac{\Delta T}{T_0}\right) \tag{2.23}$$

This means that differential THz transmission is directly proportional to the conductivity of the film:

$$\sigma \propto -\frac{\Delta T}{T_0} \tag{2.24}$$

The validity of this approach depends on the response of the material being purely resistive, such that the amplitude of the field is uniformly attenuated for all frequency components in the pulse. If there is a significant change in phase across the bandwidth of the pulse, there will be an associated temporal shift in the time domain of the THz pulse. Since in a one-dimensional scan we monitor only the peak of the THz waveform, the time shift causes what appears to be a differential transmission signal, even though there may be no attenuation of the peak. The peak effectively moves in time, so we measure a dip in the transmission

due to sliding off the peak. The direction of the time shift is important and reveals whether the phase change is related to a Drude or Lorentz (below resonance) response, which will be discussed later in this chapter.

Provided that the phase shift is small and the response is well described as Drude, we can further analyze the differential transmission to obtain valuable information on the carrier dynamics in the system, $n(t)$, as well as extract important transport coefficients such as the carrier mobility μ. However, in general the mobility can be time-dependent, in which case $\sigma(t) = n(t)e\mu(t)$ and a more complex analysis is required to separate the carrier density from the mobility response. If the mobility is time-independent, then the decay of the conductivity is entirely due to the decay of free charge carriers.

2.4 Conductivity models

There are many theoretical models for the complex conductivity of materials that can be used to described the data for σ_1 and σ_2 obtained from the THz experiments. The complex conductivity completely describes both mobile and bound charges in the material. Analysis of the frequency dependence of σ_1 and σ_2 can be used to distinguish between the various models and help identify the nature of the observed conductivity. But it is also important to be able to properly understand the obtained experimental data and to consider how carriers move in response to the applied field.

Charge carriers are constantly undergoing collisions, energy and momentum exchanges, and scattering into other states [68]. Of these, scattering plays an important role, as different scattering rates can give us an understanding of their origin, whether it is defects, other carriers, or even phonons. The carrier scattering rate contributes to the overall scattering rate, and can be used as an identification factor. Let's briefly take a look at the typical scattering mechanisms.

Every material has defects that can be divided into either neutral or ionized categories.

Ionized defect scattering is usually dominant due to the interaction of a charge carrier with the electric field. Mobile carriers are attracted by the defect, which screens the electric potential exponentially on a length scale given by the Debye length, $L_D = \sqrt{\epsilon k_b T/e^2 n}$. The higher kinetic energy (higher temperatures $T > 100K$), the less effect it has on the initial momentum of the carrier, since the carrier spends less time in the effect of the defects. This can be characterized by $\tau(k) = \tau_0(E/k_bT)^s$, where s is a characteristic exponent for ionized defects [68].

Another form of scattering is carrier-carrier scattering. It can be binary, such as electron-electron, hole-hole, or electron-hole scattering, and collective when an electron or hole scatters from plasmons. In electron-electron or hole-hole scattering, the total energy or momentum of the distribution cannot be changed by self-scattering. As such, the mobility is only affected through higher moments of the distribution. For electron-hole scattering, however, in the center-of-mass frame of reference the event looks exactly like impurity scattering, and it can contribute to a relaxation of the current. The scattering rate is calculated in a classical regime to be $\frac{1}{\tau} \approx n|\ln n|$, approximately linear with excitation density [68].

For carrier densities below the dominating regime of carrier-carrier scattering, the most important scattering mechanism at room temperature is due to carrier phonon scattering, provided carriers have thermalized to the lattice. As the lattice moves it causes a change in the lattice constant, which in turn causes a change in the band structure of the semiconductor. This perturbation leads to scattering of a charge carrier moving through the lattice. Both acoustic and optical deformation potentials play a role, which act respectively through the strain and displacement of the lattice. In polar semiconductors, the local variations in lattice spacing leads to a temporary change in the dipole moment between the positively charged and the negatively charged atoms. This sets up an electric field that can scatter charge carriers very efficiently, either through polar acoustic (piezoelectric scattering) or polar optical phonons. The scattering time and temperature dependence can be shown as $\tau(k) = \tau_0(E/k_bT)^s$ [68].

In this section, we outline the three most common theoretical models of optical conductivity: the Drude model, the Lorentz model, and the Drude-Smith model.

2.4.1 Drude Model

The most commonly used model for describing conductivity is the Drude model. It was proposed by Paul Drude in 1900 to explain the transport properties of electrons in materials [69]. This model treats electrons and holes as non-interacting particles that are free to move in an external electric field. The average time between collisions of carriers with ion cores and other scattering centers is τ, scattering or relaxation time. It is related to another important concept, the mean free path between two scattering processes given by $\lambda = \tau v_t$, where v_t is the average speed at room temperature. After each collision, the direction of the carrier velocity is instantaneously randomized. In an applied electric field, the carrier motion is described by the rate equation of motion:

$$m\frac{d\vec{v}(t)}{dt} = -m\frac{\vec{v}}{\tau} - e\vec{E}(t) \tag{2.25}$$

Taking into account that current density is $\vec{J} = -ne\vec{v}$ and that in a steady-state (DC) field, $\frac{d\vec{v}(t)}{dt} = 0$, a DC conductivity can be obtained using Ohm's law:

$$\sigma_{dc} = \frac{\vec{J}}{\vec{E}} = \frac{ne^2\tau}{m} = \omega_p^2\epsilon_0\tau = ne\mu \tag{2.26}$$

where n is carrier density, e is electronic charge, m is carrier mass, $\omega_p^2 = ne^2/\epsilon_0 m$ is a plasma frequency, and $\mu = \frac{\vec{v}}{\vec{E}} = \frac{e\tau}{m}$ is mobility, which is defined as a ratio of the average drift velocity of the carrier distribution to the electric field.

For the incident light with frequency $\omega < \omega_p$, the dielectric function ϵ is a negative number, and the complex refractive index defined as $\sqrt{\epsilon}$ is imaginary, given by $i\kappa$. In the experiment, this translates to the light not being transmitted but rather being reflected. Alternatively, if $\omega > \omega_p$, ϵ is a positive real number, resulting in propagation of light into the material. This

abrupt change in reflectivity at plasma frequency is known as the plasma edge.

In the case of the AC field $\vec{E}(t) = \Re\{\vec{E}(\omega)e^{-i\omega t}\}$, the solution of Eq. 2.25 will be $\vec{v}(t) = \Re\{\vec{v}(\omega)e^{-i\omega t}\}$. Using this solution gives us the next expression:

$$-i\omega\vec{v}(\omega) = -\frac{\vec{v}(\omega)}{\tau} - e\vec{E}(\omega) \tag{2.27}$$

Taking into account the expression for current density $\vec{J} = -ne\vec{v} = \sigma\vec{E}$, we can rewrite Eq. 2.27 in terms of the complex conductivity:

$$\tilde{\sigma}(\omega) = \sigma_1(\omega) + i\sigma_2(\omega) = \frac{\sigma_{dc}}{1 - i\omega\tau} \tag{2.28}$$

Extracting the expressions for the real and imaginary parts of the conductivity gives:

$$\sigma_1(\omega) = \frac{\sigma_{dc}}{1 + (\omega\tau)^2} \tag{2.29}$$

$$\sigma_2(\omega) = \frac{\omega\tau\sigma_{dc}}{1 + (\omega\tau)^2} \tag{2.30}$$

Note that at $\omega = 0$ (DC), we have $\sigma_1(\omega) = \sigma_{dc}$ and $\sigma_2(\omega) = 0$, such that the complex conductivity is purely real. For short relaxation times, such that $\omega\tau \ll 1$, $\sigma_2(\omega)$ approaches 0 and $\sigma_1(\omega)$ approaches σ_{dc}.

An example of the Drude conductivity for a high-resistivity Si is shown in the Fig.2.18, where the conductivity of Si was obtained by using Eq. 2.28. In the Fig.2.18, the blue and red symbols represent the real and imaginary parts of the measured conductivity, respectively, while the blue and red lines are fits to their data that were performed by using the Drude model as in Eq. 2.28. The data fits well to the Drude model [53].

In general, fitting the experimental complex conductivity spectra in the THz range to the Drude model uses three fitting parameters: the carrier density n, the effective mass m^*, and the relaxation or scattering time τ. If the effective mass m^* is known and frequency-

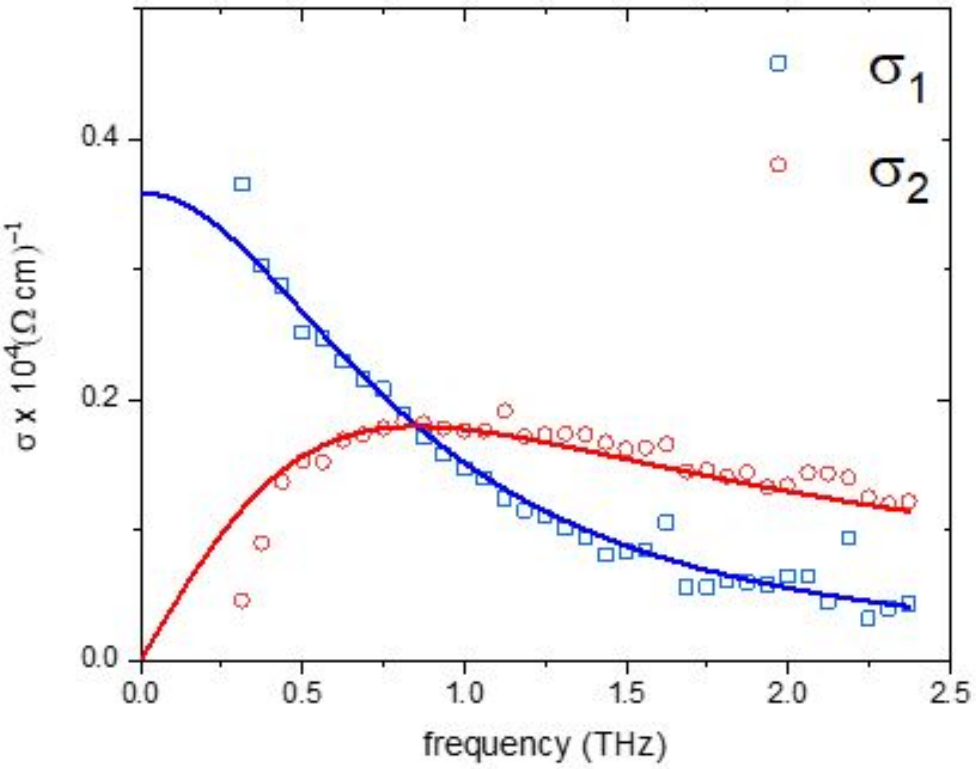

Figure 2.18: Optical conductivity of a high resistivity silicon wafer. Symbols represent the experimental data, while solid lines correspond a fit to a Drude model.

independent over the THz range, carrier density and carrier mobility can be determined from the fit. It is important to note that $\sigma_1/\sigma_2 = \omega\tau$, and a crossover point is at the frequency where $\sigma_1 = \sigma_2$, given by $f_c = 1/2\pi\tau$. Since the curvatures of σ_1 and σ_2 near f_c in the Drude model depend solely on τ, and f_c usually lies in the THz frequency range. However, if $\omega\tau \ll 1$ at 1 THz, σ_2 goes to 0 and σ_1 is roughly independent and equal to σ_{DC} in the experimental frequency range, making fitting of the experimental data to the Drude model unreliable.

2.4.2 Lorentz Model

The Lorentz Theory (1878) is based on the classical theory of light-matter interaction, and is used to describe frequency-dependent polarization due to bound charges. In a simple idealized picture, bound electrons react to an electromagnetic field by vibrating like damped harmonic oscillators. Oscillating dipoles lose their energy through collision processes, resulting in damping. Within the Lorentz model, the displacement x of the electrons in an applied external electric field can be described by the following equation of motion:

$$m\frac{d^2\vec{x}(t)}{dt^2} + \frac{md\vec{x}(t)}{\tau dt} + k\vec{x}(t) = -e\vec{E}_{pump}(t) \tag{2.31}$$

where $1/\tau$ is the damping rate, e is the electron charge, and E is the electric field of the light wave. Each term from the left side of the equation represents the acceleration, damping, and restoring force.The right side term represents the driving force exerted by the electric field of the light of the form $E(t) = E(\omega)e^{-i\omega t}$. This is a single damped harmonic oscillator with force constant k and driven by an electric field. Substituting this equation into Eq.2.31 and looking for solutions of the form $x(t) = x(\omega)e^{-i\omega t}$ gives:

$$\vec{x}(\omega) = -\frac{e}{m}\frac{1}{(\omega_0^2 - \omega^2) - i\omega/\tau}\vec{E}_{pump}(\omega) \tag{2.32}$$

where $\omega_0^2 = k/m$ is the resonance frequency of the oscillator. The displacement of the electrons will result in a dipole moment which varies with the time $p(t)$ and contributes to

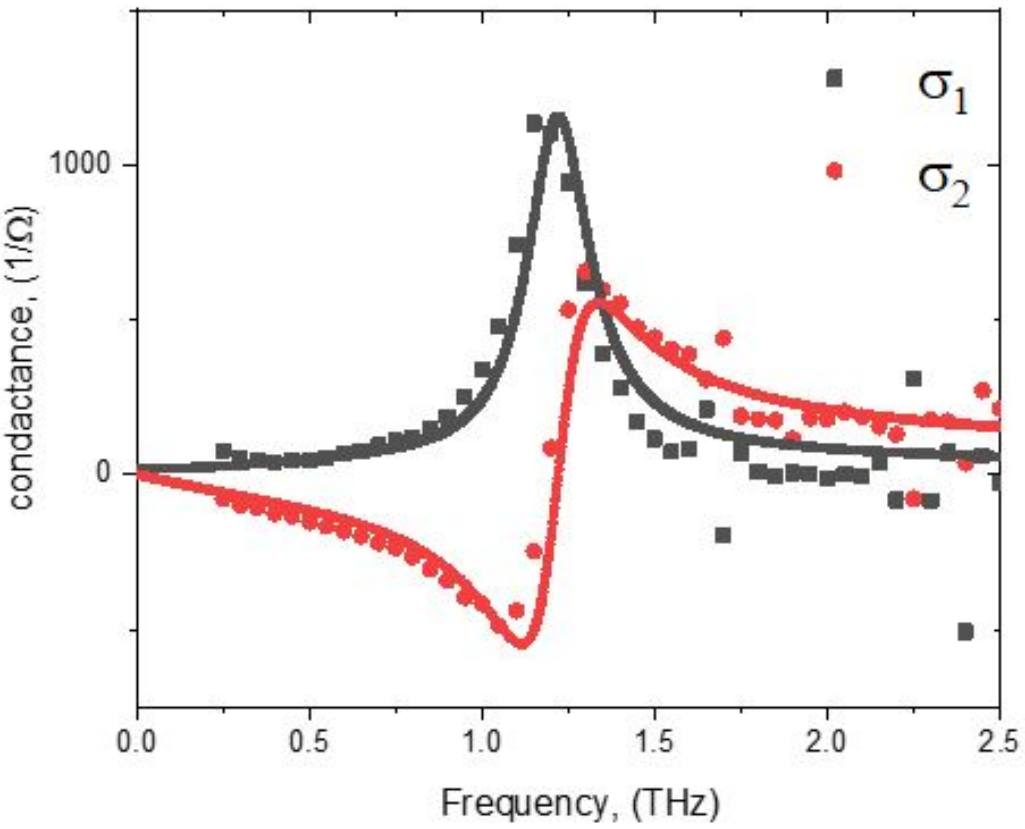

Figure 2.19: Example of the application of the Lorentz model: complex conductivity of BiOI single crystal determined by THz-TDS. The real (black symbols) and imaginary (red symbols) parts of the conductivity are simultaneously fit to Eq.2.36 and 2.37. Resulting global fit is shown as black and red solid lines.

the macroscopic polarization. The dipole moment per unit volume is $\vec{P} = -ne\vec{x}$, and it is related to the electric susceptibility by $\vec{P} = \epsilon_0 \chi \vec{E}$. The dielectric function and the electric susceptibility are related to each other by $\epsilon = \epsilon_0(1+\chi)$, and together with Eq.2.32 will give us:

$$\frac{\tilde{\epsilon}(\omega)}{\epsilon_0} = 1 + \frac{ne^2}{m}\frac{1}{(\omega_0^2 - \omega^2) - i\omega/\tau} \tag{2.33}$$

Using the relationship between the conductivity and the dielectric function

$$\tilde{\epsilon}(\omega) = 1 + \frac{i\tilde{\sigma}(\omega)}{\epsilon_0 \omega}, \tag{2.34}$$

we can rewrite Eq. 2.33 in terms of the complex conductivity:

$$\tilde{\sigma}(\omega) = \frac{ne^2}{m}\frac{\omega}{i(\omega_0^2 - \omega^2) + \omega/\tau} \tag{2.35}$$

Real and imaginary parts for the conductivity are:

$$\sigma_1(\omega) = \frac{\epsilon_0 \omega_p^2 \omega^2 (1/\tau)}{(\omega_0^2 + \omega^2)^2 + (\omega/\tau)^2} \tag{2.36}$$

$$\sigma_2(\omega) = -\frac{\epsilon_0 \omega_p^2 \omega(\omega_0^2 - \omega^2)}{(\omega_0^2 + \omega^2)^2 + (\omega/\tau)^2} \tag{2.37}$$

where ω_p is the oscillator strength. If $\omega_0 = 0$, the Drude model is recovered. It is important to note that for free carriers in the Drude model, σ_2 is always positive, while in the case of bound charges in the Lorentz model, σ_2 is negative for $\omega < \omega_0$. For frequencies well below the resonant frequency, the real part of the conductivity is zero, reflecting the pure polarization response of the bound charges in a dielectric, where the index of refraction is purely real and there is little or no absorption. Thus, for $\omega \ll \omega_0$ and $\omega \ll 1/\tau$, we get:

$$\sigma_2 \approx -\frac{\epsilon_0 \omega_p^2 \omega}{\omega_0^2} \tag{2.38}$$

This means that the low-frequency dielectric constant associated with the Lorentz oscillator is:

$$\epsilon_1 \approx 1 + \frac{\omega_p^2}{\omega_0^2} \tag{2.39}$$

This value is larger than 1 and frequency independent. In this case, the dielectric constant can also be defined by

$$\hat{\epsilon} = \epsilon_1 + i\epsilon_2 = \epsilon_\infty + \frac{i\hat{\sigma}}{\epsilon_0 \omega} \tag{2.40}$$

where ϵ_∞ is the background dielectric constant that contains contributions to the real part of the dielectric function from the Lorentz oscillators at higher frequency, and $\hat{\sigma}$ is due to any additional conductivity introduced into the material, whether by photoexcitation or doping. Thus the total conductivity of the material can be expressed by a summation of the Drude and Lorentz components and referred to as the Drude-Lorentz model:

$$\sigma = \sigma_{Drude} + \sigma_{Lorentz} \tag{2.41}$$

The Lorentz model is typically used to describe vibrational modes in materials. It can also be used to describe the dielectric polarization of excitons at lower frequencies than those associated with the binding energy of the exciton. Fig.2.19 shows an example of Lorentz model applied to the THz-TDS spectrum of a BiOI single crystal. Here, the observed Lorentzian peak at ∼1.2 THz represents a known infrared-active phonon mode.

2.4.3 Drude-Smith model

The Drude model assumes fully elastic isotropic scattering, resulting in complete momentum randomization. Carriers do not have memory of the previous moment before each scattering. In this case, the decay of the current to the impulse field has a single exponential character, with a characteristic time of τ. The resulting Drude conductivity has a maximum σ_1 at the DC value and rolls off at higher frequencies. The imaginary σ_2 rises to a peak at a frequency corresponding to the scattering rate. The Drude model works very well in describing ordered

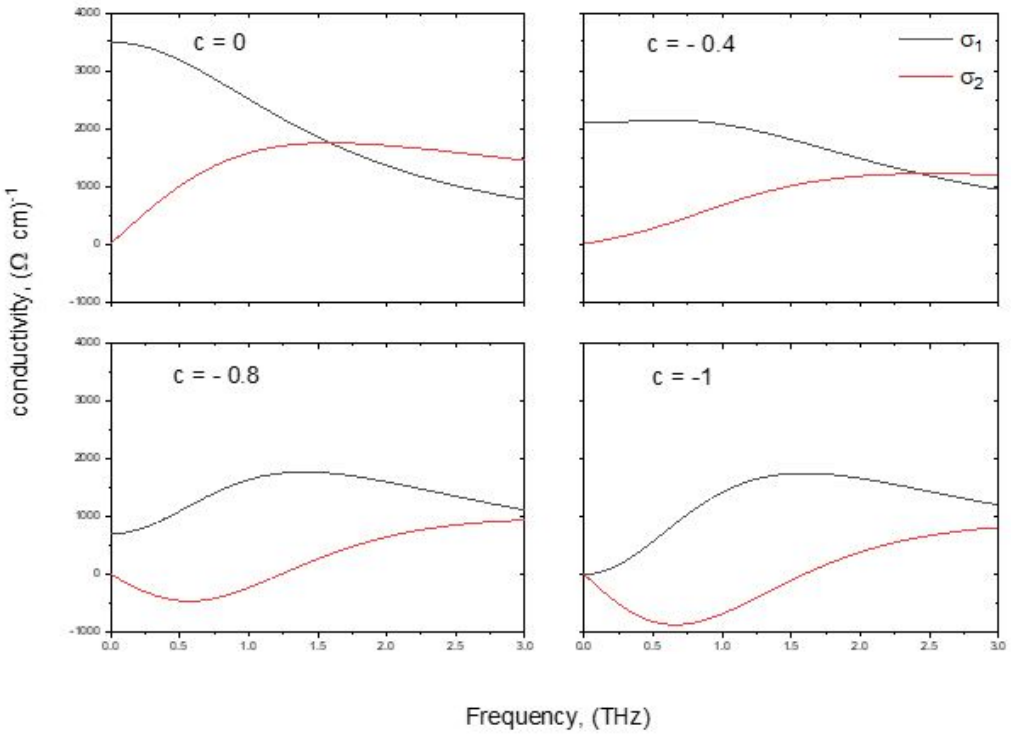

Figure 2.20: Drude-Smith model conductivity example showing the real (black) and imaginary (red) parts of the conductivity.

systems such as single crystalline metals and photoexcited semiconductors, but is not suitable for polycrystalline and disordered systems. Such systems show a suppression in the low frequency σ_1, rising to a peak at non-zero frequency, and a negative σ_2 that represents a capacitive, rather than a Drude-like inductive response. In a modification to the Drude model proposed by N. Smith [70], he introduced 'carrier back-scattering', described both as backwards-biased carrier scattering and as a memory effect, where carriers retain some information of their previous state after scattering. The Drude-Smith model has been widely used to describe complex conductivity of nanostructured and disordered systems [53, 59, 71, 72]. Cocker et. al. [73] used first-principles modeling and Monte Carlo simulations to derive a formalism that is similar in its functional form to the Drude-Smith model but relies on a more physically appropriate picture of diffusion of carriers in systems with partially transmissive barriers. A low frequency applied external electric field establishes a carrier density gradient that leads to a diffusion current in the opposite direction of the drift current, reducing the net conductivity. This result clarified the interpretation of the Drude-Smith model, which remains invaluable to describe conductivity of a structurally confined electron gas. To the first approximation,

$$\hat{\sigma} = \frac{\sigma_{DC}}{1 - i\omega\tau}[1 + \frac{c}{1 - i\omega\tau}] \tag{2.42}$$

Separating the real and imaginary parts yields:

$$\sigma_1 = \frac{\sigma_{DC}}{1 + (\omega\tau)^2}[1 + (\omega\tau)^2 + c(1 - \omega\tau)^2)] \tag{2.43}$$

$$\sigma_2 = \frac{\sigma_{DC}\omega\tau}{1 + (\omega\tau)^2}[1 + (\omega\tau)^2 + 2c] \tag{2.44}$$

where $-1 \leq c \leq 0$. If $c = 0$, the Drude model is recovered. If $c = -1$, this represents a complete back-scattering of the carriers, which corresponds to full carrier localization. Because of this, parameter c is sometimes called a localization parameter.

The Fig. 2.20 shows the real and imaginary parts of Drude-Smith conductivity represented by Eq. 2.43 and Eq. 2.44. It is clear that changes in the back-scattering parameter c results in the suppression of the imaginary part of conductivity, σ_2.

2.5 THz Emission Spectroscopy (TES)

Another important technique within the THz spectroscopy family is THz Emission Spectroscopy (TES). In this technique, the sample itself acts as a THz emitter. By analyzing the emitted THz waveform, we gain insight into the dynamics of underlying processes, such as optical rectification, transient shift and injection currents, spin-currents, ultrafast charge transfer and others [58, 74, 75, 76].

Fig. 2.21 shows a schematic diagram of the TES spectroscopy experiment that was used in the experiments described later. Samples, placed on a rotation stage (not shown), are excited at a normal incidence with 800 nm or 400 nm, 100 fs pulses, and emitted THz radiation is detected in transmission geometry in the same way as THz probe pulses are detected in THz-TDS or TRTS. Polarization of the optical excitation pulse is controlled by a half-wave plate.

From Maxwell's equations, we know that fast-varying currents, as well as transient changes in electronic polarization or magnetization can act as source terms, radiating out electromagnetic pulses. If the underlying processes evolve on sub-picosecond time scales, the result is a very short electromagnetic pulse with frequency contents in the THz range.

Of the many mechanisms for THz generation, two have been described in Section 2.1: transient photocurrents in a biased photoconductive antenna and OR in 2^{nd} order nonlinear crystals. OR is a dominant mechanism of THz emission when the optical excitation photon energy is below the band gap [36, 77]. When the energy of excitation photons is larger than the band gap of a material, real transient currents contribute most to the THz emission. Without external bias voltage, possible mechanisms include the photo-Dember effect, currents driven by built-in surface depletion fields, laser-induced Seebeck effects, photoexcited carrier transfer in heterojunctions, injection and shift currents and related phenomena [78, 79, 80]. Here, we will briefly introduce the known mechanisms underlying bias-free transient photocurrents that need to be taken into consideration while interpreting the results of

TES experiments on 2D chalcogenides discussed in Chapter 4.

2.5.1 Seebeck effect

When an ultrafast laser excitation creates a temperature gradient across the material, the resulting fast diffusion of free majority carriers can emit electromagnetic radiation. THz emission by Seebeck effect has been observed in thermoelectric materials such as BiSnTe and BiTeSe [81]. When evaluating the possible contribution of the Seebeck effect to THz emission in photoexcited materials with pronounced thermoelectric properties, which include GeS, GeSe, and other group-IV layered monochalcogenides [33, 82], it is important to consider experimental geometry. Specifically, if the THz radiation is collected by the area with non-uniform optical excitation, Seebeck currents resulting from the temperature gradients within the THz detection area must be considered. In the experiments described here, emission was collected from a ~ 2 mm diameter spot defined by an aperture, and defocusing the excitation beam to ~ 5 mm diameter spot ensured uniform illumination of the area of interest.

While not directly relevant to the measurements described in this thesis, it is also worth differentiating the ultrafast laser-induced spin Seebeck effect which can also be used as a source of THz emission without any external bias. The spin Seebeck effect at the interfaces between magnetic insulators (such as yttrium iron garnet) and non-magnetic metals (such as Pt, Au or others) has attracted attention for its possible applications in spintronics, as a way to inject spin-polarized currents [48, 83, 84, 85]. Femtosecond laser excitation nearly instantaneously heats the metal layer, resulting in a temperature gradient that drives excited metal electrons toward the interface with the magnetic insulator. There, electrons experience torque from in-plane magnetization that is rectified by two subsequent interactions and results in a net spin current into the metal, which is then converted into a transverse ultrafast charge current density by the inverse spin Hall effect, as mentioned earlier in Section 2.1.4. This current surge acts as a source of a THz electromagnetic pulse. In addition to the possible applications of such structures as a THz source, investigating THz emission by the spin

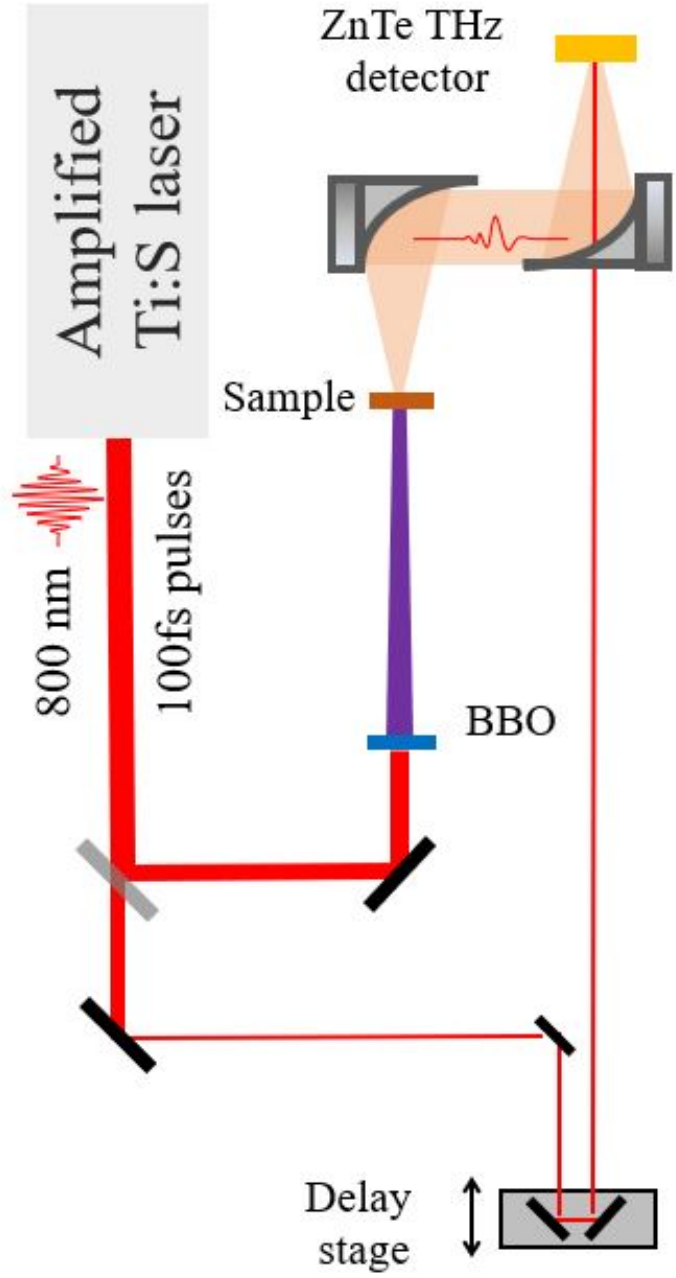

Figure 2.21: Schematic of the experimental setup for TES spectroscopy.

Seebeck effect provides a unique view of the ultrafast spin dynamics not accessible by other means [48, 83, 84, 85].

2.5.2 THz emission observed at oblique incidence: mechanisms

Disentangling the contributions of various ultrafast processes to THz emission in response to the above band gap excitation requires careful consideration of the experimental geometry, viz. sample orientation and polarization, as well as incidence angle of excitation. Specifically, several important mechanisms of ultrafast photocurrents in the absence of external bias can only be observed at the oblique excitation and detection. Examples of such processes include photon drag effect (PDE) and ultrafast photocurrents that flow normal to the sample surface, such as those due to built-in surface fields and the photo-Dember effect, as well as the ultrafast carrier transfer in stacked 2D semiconductors [86, 87]. Experiments described here were all carried out at normal incidence (Fig. 2.21). However, future TES experiments at oblique incidence, outlined in Chapter 4, will allow us to study these effects in 2D chalcogenides, thus we briefly introduce some of them here.

The **photon drag effect (PDE)** originates from photon momentum, which has been transferred to the free carriers via phonons after excitation [88]. It vanishes in experiments carried out at normal incidence. The PDE is allowed in all materials, whether they possess inversion symmetry or not, and can occur for both inter-band or intra-band transitions. However, the energy and momentum conservation imply that momentum transfer from photon to electron (hole) requires participation of the lattice via the electron-phonon interaction. Since $ka \ll 1$, where k is the wave vector and a is the lattice parameter, the photon-drag current in most materials is negligibly weak. On the other hand, the acquired momentum and, hence, the drag current survives for only the momentum relaxation time τ_p, which is also determined by the interaction between carriers and phonons. That is, the stronger the electron-phonon coupling, the higher the momentum transfer rate and the shorter the momentum relaxation time [89, 90]. For 2D materials, large PDE has been theoretically predicted and observed in

graphene, owing to the large carrier mobility and low carrier relaxation rate [90, 91].

Ultrafast photocurrents along the surface normal can be driven by the **built-in surface depletion fields** formed by the band bending at the surface. The magnitude and direction of the built-in surface fields, and therefore the amplitude and polarity of the emitted THz pulses, are sensitive to surface roughness, composition, and the presence of defects that act as charge traps [92, 93, 94, 95]. This sensitivity of the THz emission to the surface properties inspired development of Laser THz Emission Microscopy, where oblique incidence optical excitation is focused to a sub-μm spot and scanned over the sample surface to map out local defect distribution [96, 97]. Application of TES to determine the band bending at the surface is particularly important for unambiguous identification of Dirac surface states in 2D chalcogenide topological insulators Bi_2Se_3 and Bi_2Te_3 [76, 85, 98].

THz emission by built-in surface depletion fields must be disambiguated from emission by **photo-Dember effect** currents that also flow along the surface normal. In the photo–Dember effect, ultrafast photogeneration of charge carriers in the vicinity of a semiconductor surface can result in the formation of a transient charge dipole owing to the difference of mobilities (or diffusion constants) for holes and electrons, leading to an effective charge separation in the direction perpendicular to the surface. This effect is present in most semiconductors but it is particularly strong in narrow-gap semiconductors with high electron mobility such as InAs, Te, InSb [86, 87].

2.5.3 Shift and Injection currents

At the normal incidence geometry resonant, above band gap excitation can result in THz emission due to shift and injection currents, depending on the polarization state of the excitation pulse and the symmetry of the semiconductor structure. These processes were first described in terms of nonlinear susceptibility by Sipe et al. [36]. In this situation, when a pulse with a center frequency ω_0 and temporal electric field $E(t) = \int d\omega \tilde{E}(\omega) e^{-i(\omega-\omega_0)t}$ interacts with a semiconductor, the components $\tilde{E}(\omega)$ and $\tilde{E}(\omega - \Omega)$ induce a nonlinear po-

larization $\tilde{P}(\Omega)$ via $\chi^{(2)}$, where Ω is the sum of optical driving frequencies in the susceptibility tensor. Neglecting carrier scattering effects and ignoring explicit tensor notation, for $\Omega \ll \omega$, $\chi^{(2)}$ takes the form:

$$\chi^{(2)}(-\Omega,\omega,-\omega+\Omega) = \chi_2'(-\Omega,\omega,-\omega+\Omega) + \frac{\sigma_2(-\Omega,\omega,-\omega+\Omega)}{-i\Omega} + \frac{\eta_2(-\Omega,\omega,-\omega+\Omega)}{(-i\Omega)^2} \quad (2.45)$$

The first term represents the nonresonant (rectification) component and reflects displacement of virtually excited carriers; it is nonzero for all ω, since all pairs of valence, conduction bands separated by a band gap E_g' with $\hbar\omega < E_g'$ can make a contribution. The other two terms are associated with the production of carriers in the resonantly excited bands and lead to electrical current. The second term arises from the spatial shift of the center of charge during excitation and leads to a **shift current** if the subsequent carrier scattering has an isotropic component. The third term reflects quantum interference between different pathways (involving different polarization components of the same beam) linking the same initial and final states in the valence and conduction bands. For materials of appropriate symmetry, it can lead to injection of polar distributions of carriers and is therefore known as an **injection current**.

Since carrier current is related to the time-derivative of the optically induced polarization density, it can be shown that the rectification and shift currents induced by transform-limited optical pulses take the form:

$$J_{rect}(t) = 2\epsilon_0\chi_2'\frac{\partial}{\partial t}E(t)E^*(t) \quad (2.46)$$

$$J_{shift}(t) = 2\epsilon_0\sigma_2 E(t)E^*(t) \quad (2.47)$$

The rectification current follows the time derivative of the optical pulse envelope whereas

the shift current follows the envelope directly.

Shift and injection currents arise from different physical mechanisms and possess different crystal symmetry properties [35]. The shift current, which has also been referred to as "above band-gap optical rectification" or the "linear photovoltaic effect," is the result of a shift of the center of charge within a unit cell during optical excitation, e.g., during the electron transitions from the valence to the conduction band. The injection current, which has also been referred to as the "circular photogalvanic effect" occurs in only 18 of the 21 noncentrosymmetric crystal classes and involves the generation of a polar distribution of charge in momentum space due to interference between absorption processes induced by orthogonally polarized beams. It is maximal for circularly polarized excitation light. It leads to a polar distribution of electrons or holes in momentum space, resulting in current injection that temporally follows the optical intensity but whose decay characteristics are related to momentum scattering [75, 99]. These currents can be distinguished by their dependence on the optical polarization and sample orientation and, in principle, by their temporal behavior.

Chapter 3

Ultrafast carrier dynamics in 2D nanomaterials

We have applied TDS and TRTS to study ultrafast carrier dynamics in 2D van der Waals chalcogenides and in nanocrystalline chalcogenides. Studied 2D chalcogenides GeS, GeSe, SnSe, SnS_2, and Bi_2Se_3 stand out among other 2D materials as they are composed of non-toxic, earth-abundant elements and exhibit high carrier mobility and band gaps in the visible to near-infrared range [78, 98, 100, 101, 102]. Some of them also exhibit unique properties, such as room temperature ferroelectricity, strongly anisotropic electronic and optical properties that can be controlled by external fields, and even topological insulator behavior [101, 102, 103]. 2D chalcogenides have been proposed as candidates for chemical sensors, solar energy conversion, and fast electro-optical devices. In this Chapter, we focus on the experimental investigations of the dynamics of photoexcited charge carriers and photoexcitations over sub-picosecond to nanosecond time scales aimed at revealing the relationship between the structural and optoelectronic properties of these 2D chalcogenides. We also describe investigations of carrier dynamics in nanocrystalline chalcogenide materials, specifically, in Bi_2S_3 nanocrystal films, PbS nanocrystal films and across PbS/ZnO heterojunctions.

Work described in this Chapter has been reported in the following publications: Kushnir et al.[104], Zhu et al.[105], Giri et al.[106], and Shi, Kushnir et al.[107].

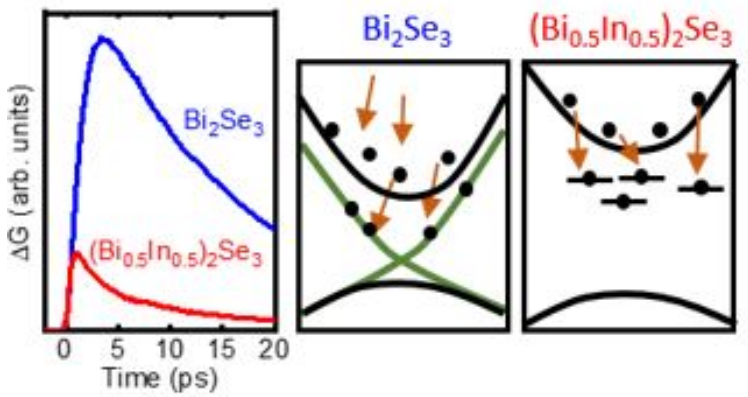

3.1 Photoexcited free carrier dynamics in Bi_2Se_3, $(Bi_{0.75}In_{0.25})_2Se_3$, and $(Bi_{0.5}In_{0.5})_2Se_3$: from topological to band insulator.

Recently, topological insulators (TIs) have drawn much attention due to new transport and optical phenomena that emerge in these systems. TIs are quantum materials where a full band gap in the bulk coexists with gapless metallic surface states (SS) that are topologically protected by time-reversal symmetry and spin-orbit interactions [108, 109]. Bi_2Se_3 is a TI with a bulk band gap of $\sim$0.35 eV and topological surface states that have been observed experimentally and described theoretically [109]. The electrons in these surface states exhibit spin-momentum locking and have small masses, leading to large Fermi velocities and low backscattering. Currently, the application of Bi_2Se_3 in devices is hindered by a lack of a lattice-matched trivially band insulating (BI) counterpart for TI/BI heterostructures. The $(Bi_{1-x}In_x)_2Se_3$ alloy opens up such a possibility. Substitution of Bi atoms with In in $(Bi_{1-x}In_x)_2Se_3$ transforms it from a TI at $x = 0$ to a trivial metallic state at $3\% \leq x \leq 7\%$, and to a true BI at higher In content [110]. Varying In content in $(Bi_{1-x}In_x)_2Se_3$ thus enables tuning the band structure and achieving unique electronic and optical properties. Moreover, the resulting alloy retains the rhombohedral D_3d^5 crystal structure of Bi_2Se_3 for up to

$x = 1$, and is structurally compatible with Bi_2Se_3 [109]. The lattice mismatch between Bi_2Se_3 and In_2Se_3 is only 3%, and high quality Bi_2Se_3 TI layers can be grown by molecular beam epitaxy (MBE) on $(Bi_{1-x}In_x)_2Se_3$ with x up to 75% [103]. This allows the possibility of engineering heterostructures where $(Bi_{1-x}In_x)_2Se_3$ layers with different In content, and therefore different band structures are seamlessly integrated to yield new functionalities. Specifically, $(Bi_{1-x}In_x)_2Se_3$ with In concentration in the trivial BI range can serve as a gate dielectric material or tunnel barrier, essential components of TI field effect transistors, spin valves or topological tunnel junctions.

The electronic band structure of Bi_2Se_3 has been investigated by angle-resolved photoemission spectroscopy (ARPES) and Shubnikov-de Haas measurements, which confirm the presence of spin-polarized Dirac SS that are well separated from the bulk states. In addition to these occupied SS, two-photon ARPES and time-resolved ARPES measurements with $\sim$ 3-eV excitations have identified a second set of unoccupied Dirac SS $\sim$ 1.5 eV above the conduction band minimum that are accessible by optical excitation [111]. ARPES also showed that $(Bi_{1-x}In_x)_2Se_3$ undergoes a transition to a non-topological metallic state for x $\approx$ 4% and finally, to a trivial BI for $x \geq 10\%$. Conventional transport measurements cannot readily disentangle the contribution of the SS states to room temperature electrical conductivity from the large bulk carrier contribution ($\sim 10^{17} cm^{-3}$ to over $10^{19} cm^{-3}$), as most samples are heavily n-doped due to the presence of Se vacancies and antisite defects. In addition to bulk carriers, the contributions of the quantum well states (QWS) that can form in the top 3-4 quintuple layers (QLs) also obscure observation of SS conduction [112].

Recent THz-TDS studies of Bi_2Se_3 were successful at delineating SS, QWS, and bulk state contributions [113]. They found that the mobility of carriers in the QWS is more than 50 times lower than that in the SS ($54 cm^2/Vs$ versus $2,880 cm^2/Vs$), and followed the evolution of the optical conductivity in $(Bi_{1-x}In_x)_2Se_3$ over the sequential phase transitions from TI state to metallic and finally, to trivial BI state as a function of In content from 0% to 25% [114, 115].

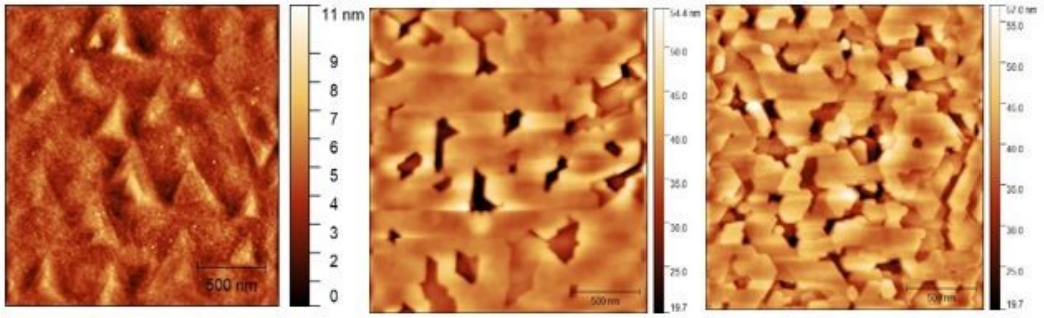

Figure 3.1: AFM images of $(Bi_{1-x}In_x)_2Se_3$ thin films with indium concentration of x=0, 0.25 and 0.50 (left to right) show triangular pyramidal domains in all three samples. This figure was reproduced with permission [107].

We have applied TRTS with 800 nm (1.55 eV) and 400 nm (3.1 eV) excitation to study the dynamics of optically excited carriers and the evolution of photoconductivity in $(Bi_{1-x}In_x)_2Se_3$ with In content increasing to 25% and 50%, well above the onset of the trivial BI phase. $(Bi_{1-x}In_x)_2Se_3$ with x values above the BI threshold is suitable for structurally-compatible insulating layers for TI devices. We demonstrated that photoexcitation injects carriers into the bulk conduction band of Bi_2Se_3, but those free carriers rapidly, over several picoseconds, scatter to the high mobility topological surface states, resulting in high photoconductivity. On the other hand, photoexcited carriers in In-containing films have significantly lower carrier mobility and are weakly confined over mesoscopic lengths scaled by the twin domain boundaries and possible phase segregation. Thus, controlling In concentration during the film growth allows tuning carrier mobility, photoconductivity rise time, and the lifetime of photoexcited carriers, tailoring the ultrafast response of $(Bi_{1-x}In_x)_2Se_3$ films for high speed optoelectronic devices, including TI/BI heterostructure devices.

3.1.1 Experimental methods

$(Bi_{1-x}In_x)_2Se_3$ thin films with different compositions and $\sim$ 100 nm thickness were grown by the MBE on c-plane sapphire ($\sim$ 0.5 mm thick). For indium-containing films, a two-step growth method was used, that involved an initial seed-layer growth with the desired

composition to maintain the correct phase and polytype [103]. Detailed thin film growth information has been reported by Shi et al [107]. The AFM images of the resulting films are shown in Fig. 3.1. The image of Bi_2Se_3 shows pyramid-like domains of $\sim$ 500 nm size that have previously been attributed to twin boundaries [116]. The twin domains form due to relative rotation ($\sim 60^o$ in hexagonal symmetry) of growth front direction. Both In-containing films also show evidence of pyramid like domains, though the domains are smaller, most probably due to the shorter diffusion length of In adatoms compared to Bi adatoms.

Equilibrium complex optical conductivity in $(Bi_{1-x}In_x)_2Se_3$ films was investigated using THz-TDS in a transmission configuration, while the effects of optical excitation were studied using TRTS with either 800 nm (1.55 eV) or 400 nm (3.1 eV), 100 fs optical excitation, as described in Chapter 2.

3.1.2 Equilibrium conductivity in $(Bi_{1-x}In_x)_2Se_3$ films

Equilibrium complex THz-TDS spectra of the three films are shown in Fig. 3.2. Observed conductivity of Bi_2Se_3 is in agreement with previous reports of THz sheet conductance [110, 117]. It exhibits a broad free carrier Drude response at low frequencies that can be extrapolated to a zero frequency, DC value, $G_{DC} \sim (430 \pm 30) \times 10^{-5} 1/\Omega$. In addition to the low frequency Drude free carrier response, the THz complex conductivity of Bi_2Se_3 contains a strong contribution of a bulk infrared-active in-plane α-phonon mode at $\sim$ 2 THz. In the absence of a substantial interaction between the bulk phonon and topological SS, the phonon resonance is symmetric, and the overall complex conductance can be described by a Drude-Lorentz conductivity (Eq. 2.41) which combines a Lorentzian to represent the phonon mode, and a free carrier Drude model to account for the free carrier response. In terms of sheet conductance, it can be written as:

$$\tilde{G}(\omega) = \tilde{G}_{Drude}(\omega) + \tilde{G}_{Lorentz}(\omega) = \left(\frac{\omega_p^2}{\Gamma_D - i\omega} + \frac{S_\alpha \omega (\Gamma_\alpha \omega - i(\omega_\alpha^2 - \omega^2))}{(\omega_\alpha^2 - \omega^2)^2 + (\Gamma_\alpha \omega)^2} \right) \epsilon_0 d \qquad (3.1)$$

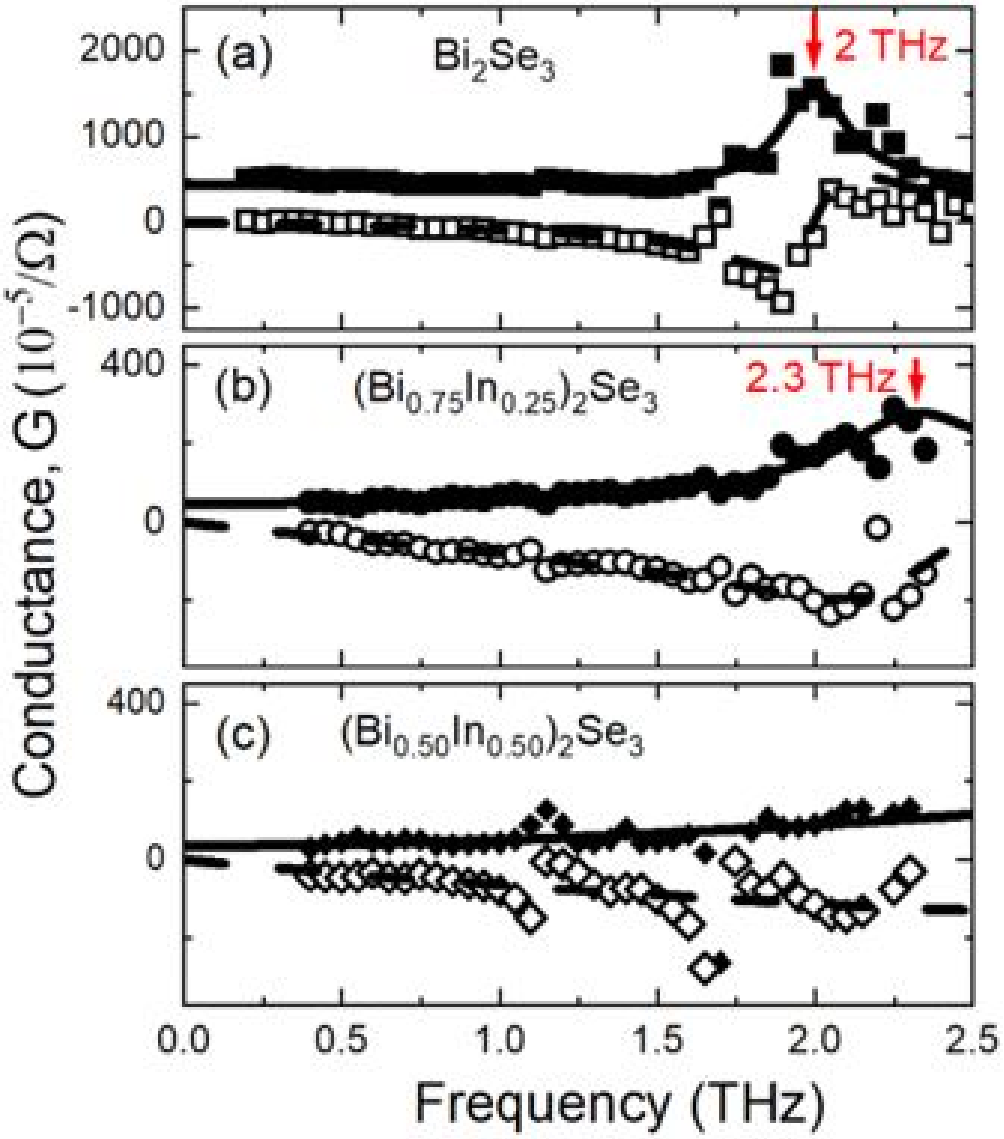

Figure 3.2: THz-TDS spectra: equilibrium conductance of $(Bi_{1-x}In_x)_2Se_3$ films with (a) $x = 0\%$, (b) $x = 25\%$, and (c) $x = 50\%$. Solid and open symbols represent real and imaginary conductivity, respectively, with lines showing global fits of both the real and imaginary conductivity to the Drude-Lorentz model. This figure was reproduced with permission [107].

Here, $\Gamma_D/2\pi$ is the Drude carrier scattering rate,$((\omega_p/2\pi)^2 d)$ is the 2D Drude spectral weight, with $(\omega_p/2\pi)$ representing the plasma frequency, ϵ_0 is the free space permittivity, and d is the film thickness. Lorentzian contribution of the α-phonon with frequency $\omega_\alpha/2\pi$, is given in terms of the phonon damping constant in THz, $\Gamma_\alpha/2\pi$, and S_α, the oscillator strength. Similar to the previously reported studies, the phonon mode broadens, with $\Gamma_\alpha/2\pi$ increasing from ~ 0.25 THz to ~ 0.55 THz for $x = 25\%$. The phonon mode also shifts to the higher energy due to lower atomic weight of In compared to Bi, appearing at ~ 2.3 THz for $x = 25\%$, as reported earlier by Wu et al. [110]. For the even higher In concentration, $x = 50\%$, the phonon mode moves out of the experimental bandwidth and contributes only to a broad positive real and negative imaginary conductance that slowly increases over the experimental spectral window.

The dominant photon contribution and high free carrier scattering rate precludes us from reliably fitting the low frequency free carrier response to the Drude model conductance spectra to estimate carrier scattering time or carrier density. However, prior THz-TDS measurements have demonstrated that the bulk free carriers contribute little to the equilibrium conductivity of MBE-grown Bi_2Se_3 films of 16-100 QL thickness, with 2D conduction channels (SS and QWS) playing a dominant role. Using the combined sheet carrier density of these two channels, $N \sim 3.32 \times 10^{13} cm^{-2}$, and Hall effect mobility of $\mu \sim 623 cm^2/Vs$, reported earlier for a similarly prepared sample, we estimate that $G_{DC} = N\mu e \sim 330 \times 10^{-5} 1/\Omega$, comparable to our extrapolated value (Fig. 3.2(a)). For both In-containing films, G_{DC} is nearly zero, with any possible bulk free carrier response due to residual doping small enough to be entirely obscured by the phonon contribution. This is expected for the trivial BI and agrees with previous Hall measurements. Sharp discontinuities in the spectra at frequencies ~ 1.1 THz and ~ 1.6 THz are experimental artifacts due to the absorption of THz probe pulses by the rotational transitions of water molecules in ambient air. All conductivity fitting was weighted by the spectral amplitude of the reference THz pulse to ensure these artifacts do not affect experimental fitting parameters.

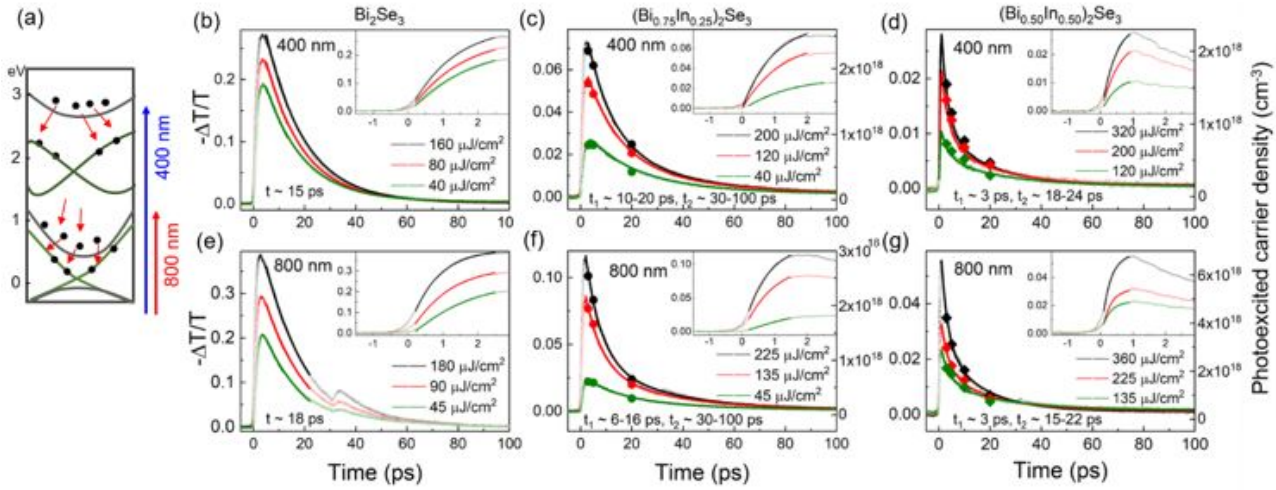

Figure 3.3: (a) Schematic illustrating the band structure of Bi_2Se_3 with two sets of SS. Excitation with 800 nm pulses excites carriers into the lower states of the bulk CB above SS1, and 400 nm pulses can inject carriers into the higher lying states in CB above the SS2. Following excitation, the photoexcited electrons scatter from CB to SS. Transient change in THz ($-\Delta T/T \propto \Delta\sigma$) transmission of $(Bi_{1-x}In_x)_2Se_3$ films as a function of time after photoexcitation with 400 nm (b-d) and 800 nm (e-g) pulses with excitation fluences indicated in the legends. Solid lines in (b-d) represent fits of $-\Delta T/T$ decays to either a single exponential (b, e) or a double-exponential (c, d, f, g) decay functions with the decay times indicated in the panels. Insets show the same data zoomed around the photoconductivity rise, with solid lines showing singe-exponential rise fits. Second peaks seen in (e), (f) and (g) result from re-excitation by an 800 nm pulse reflected from substrate/air interface. In (c), (d), (f), (g), the solid symbols and the scale on the right represent photoexcited carrier density extracted from the Drude-Smith analysis of transient photoconductivity $\Delta\sigma = \Delta Gd$, where d is the layer thickness. This figure was reproduced with permission [107].

3.1.3 Non-equilibrium photoexcited carrier dynamics in $(Bi_{1-x}In_x)_2Se_3$ films.

A simplified schematic of Bi_2Se_3 band structure is shown in Fig. 3.3(a). It includes, in addition to SS within the bulk band gap (SS1), a second set of unoccupied Dirac SS (SS2) located $\sim 1.5 - 1.8$ eV above the bulk CB edge that was previously identified in ARPES measurements[118]. While the excitation with 800 nm (1.55 eV) pulses should predominantly excite bulk free carriers into the lowest CB band, located 300-400 meV above the Fermi edge,the 400 nm pulses can access higher bulk CB states located above the second set of SS.

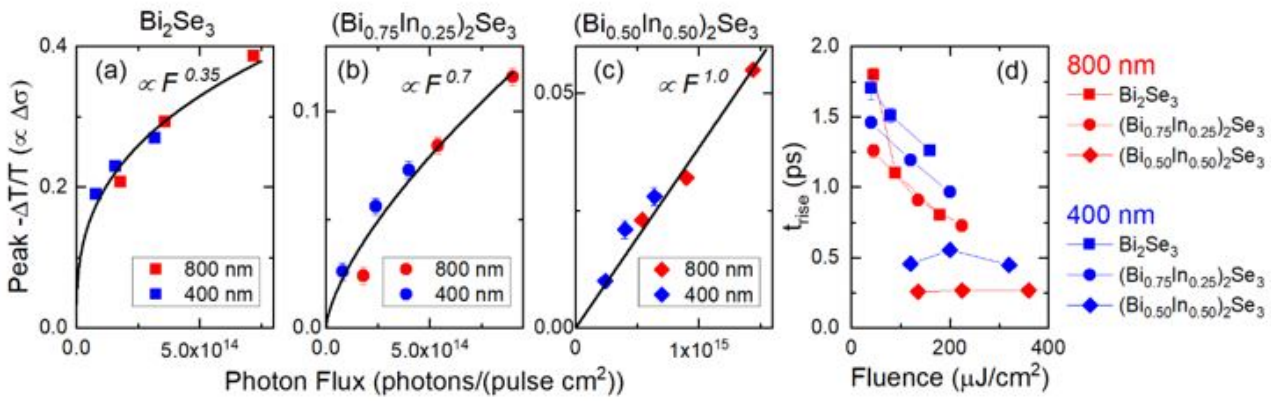

Figure 3.4: (a–c) Peak of $-\Delta T/T$ at 800 and 400 nm as a function of the photon flux in an excitation pulse. Symbols show the experimental data, and solid lines show power law fits with fit results given in the panels. (d) Rise time of $-\Delta T/T$ as a function of the excitation fluence of 800 and 400 nm pulses for all three films. This figure was reproduced with permission [107].

$(Bi_{0.75}In_{0.25})_2Se_3$ and $(Bi_{0.5}In_{0.5})_2Se_3$ are BIs with no surface states and the (indirect) band gap increasing to ~ 0.6 eV and ~ 0.85 eV, respectively, while the higher bulk states that give rise to the onset of direct optical transitions occur at $\sim$1.5 eV and $\sim$1.8 eV, respectively.

Transient dynamics of the photoexcited carriers are captured in $-\Delta T/T$ traces, the negative change in transmission of the THz probe peak as a function of time after photoexcitation (Fig.3.3 (b-g)), which is proportional to the transient photoconductance $\propto \Delta Gd$. We also plot the peak values of $-\Delta T/T$ for all three samples as a function of the photon flux (Fig. 3.4(a-c)), and the photoconductance rise time as a function of excitation fluence, determined by fitting the early time dynamics to a single-exponential rise (Fig. 3.4 (d)).

Here, we underscore several important observations. First, the transient photoconductance ΔG, which is proportional to the negative transient change in peak THz transmission, in Bi_2Se_3 is positive for both 400 nm and 800 nm excitation, for all studied fluences and times after excitation, contrary to a transient suppression of THz sheet conductance in thinner ($<$ 20 QL) films in prior studies. Direct photoexcitation of SS, just like photoexcitation of carriers in graphene, results in their rapid thermalization and an emergence of a population of hot carriers subject to an increased scattering rate, resulting in lower conductivity observed

in these studies. In ∼100 QL films studied here, photoexcitation initially injects free electrons into the bulk CB (Fig. 3.3(a)). Carriers then relax to the lower energies within the bulk CB and finally scatter into the unoccupied SS. This relaxation occurs over few picoseconds, as evidenced by a slow build-up of photoinduced conductance in Bi_2Se_3 shown in the insets of Fig. 3.3 (b, e), as well as in the plot of the rise time as a function of excitation fluence (Fig. 3.4 (d)). The increase in conductance due to scattering of free carriers from bulk CB to unoccupied high mobility SS states overwhelms the expected reduction in conductance due to direct excitation of SS.

Second, the peak transient increase in conductance is significantly higher in Bi_2Se_3 compared to both In-containing films, for comparable or even lower excitation fluence values. This indicates that SS, characterized by significantly higher carrier mobility values than the bulk states, or even the QWS, dominate the photoinduced response of Bi_2Se_3 after the initial buildup of photoexcited carriers in SS. Dependence of the peak $-\Delta T/T$ on of the photon flux (e.g. number of incident photons per unit area of the sample in an excitation pulse) for both 800 nm and 400 nm excitation is shown in Fig. 3.4 (a-c), where the solid lines are power law fits. For each film, peak photoconductance values for both 800 nm and 400 nm excitation fall on the same curves, indicating that each absorbed photon eventually contributes one electron-hole pair to the photoexcited SS population. For Bi_2Se_3, the peak photoinduced change in conductance saturates with increased excitation, as indicated by the power law exponent ~ 0.35 (Fig. 3.4(a)). Saturation occurs as a result of filling of the SS bands. Higher excitation fluences reduce the observed photoconductance rise time. Carrier-carrier scattering at high fluences also plays a role of an additional relaxation channel, accelerating scattering towards the SS. Finally, the rise time for most fluence values appear to be slower for 400 nm excitation, likely an indication of the slower scattering of bulk carriers to SS2.

The peak also shows signs of behavior indicated by a power law exponent of ~ 0.7 (Fig. 3.4(b)), albeit weaker, for $(Bi_{0.75}In_{0.25})_2Se_3$. $(Bi_{0.75}In_{0.25})_2Se_3$ film also has a fluence dependent rise time, comparable to that of Bi_2Se_3, while for $(Bi_{0.5}In_{0.5})_2Se_3$ film, the rise time is

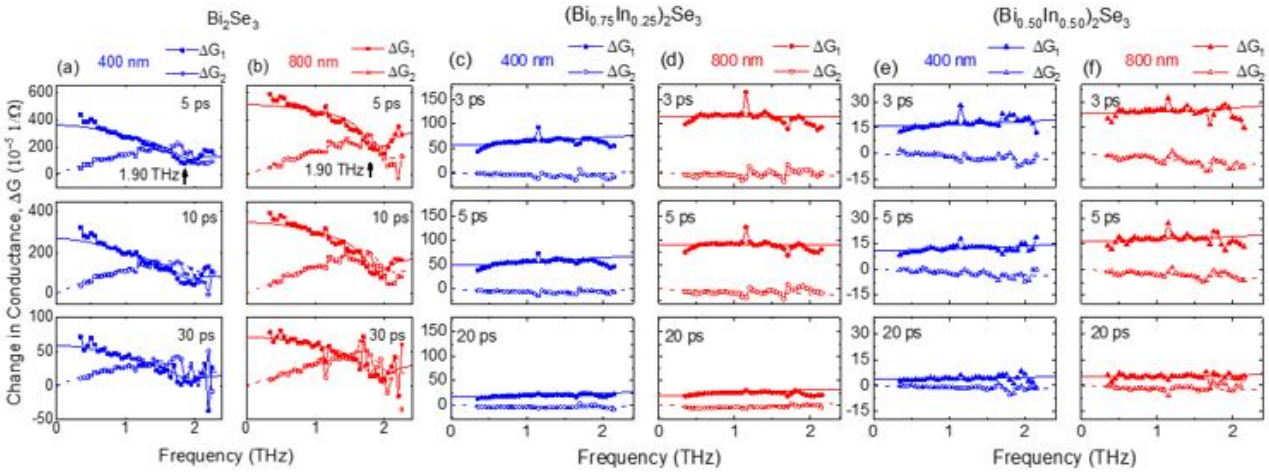

Figure 3.5: Photoinduced change in THz conductance in $(Bi_{1-x}In_x)_2Se_3$ films at different times after excitation with fluences of 200 $\mu J/cm^2$ for 400 nm (shown in blue) and 225 $\mu J/cm^2$ for 800 nm (shown in red). Solid and open symbols indicate the real (ΔG_1) and imaginary (ΔG_2) components of the transient conductance change. Solid and dashed lines show are global fits of ΔG_1 and ΔG_2 to a Drude–Lorentz model (Eq.3.1) for Bi_2Se_3, and the Drude-Smith model (Eq. 3.2) for Bi_2Se_3, $(Bi_{0.75}In_{0.25})_2Se_3$, and $(Bi_{0.5}In_{0.5})_2Se_3$. This figure was reproduced with permission [107].

short and not dependent on fluence, $\sim$ 260 fs for 800 nm excitation, and $\sim$ 500 fs for 400 nm excitation. Carriers in both In-containing films are still excited well above the CB minimum. Many of them rapidly become trapped by bulk defect states or trap states associated with the twin boundaries over the time scales smaller than our experimental time resolution ($<$ 200 fs). In the absence of SS, the remaining carriers relax within the CB, likely ending up in lower energy, higher mobility bands. Filling and emptying of those higher mobility CB states may lead to a relaxation bottleneck, observed as a slow rise time in $(Bi_{0.75}In_{0.25})_2Se_3$ at low excitation fluence values. As increased fluence leads to a higher instantaneous carrier density, carrier-carrier scattering processes contribute to accelerated relaxation. We hypothesize that higher density of trap states, combined with a lower excess energy of the photoexcited carriers due to the higher energies of CB states in $(Bi_{0.5}In_{0.5})_2Se_3$ compared to $(Bi_{0.75}In_{0.25})_2Se_3$, accelerate trapping reduce possible band filling effects.

After photoinduced transient conductance reaches a peak, it decays within tens of picoseconds. In Bi_2Se_3, the SS photoconductivity decays to zero with 15-18 ps time constant. In

both In-containing films, photoconductivity follows a two-exponential decay, indicating the presence of at least two carrier-trapping mechanisms. Trap states may be associated with In substitutions, phase segregation, non-uniform In concentration, and twin boundaries. Both decay components are significantly shorter in $x = 50\%$ film (3 ps vs 6-20 ps, and $\sim$ 20 ps vs 30-100 ps), suggesting an approach for tailoring carrier lifetime in $(Bi_{1-x}In_x)_2Se_3$ BIs for applications in high-speed devices by changing In content.

Analysis of the transient complex, frequency-resolved photoconductance at different times after the optical excitation provides a much more granular picture of ultrafast photoexcited carrier dynamics. Examples of those spectra for 400 nm and 800 nm excitation for all three films are given in Fig. 3.5.

Like in the case of static conductivity measured using THz-TDS, spectra of Bi_2Se_3 are dramatically different from those of $(Bi_{0.75}In_{0.25})_2Se_3$ and $(Bi_{0.5}In_{0.5})_2Se_3$; the transient change in conductance is about an order of magnitude stronger for the same excitation fluence values in TI phase, and the spectral shape differs as well. Once the injected carriers scatter to SS, the low frequency transient photoconductance of Bi_2Se_3 is dominated by a Drude response of SS free carriers, described by the first term of Eq. 3.1. In $(Bi_{0.75}In_{0.25})_2Se_3$ and $(Bi_{0.5}In_{0.5})_2Se_3$, the suppressed real photoinduced conductance component ΔG_1 at low frequencies and negative imaginary photoinduced conductance ΔG_2 are indicative of the effects of disorder and back-scattering of charge carriers, typically observed in nanostructured and granular materials. The potential phase segregation and non-uniform In distribution, as well as partially transparent twin domain boundaries may contribute to localization of free optically excited bulk carriers over mesoscopic length scales and impede long-range transport. We analyze photoconductance spectra within the framework of the Drude-Smith model (Chapter 2, Section 2.4) It can be written in terms of film photoconductance as

$$\Delta G_{DS} = \frac{\omega_p^2 \epsilon_0 \tau_{DS}}{1 - i\omega\tau_{DS}} \left[1 + \frac{c}{1 - i\omega\tau_{DS}}\right] d \tag{3.2}$$

where N is the bulk charge carrier density, τ_{DS} is carrier scattering time (related to

the corresponding scattering rate as $2\pi\Gamma_{DS} = 1/\tau_{DS}$). The lines in Fig. 3.5(c-f) are the global fits on the complex change in conductance to to Eq. 3.2. In the absence of highly conductive SS, bulk volume carrier density N can be calculated from the plasma frequency as $N = (\omega^2 \epsilon m^*)/e^2$, where $m^* = 0.15 m_e$ is the carrier effective mass[103]. Time- and excitation-dependent instantaneous photoexcited carrier density values obtained from the fitting the frequency-resolved complex photoconductance spectra of $x = 25\%$ and $x = 50\%$ films at 3 ps, 5 ps and 20 ps are shown alongside the $-\Delta T/T$ decays in Fig. 3.3 (c-g). We find that the photoconductivity decay tracks photoexcited carrier density for all excitation fluence values. Using those values to estimate the photoexcited carrier density that corresponds to the peak photoconductivity, and comparing it to the total injected carrier density estimated from the photon flux, we find that only 3-5% of all carriers contribute to the observed photoconductivity, while the vast majority are lost to rapid trapping.

The c-parameter values for In-containing films at different excitation fluence values and times after excitation are shown in Fig. 3.6. In both samples, localization of carriers is pronounced, and it is stronger in $x = 50\%$ film. We also find that the c parameter becomes slightly more negative with time after excitation, going from $\sim$ -0.55-0.65 to $\sim$ -0.7 in $(Bi_{0.75}In_{0.25})_2Se_3$, and from -0.7 to $\sim$ -0.8 in $(Bi_{0.50}In_{0.50})_2Se_3$. Such behavior of photoinjected carriers is common among nanocrystalline or granular semiconductors [53, 71, 104, 105]. Carriers become more affected by localization as they thermalize with the lattice. Lower localization at the early times experienced by the carriers excited by 400 nm pulses compared to 800 nm pulses supports this hypothesis. Additionally, carriers trapped at bulk defects and domain boundaries may impact long-range transport of the remaining free carriers. For higher excitation fluence values, injecting more carriers also results in less localization as higher injected hot carrier density takes longer to thermalize with the crystal lattice by emission of phonons.

Finally, using the experimental Drude-Smith parameters τ_{DS} and c, we can also estimate short-range and long-range carrier mobility for photoexcited bulk free carriers as

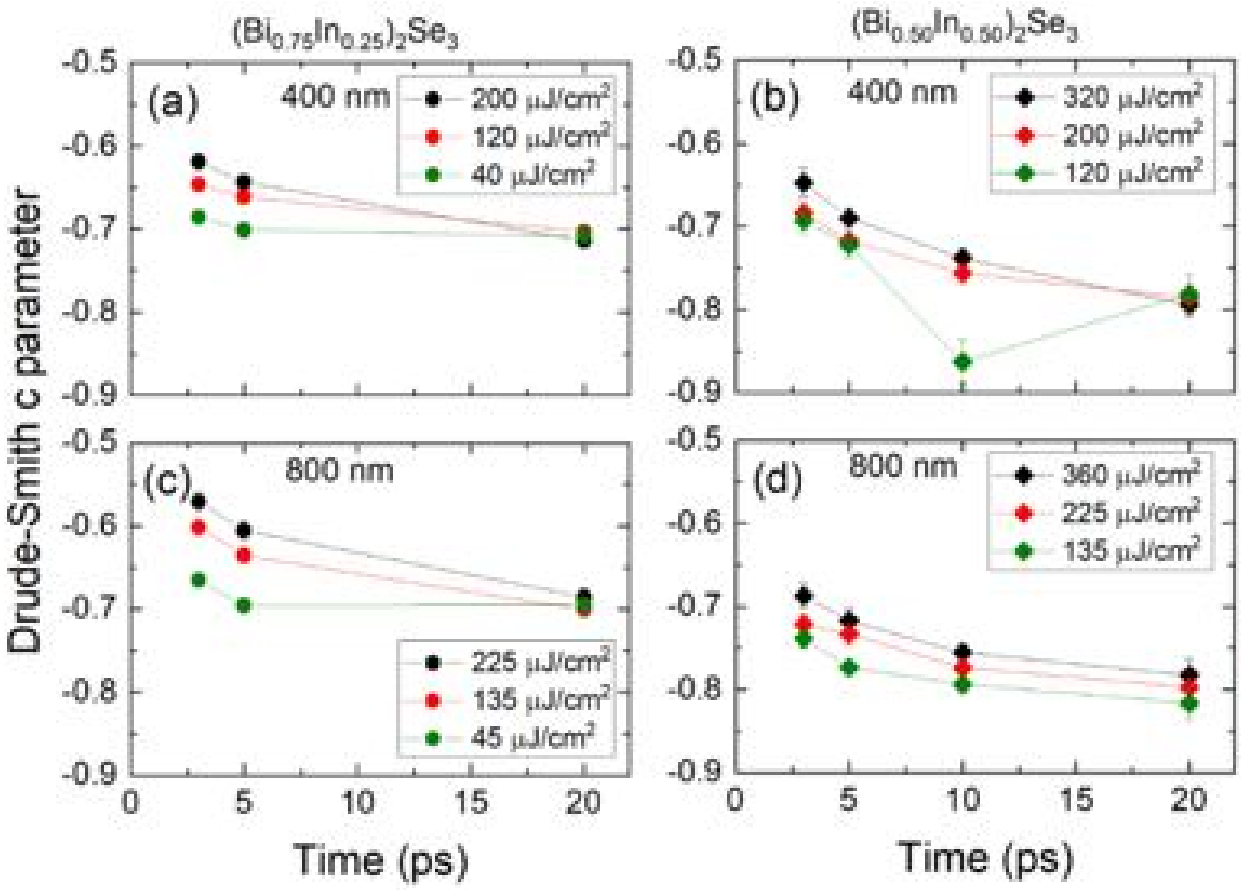

Figure 3.6: Time evolution of the Drude-Smith c parameter for photoexcited charge carriers in $(Bi_{1-x}In_x)_2Se_3$ films with $x = 25\%$ and $x = 50\%$ for 400 nm (a, b) and 800 nm (c,d) excitation. Excitation fluence values are given in legends. This figure was reproduced with permission [107].

	$(Bi_{0.75}In_{0.25})_2Se_3$	$(Bi_{0.5}In_{0.5})_2Se_3$
τ_{DS} (400 nm)	35 fs ± 7 fs	20 fs ± 10 fs
τ_{DS} (800 nm)	50 fs ± 10 fs	15 fs ± 5 fs

Table 3.1: Drude-Smith τ_{DS} values for $x = 25\%$ and $x = 50\%$ films, obtained by fitting photoconductivity spectra to Eq. 3.2. This figure was reproduced with permission [107].

$\mu_{short-range} = e\tau_{DS}/m^*$ and $\mu_{long-range} = \mu_{short-range}(1 + c)$. The summary of the τ_{DS} values is given in Table 3.1.

We find for $(Bi_{0.75}In_{0.25})_2Se_3$, that $\mu_{short-range}$, describing carrier motion over the short distance within individual domains is in the 400-600 cm^2/Vs range. Mobility over macroscopic distances, $\mu_{long-range}$ is as high as 180-270 cm^2/Vs at early times, and decreases to 120-180 cm^2/Vs at later times as the stronger carrier localization sets in. For $(Bi_{0.50}In_{0.50})_2Se_3$, $\mu_{short-range} \sim 200cm^2/Vs$, and $\mu_{long-range}$ decreased over time from 60 cm^2/Vs to 40 cm^2/Vs. This demonstrates that varying In content allows fabrication of $(Bi_{1-x}In_x)_2Se_3$ films with different lifetimes as well as mobilities of optically excited carriers, thus tailoring the properties for a specific application.

In Bi_2Se_3, photoexcited carriers exhibit a Drude response with $c = 0$, as SS are not susceptible to back-scattering. We also observe excitation-induced blue-shift of the α-phonon, which manifests as a negative Lorentzian contribution in the differential conductance ΔG. Blue shift of the α-phonon frequency has been reported in prior studies and attributed to an increased lattice temperature that results from thermalization of optically injected hot carriers. The lines in Fig. 3.5 (a,b) represent global fits of the real and imaginary parts of the differential conductance ΔG and $\Delta\Gamma$ to Eq. 3.1 with negative time- and fluence-dependent Lorentzian amplitude S_α and a damping rate $\Gamma_\alpha/2\pi \sim 0.45$ THz. From the fitting, we obtain both the 2D Drude spectral weight and the Drude scattering rate. We find that, for each excitation wavelength, the scattering rate appears to be a function of the

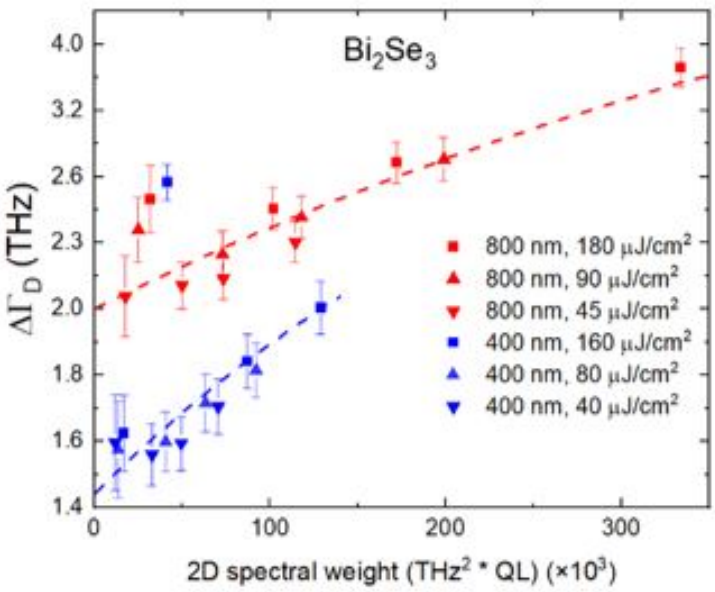

Figure 3.7: Scattering rate Γ_D as a function of photoexcited 2D Drude spectral weight in Bi_2Se_3 at after photoexcitation with 800 nm and 400 nm. Lines are guides to the eye. This figure was reproduced with permission [107].

Drude spectral weight, suggesting that carrier-carrier scattering is a limiting factor on carrier mobility ($\mu \propto \tau_D \propto 1/\Gamma_D$). Data in Fig. 3.7 also show that the scattering rate is significantly lower for the carriers excited with 400 nm. This finding suggests the difference in properties of the two sets of SS, SS1 which becomes populated following excitation with 800 nm pulses, and SS2, which is accessible to carriers injected higher into the CB by 400 nm pulses (Fig. 3.3(a)). Finally, we note here that the scattering times τ_D, corresponding to the lower carrier density limit, are $\sim$ 100 fs for SS1, and $\sim$ 80 fs for SS2. Taking the effective mass in the SS to be $0.07m_e$, we estimate the corresponding carrier mobility values to be $\sim$ 2,500 cm^2/Vs and $\sim$ 2,000 cm^2/Vs.

3.1.4 Conclusion

In conclusion, we have characterized non-equilibrium dynamics of photoexcited free carriers in three $\sim$ 100 QL thick, MBE-grown $(Bi_{1-x}In_x)_2Se_3$ films with $x = 0$, 25%, and 50%, representing the end points of topological insulator- metal-insulator phase transition that

occur as the indium concentration is increased. Excitation of charge carriers with 1.5 eV (800 nm) and 3.1 eV (400 nm) pulses allowed investigation of the carriers injected into different CB energy levels. In the TI limit ($x = 0$), topological surface states dominate both equilibrium and non-equilibrium properties. Carriers that are optically injected into the bulk conduction band relax to the high mobility surface states over few picoseconds. We find that photoexcited carriers in the second set of Dirac surface states, located $\sim$ 1.5-1.8 eV above the conduction band minimum and accessible by 3.1 eV excitation, experience lower scattering and have higher mobility than those in the lower-lying surface states within the band gap. For indium-containing films, photoexcitation generates bulk free carriers that experience partial localization over mesoscopic length scales, commensurate with the presence of the twin domain boundaries. Dynamics of the photoexcited carriers in In-containing $(Bi_{1-x}In_x)_2Se_3$ films, including both the rise time of photoconductivity and the carrier life time, depend on In concentration, demonstrating that specific properties desired for high-speed photonic devices can be achieved by composition engineering of $(Bi_{1-x}In_x)_2Se_3$. As insulating $((Bi_{1-x}In_x)_2Se_3$ is structurally-compatible with TI Bi_2Se_3, ability to tune its optoelectronic properties makes it highly desirable for applications in high-speed optical, electronic and spintronic devices based on TI/BI heterostructures.

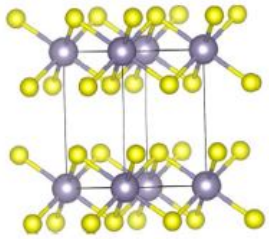

Crystal structure of SnS_2

3.2 Carrier Dynamics in Vertical SnS_2 Nanoflakes and Bulk Single SnS_2 Crystal

Another member of the van der Waals 2D layered materials family is tin disulfide, SnS_2. Its moderate bandgap, environmental stability and high carrier mobility makes it attractive for solar energy conversion applications. Here we explore how nanostructuring SnS_2 in the form of vertically-aligned nanoflakes impacts the lifetime and microscopic conductivity of photoinjected carriers compared to the bulk single crystal SnS_2. This material has potential suitability for applications in electrochemical sensors, photodetectors, photovoltaics, electrocatalysis, and electrochemical energy storage. SnS_2 has a CdI_2-type crystal structure, wherein the triatomic layers are held together by weak van der Waals forces [119]. It is an n-type semiconductor with an indirect bandgap of 2.08-2.44 eV, a high optical absorption coefficient exceeding 104 cm^{-1}, and high carrier mobility of 18-760 cm^2/Vs [120, 121]. In addition, both its elemental constituents have relatively high earth abundance.

One of the promising applications of SnS_2 is in the field of photoelectrochemistry (PEC), specifically for water splitting. The CB and VB energies of bulk SnS_2 straddle the oxidation and reduction potentials of water [122]. However, efficient PEC application of SnS_2 require balancing light absorption and carrier transport, and vertically aligned nanoflakes provide a way to achieve such balance. When the basal planes of SnS_2 are perpendicular to the current collector, photoexcited charges can be transported more efficiently because of the high conductivity along the SnS_2 basal planes [119]. Height of the nanoflakes needs to be

optimized to ensure both optical absorption and efficient charge transport. Theory predicts photocurrents as high as $\sim$ 11 $mAcm^{-2}$ in SnS_2 [123]. However, the previously obtained photocurrent was only $\sim$ 1.5 $mAcm^{-2}$ at the thermodynamic potential for water oxidation (1.23 V_{RHE}) in 0.5 M Na_2SO_4 [124]. Therefore, optimized morphology, high crystallinity, and phase purity are needed to realize high PEC performance from SnS_2 photoelectrodes.

We have conducted a detailed characterization of photoexcited carrier transport in SnS_2 nanoflakes, as well as in a bulk single crystal, using TRTS. We find that intrinsic (intra-nanoflake) carrier mobility in nanostructured SnS_2, 330 cm^2/Vs, is comparable to that in a single crystalline material, 800 cm^2/Vs. Combining the results from TRTS and time-resolved photoluminescence (TRPL) experiments, we found that the optimal length of the vertical nanoflakes for best PEC performance lies between this diffusion length of $\sim 1\mu m$ and the optical absorption depth of $\sim 2\mu m$, which balances the competing requirements of charge transport and light absorption.

3.2.1 Experimental Methods

SnS_2 nanoflake arrays were grown by the close space sublimation (CSS) method. A custom-built CSS system was designed to allow independent control of source temperature (T_{src}), substrate temperature (T_{sub}), and source-substrate separation (d_{ss}). Controlled experiments were carried out to determine the optimal growth conditions. X-ray diffraction (XRD), scanning electron microscopy (SEM), and PEC measurements with a Na_2SO_3 hole scavenger were carried out to characterize the purity, morphology, and PEC performance of the nanoflakes at each growth condition. Single crystal SnS_2 was grown by chemical vapor transport (CVT). Both synthesis methods and detailed structural and chemical characterization were reported by [106].

The photoluminescence (PL) of SnS_2 nanoflakes was measured using a Horiba iHR550 Spectrometer with a 405 nm fiber coupled laser and a Horiba Synapse CCD camera. Similarly, time-resolved photoluminescence was measured using a Becker & Hickl time-correlated single

photon counting system and an ID Quantique single photon avalanche photodiode. The pump used was a 20 picosecond pulsed laser with a frequency of 19.4 MHz, average power of 0.5 μW, and spot size of about 1 mm^2. Hence, the instantaneous peak intensity of the pulsed laser incident on the sample was about 128 mW/cm^2, which is similar to one-sun condition.

Intrinsic mobility of photoexcited charge carriers in SnS_2 nanoflakes and single crystals were characterized by TRTS using a duration of $\sim$ 100 fs and 400 nm pulses for above the band gap excitation, as described in Chapter 2.

3.2.2 Results and discussions

SEM images of a series of SnS_2 vertical nanoflake arrays grown by CSS at different substrate temperatures, T_{sub}, and different distances from the source of SnS_2 to the substrate at fixed $T_{sub} = 450^oC$ are shown in Fig. 3.8. As the T_{sub} is increased from 424 ^oC to 453 ^oC, nanoflakes grew taller and wider SnS_2. Increasing T_{sub} further to 471 ^oC caused the formation of Sn_2S_3 nanorods. Decreasing d_{ss} from 19 mm to 10 mm resulted in taller nanoflakes with increased opacity. In device measurements, described in detail in Ref. [106], the optimal performance of the vertical nanoflake array as a photocathode producing the maximum photocurrent of 4.5 $mAcm^{-2}$ were achieved using $\sim 1.5\mu m$ tall nanoflakes grown with $d_{ss} = 10$ mm.

For comparison, the SEM image of the CVT-grown bulk SnS_2 in Fig. 3.9 shows a uniform, single crystalline structure.

We measured the optoelectronic properties of the optimized nanoflakes and compared them to the properties of the single crystal SnS_2 to gain insights into the origin of the high photocurrent and the reason for the existence of an optimum height of the SnS_2 nanoflakes. First, the Tauc plot in Fig. 3.10 (a) shows the indirect bandgap of SnS_2 to be about 2.1 eV. This indirect band gap also gives rise to a weak, broad PL peak centered at 588 nm (2.11 eV) in Fig. 3.10 (b). The radiative photoexcited carrier lifetime was determined using TRPL decay of the 2.11 eV peak, corresponding to the band gap emission, after exciting with 405 nm laser at near one-sun peak excitation intensity ($\sim 128 mW cm^{-2}$), as shown in Fig. 3.10

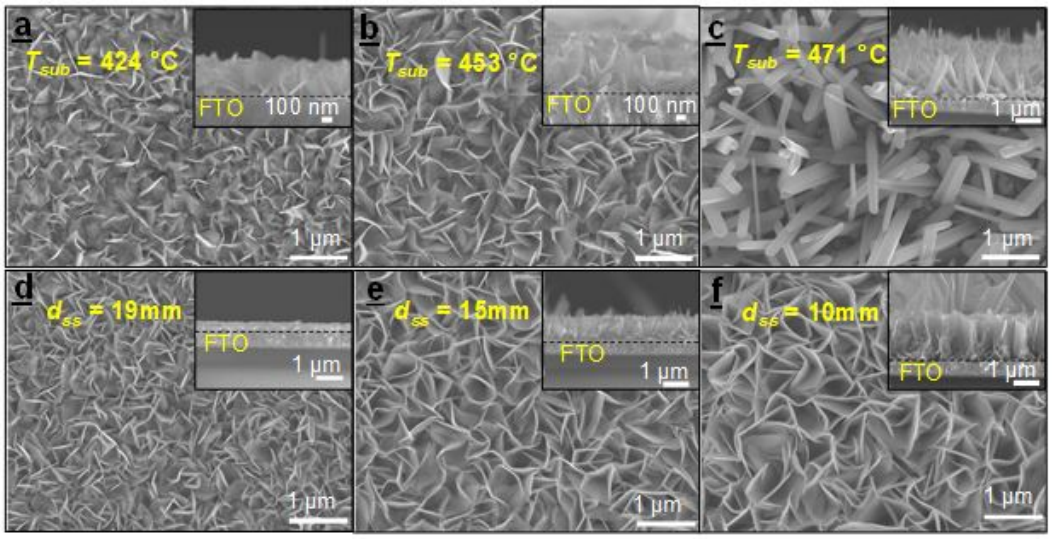

Figure 3.8: Optimization of SnS_2 nanoflake growth by CSS. (a-c) SEM images of nanoflakes synthesized with $T_{sub} = 424\ ^oC$, 453 ^oC and 471 ^oC; (d-f) SEM images of nanoflakes synthesized with $d_{ss} = 19$ mm, 15 mm and 10 mm. The insets show respective cross-section views. This figure was reproduced with permission [106].

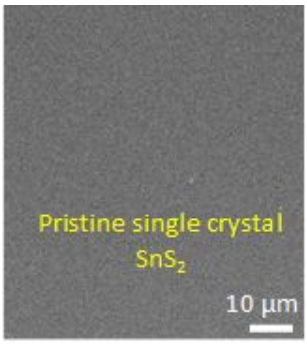

Figure 3.9: SEM image of the pristine single crystal SnS_2. This figure was reproduced with permission [106].

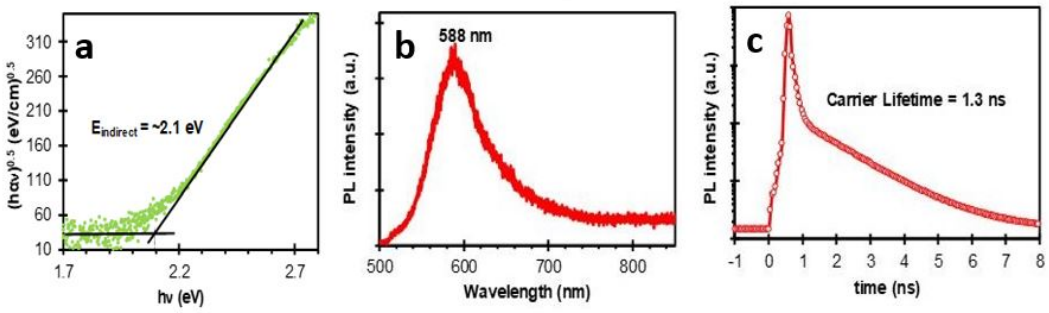

Figure 3.10: (a) Indirect bandgap Tauc plot; (b) steady-state photoluminescence spectrum and (c) time-resolved photoluminescence of vertical SnS_2 nanoflakes following photoexcitation with 405 nm, $\sim$ 20 ps pulses. This figure was reproduced with permission [106].

(c). The observed decay can be fit to a double exponential function, with the fast component of 78 ps due to the TRPL system response time, and the slow component corresponding to the radiative carrier lifetime of $\sim$1.3 ns in SnS_2 nanoflakes. This value provides an upper limit of the free carrier lifetime that is relevant to the device performance, as in systems such as the nanoflake arrays with defects, edges, and disorders. It is possible for the photoinjected carriers to undergo trapping and de-trapping events and eventually to contribute to measured device photocurrent. The other limit of the free carrier lifetime can be obtained by TRTS which is sensitive to free carriers exclusively.

TRTS measurements of 1.5 μm-tall vertical SnS_2 nanoflakes and of a single crystalline SnS_2 are shown in Figures 3.11 and 3.12. In Fig.3.11, samples were optically excited with 28 μ J/cm^2, 400 nm laser pulses. We found that transient photoconductivity in both single crystal SnS_2 and vertical SnS_2 nanoflakes exhibits a multi-exponential decay. In both, the fastest component (2 - 3 ps) is more pronounced at higher excitation fluence values (Fig. 3.12 (a)), and can be thus ascribed to carrier-carrier scattering. The slower, 10 - 15 ps decay observed in vertical SnS_2 nanoflakes likely represents carrier trapping at defect and edge states. Finally, a much slower component observed in both samples, decays over $>$ 250 ps and cannot be determined accurately due to the limitation imposed by the available pump-probe delay. We attribute this long-lived component to the free carrier recombination. Therefore, by combining the information from TRTS and TRPL, we can place the lifetime of

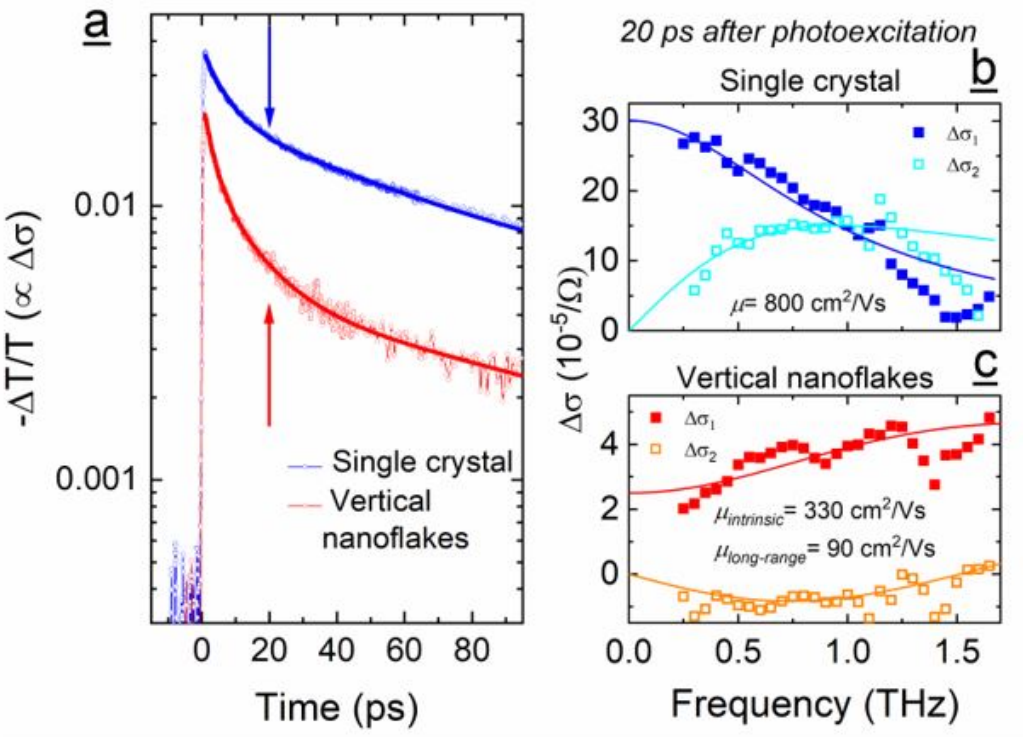

Figure 3.11: (a) Time-resolved terahertz spectroscopy showing picosecond dynamics of photoconductivity in single crystal SnS_2 and vertical SnS_2 nanoflakes following photoexcitation with 400 nm, $\sim$ 100 fs pulses. Real ($\Delta\sigma_1$) and imaginary ($\Delta\sigma_2$) components of THz photoconductivity of (b) single crystal SnS_2 and (c) vertical SnS_2 nanoflakes on quartz measured at 20 ps after the excitation. The lines in (b-c) represent global fit for real and imaginary components of the conductivity to the Drude-Smith model. This figure was reproduced with permission [106].

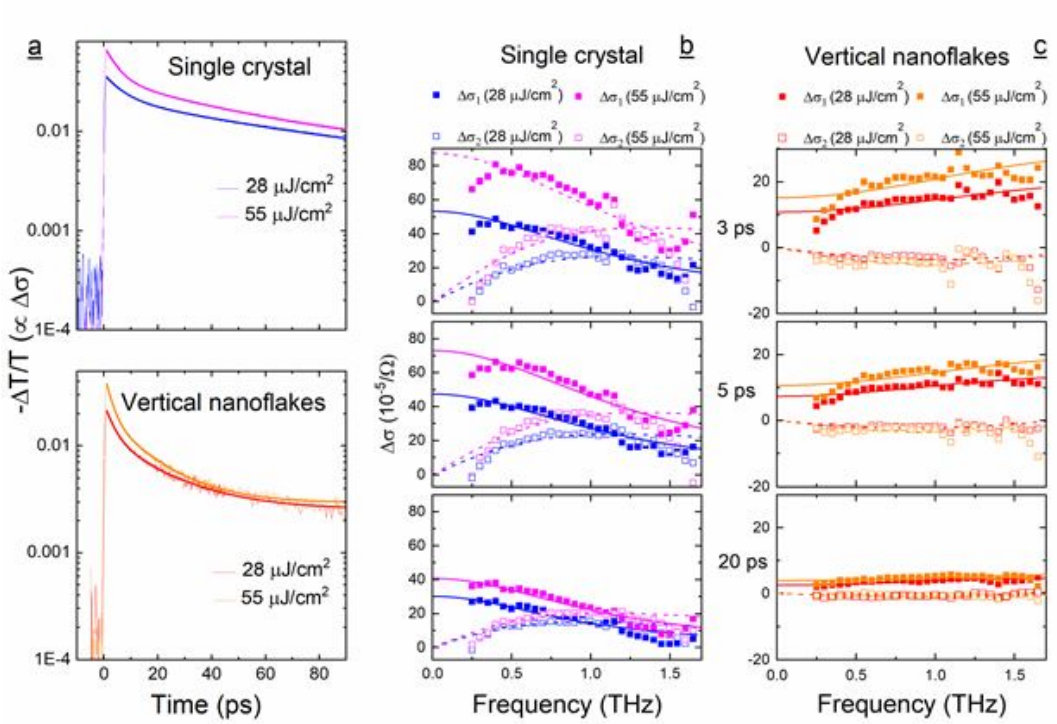

Figure 3.12: (a) Time-resolved THz photoconductivity in single crystal SnS_2 and vertical SnS_2 nanoflakes at two fluences: 28 $\mu J/cm^2$ and 55 $\mu J/cm^2$, following photoexcitation with 400 nm, $\sim$ 100 fs pulses. Real ($\Delta\sigma_1$) and imaginary ($\Delta\sigma_2$) components of THz photoconductivity of (b) single crystal SnS_2 and (c) vertical SnS_2 nanoflakes on quartz measured as a function of THz probe frequency at 3, 5 and 20 ps after the photoexcitation. The lines in (b-c) represent global fits for real and imaginary components of the complex conductivity to the Drude-Smith model. This figure was reproduced with permission [106].

the photoexcited carriers in the optimized vertical nanoflake array in (0.25 - 1.30 ns) range.

Complex, frequency-resolved photoconductivity spectra for both single crystalline and nanostructured samples at 20 ps after excitation with 28 $\mu J/cm^2$, 400 nm pules are shown in Fig. 3.11 (b) and (c). At 20 ps, carrier-carrier scattering is no longer appreciable, and thus intrinsic carrier scattering time and mobility can be determined. In general, the complex conductivity ($\hat{\sigma}$) of both of these samples can be described by Drude-Smith model Eq.2.42.

The c-parameter and τ_{DS} were first determined by fitting the measured frequency-resolved complex conductivity to this model. Then, intrinsic and long-range mobility of carriers in our samples were estimated using Eq. 3.3, where a previously-reported value of effective mass

$m^* = 0.375 m_e$was used [125].

$$\mu_{intrinsic} = \frac{e\tau_{DS}}{m^8}, \mu_{long-range} = \frac{e\tau_{DS}}{m^8}(1+c) \tag{3.3}$$

We find that for single crystal SnS_2, Eq.2.42 reduces to the Drude model (with $c = 0$) and the mobility is estimated to be 800 cm^2/Vs, which is similar to a theoretically-predicted value of electron mobility in monolayer SnS_2. However, for vertical nanoflakes, the localization parameter is nonzero ($c = -0.72$) due to confinement of carriers within individual nanoflakes, and the intrinsic and long-range mobilities are estimated to be 330 cm^2/Vs and 90 cm^2/Vs respectively. This intrinsic mobility is slightly higher than that reported in previous studies and approaches the theoretically predicted one, which is a testament to the high crystallinity of the nanoflakes and low defect concentration. Since the important charge transport in PEC applications occurs within individual nanoflakes, the high intrinsic mobility can improve the overall photocurrent in SnS_2 photoanodes.

Another important factor that impacts the performance of photoanodes is diffusion length (L_D) of the photoexcited charge carriers, which can be calculated from carrier lifetime (τ) and mobility (μ) using Eq.3.4 , where k_B is the Boltzmann constant, T is absolute temperature and e is elementary charge:

$$L_D = \sqrt{\left(\frac{k_B T}{e} \times \mu\right) \times \tau} \tag{3.4}$$

Combining the carrier lifetime (0.25 - 1.30 ns) and TRTS mobility yields the diffusion length of $\sim$ (0.4 - 1.0 μm) in the optimized nanoflake array. As expected, the optimized nanoflake height of $\sim$1.5 μm falls in between $\sim 2\mu m$ thick SnS_2, required to absorb most of the incident photon energy, and the diffusion length.

Finally, Fig. 3.12 provides additional information into photoexcited carrier behavior in single crystalline and nanoflake samples by examining the dependence of photoconductivity from the photoexcitation fluences. We observe that photoconductivity in both single crys-

tal SnS_2 and vertical SnS_2 nanoflake arrays slightly increase with fluence (Fig. 3.12 (a)). More pronounced at higher excitation fluences, the fastest component that correspond to trapping or recombination process linearly depends on excitation fluence, while the slower process saturates so that the photoconductivity at times $\sim$ 50 ps after photoexcitation is low and nearly independent on initial carrier injection. Additionally, analysis of the complex THz photoconductivity as a function of time after optical injection with different excitation fluences provides further insight into the role of edges and surfaces. Fig. 3.12 (b-c) summarizes the results of the transient complex conductivity measurements and illustrates the time evolution of the complex photoconductivity. From here we can see that time evolution of the carrier scattering rate and parameter c related to the carrier localization are independent of excitation fluence, and both parameters indicate that mobile carriers remaining in the nanoflake array at later times after excitation experience less confinement and scattering. We also find that the Drude-Smith c parameter becomes less negative, and scattering time increases by more than a factor of 2 within the first 20 ps after photoexcitation. Based on these observations, we hypothesize that the carriers in the thinnest nanoflakes are trapped and/or recombine at surface and edge trap states rapidly, within the first 5-10 ps, leaving behind the carriers in the thicker nanosheets. Taking the bulk SnS_2 scattering time to be $\sim$ 64 fs, as determined from the single crystal measurements, we find that the average characteristic nanoflake thickness experienced by the mobile photoexcited carriers changes from 6-10 nm at 2 ps after photoexcitation to 40-90 nm at 20 ps. The role of edges vs the surface state in trapping the mobile carriers is being explored using edge passivation by the organic ligands.

3.2.3 Conclusion

In summary, we have applied TRTS in combination with other optical characterization techniques, uv-vis and TRPL spectroscopy, to uncover how achieving the balance between the light absorption and photocarrier lifetime results in efficient photoelectrochemical perfor-

mance of SnS_2 nanoflake arrays. The optimized SnS_2 nanoflakes exhibit high intrinsic carrier mobility (330 cm^2/Vs) and long photoexcited carrier lifetimes (0.25-1.3 ns), which result in large diffusion lengths of $\sim 1\mu m$. We also demonstrated that the thinnest nanoflakes in the array are the most susceptible to carrier trapping and/or recombination as surface and edge states. Photoanodes made of these nanoflakes yield photocurrents as high as 4.5 $mAcm^{-2}$ at 1.23 V_{RHE} under simulated sunlight. High photocurrent results from the combination of excellent optoelectronic properties, unique stepped morphology that exposes multiple edge sites in every nanoflake, and the optimized nanoflake height ($\sim 1.5\mu m$) that balances light absorption and charge transport.

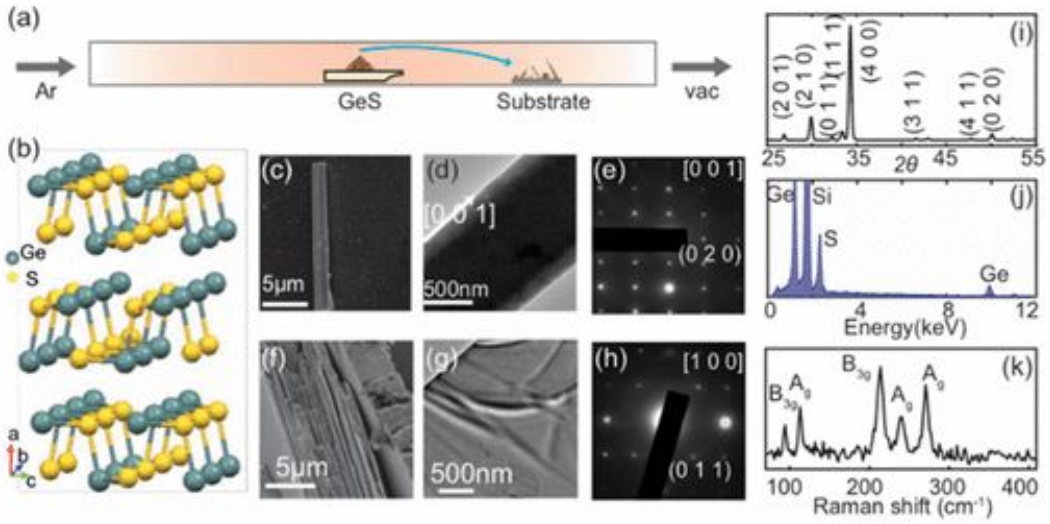

Figure 3.13: (a) GeS is synthesized through the VLS route. (b) GeS has an orthorhombic crystal structure. (c–h) Morphologies grown are flat nanoribbons and sheets with either the flat facet as (001) or (100). Most measurements here are presented on ribbons grown in the (001) direction. (i) XRD, (j) EDS, and (k) Raman characterization show predicted crystal structure and chemical composition. This figure was reproduced with permission [33].

3.3 Transient THz photoconductivity in GeS nanoribbons

A layered van der Waals chalcogenide GeS belongs to a family of group-IV monochalcogenides. Bulk group-IV monochalcogenides have been investigated for decades for their outstanding thermoelectric and electronic properties [126, 127, 128]. Its bulk crystal structure, shown in Fig. 3.13(b) belongs to an orthorhombic Pnma (62) space group and consists of puckered layers separated by a van der Waals gap of about 0.4 nm [129, 130]. Monolayers have a symmetry of the point group mm2. In the bulk, the unit cell includes two adjacent layers. Recent theoretical investigations of GeS and other group-IV monochalcogenides sparked renewed interest in these materials by demonstrating that their monolayers exhibit a giant in-plane switchable spontaneous ferroelectric polarization [78, 129, 131, 132], multi-valley band structure [133], band gap tunability with applied electric field [134], large spin-orbit splitting of 19-86 meV [129], exciton binding energy up to 0.6 eV [132**?**] and

carrier mobility that approaches that of crystalline Si [135]. Broken inversion symmetry in GeS, GeSe, SnS and $SnSe$ monolayers has been predicted to result in anisotropic electronic and optical properties and pronounced second order nonlinear effects that will be discussed in detail in Chapter 4 [78, 101, 102, 136, 137, 138]. With a moderate band gap (∼1.5 eV for multilayer crystals) and high carrier mobility, GeS holds promise for solar energy conversion devices. In this Section, we focus on transient photoconductivity in GeS with an eye on potential applications in photovoltaics and other optoelectronic devices. We apply TRTS to probe photoexcited carrier dynamics in GeS nanoribbons [139].

3.3.1 Sample preparation

GeS nanosheets were synthesized through the vapor–liquid–solid method using established procedures as illustrated in Fig. 3.13 [139]. In brief, fused silica or sapphire substrates were cleaned with acetone and then dried with high-purity nitrogen. Clean substrates were coated with 20 nm Au nanoparticles as a catalyst. GeS powder (50 mg; Sigma-Aldrich) was placed in the center of a quartz tube furnace with substrates downstream. Synthesized GeS nanomaterials (Fig. 3.13 b) are characterized with X-ray diffraction, transmission electron microscopy (TEM), scanning electron microscopy (SEM), energy dispersive X-ray (EDX), and Raman scattering, shown in Fig. 3.13 (c–k). Resulting GeS nanoribbons vary from 10-100 μm in length and 1-100 μm in width, as well as 30-50 nm in thickness.

3.3.2 Results and discussions

Photoconductivity dynamics in an ensemble of GeS nanoribbons after excitation with 800 nm, 100 fs pulses were studied by TRTS as described in Chapter 2. Normalized transient photoconductivity for GeS nanoribbons following excitation with $445 \mu J/cm^2$ is shown in Fig. 3.14 (a). Photoconductivity decays as free photoexcited carriers become trapped at the defect state, both in the bulk and at the nanoribbon edges, and eventually recombine. We find that photoconductivity initially decays over ∼ 60 ps time scales, attributed to carrier

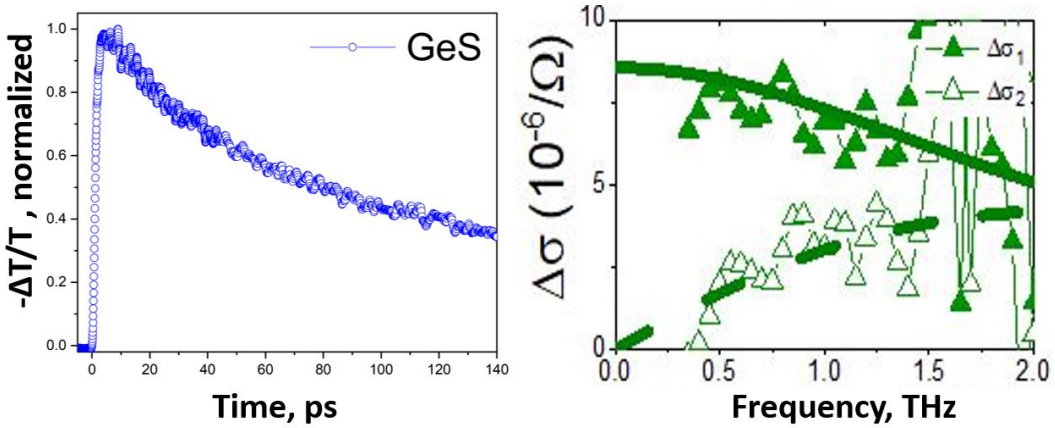

Figure 3.14: (a) Normalized change in THz peak transmission in GeS nanoribbons following photoexcitation with 800 nm, 100 fs pulses.(b) Real and imaginary components of THz photoconductivity of GeS nanoribbons measured at 5 ps after the excitation. The lines represent global fit for real and imaginary components of the conductivity to the Drude model.

trapping, with a much longer lived component corresponding to the remaining free carriers that finally relax by recombination.

A complex, frequency-resolved photoconductivity spectrum 5 ps after excitation is plotted in Fig. 3.14 (b). We find that it is well described by the Drude model, Eq. 2.28 as lateral dimensions of the ribbons are significantly larger that the mean free path of the free carriers, resulting in bulk-like observed THz conductivity. From the Drude fit to the experimental data, we find that the effective scattering times for the pure GeS is $\tau_D \approx 65fs$. The effective carrier scattering time, which determines carrier mobility, includes contributions from all possible carrier scattering processes, such as scattering by defects, interfaces, phonons, and carrier-carrier scattering at high carrier densities. This value yields carrier mobility of $\mu = 350cm^2/Vs$, comparable to literature values for monolayer $\mu = 3680cm^2/Vs$ [135].

The data presented in this Section represent preliminary measurements of ultrafast carrier dynamics in 2D group-IV monochalcogenides. The ongoing efforts and future work, discussed in more detail in Chapter 5, focus on in-plane anisotropy of carrier mobility in GeS, GeSe, and $SnSe$, and on its dependence on excitation polarization, which allows controlled injection of valley-polarized photocarriers. Another important aspect of ultrafast carrier dynamics in

GeS and a related material, GeSe, involves bias-free nonlinear photocurrents occurring within the first picosecond of photoexcitation. These so-called shift photocurrents are discussed in detail in the Chapter 4.

3.4 Charge carrier dynamics in polycrystalline Bi_2S_3 thin films: role of nanocrystal sizes and sulphur vacancies

In addition to the layered, 2D chalcogenides, we have also investigated carrier dynamics in polycrystalline (quasi-3D) systems. One example is thin films of polycrystalline Bi_2S_3. With a band gap of ∼1.3 eV, this is a promising material for efficient generation of electricity or chemical fuels from sunlight [140]. It is typically synthesized using successive ionic layer adsorption and reaction (SILAR), resulting in nanocrystalline films where grain boundaries as well as the sulfur vacancies negatively impact the optoelectronic performance of the material and limit energy conversion efficiency. Density functional theory calculations predict that sulfur vacancies form a deep trap state in the band gap of Bi_2S_3 which can act as a strong recombination channel for photoexcited charges [88]. Annealing solution-deposited Bi_2S_3 in argon at relatively low temperatures ($< 300^oC$) was explored as a way to increase the grain size to $\sim$ 20 nm [141], and sulfurizing of $Bi(NO_3)_3$ in elemental sulfur vapor at 180^oC was proposed as an approach to achieve Bi_2S_3 quantum dots with an average diameter of 6 nm and low impurity content. However, these processes did not lead to highly crystalline Bi_2S_3 with high energy conversion efficiency.

In this work, we have investigated an alternative approach to improving both crystallinity and phase purity of the solution-deposited Bi_2S_3. Polycrystalline Bi_2S_3 thin films were synthesize by high-temperature annealing of solution-deposited nanocrystalline Bi_2S_3 in a sulfur vapor environment. Sulfur annealing increases the grain size and phase purity, fills in sulfur vacancies, and improves optical absorption. We then used TRTS to study the effects of annealing on photoexcited carrier lifetime and mobility. We found that sulfur annealing increases the photoexcited carrier lifetime by orders of magnitude, from sub-picosecond to $\sim$ 30 picoseconds. TRTS also revealed that the intra-grain carrier mobility in the S-annealed

films is $\sim$ $165cm^2/Vs$ and the long-range mobility is $\sim$ $111cm^2/Vs$ at early times after excitation, indicating that carriers are able to hop across grain boundaries, which is critical for the extracting optically injected carriers. These improvements in optoelectronic properties also led to an increase in the internal quantum efficiency of a PEC solar cell device from ~10% to ~40%. These results indicate that annealing in sulfur vapor can produce simultaneously high light absorption and charge separation efficiencies by achieving a carrier diffusion length that is comparable to the light absorption depth, leading to high solar energy conversion efficiencies in Bi_2S_3.

3.4.1 Experimental methods

Bi_2S_3 films with thickness of 150 nm were synthesized by solution deposition and annealing in a sulfur vapor environment as discussed in detail in Ref. [105]. Morphologies, crystal structures, and chemical compositions of the Bi_2S_3 thin films were characterized by SEM, TEM, XRD, XPS. As shown in SEM and TEM images in Fig. 3.15, the crystallite size of the un-annealed Bi_2S_3 nanocrystals was $\sim$ 10 nm, while the average crystallite size of the S-annealed film was calculated to be $\sim$ 45 nm from the XRD pattern and SEM micrographs. Furthermore, the XRD showed that annealing the solution-deposited Bi_2S_3 film in sulfur vapor at 445^oC results in a XRD pattern with peaks that can be indexed to pure orthorhombic Bi_2S_3 (Figure 3.15 (d)), demonstrating that sulfur vapor annealing increases not only the crystallite size of the solution-deposited Bi_2S_3 but also the crystallinity of the grains.

The wavelength-dependent optical absorption properties of the samples were obtained using illumination from a Xe lamp. The PEC measurements were performed in a three-electrode configuration, using a potentiostat under back-side broadband illumination from a Xe lamp. Transient photoconductivity and photoexcited carrier lifetime were analyzed with TRTS using 400 nm optical excitation, as described in Chapter 2. Absorption of both un-annealed and S-annealed Bi_2S_3 films was similarly high at 400 nm. Thus, comparing transient photoconductive response at this excitation wavelength allows us to focus exclusively on the

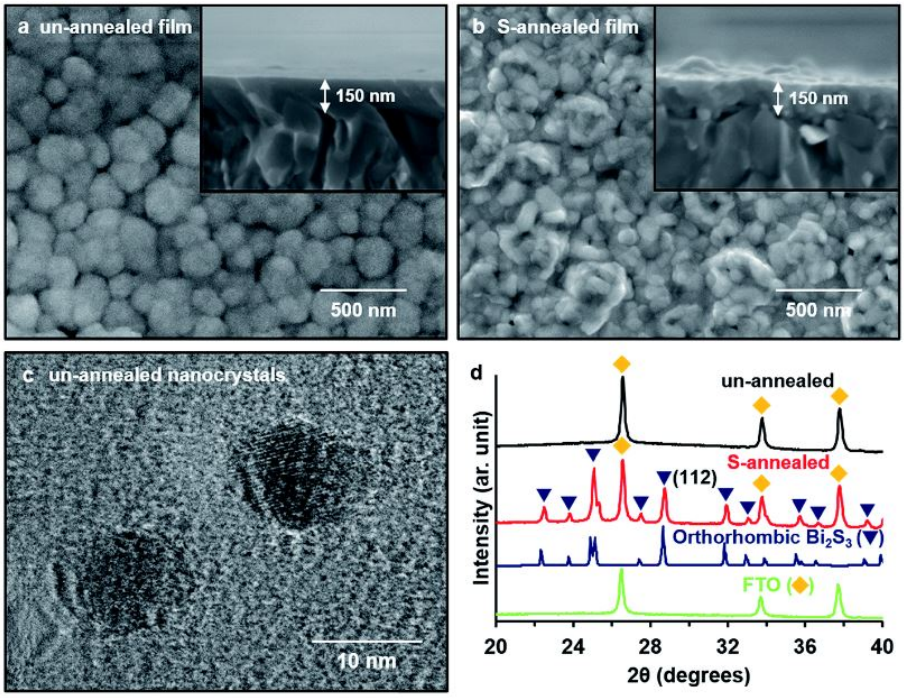

Figure 3.15: Top-view and cross-section SEM images of 10 layers of (a) un-annealed and (b) S-annealed Bi_2S_3 thin films on FTO substrate. (c) TEM image of un-annealed Bi_2S_3 nanocrystals. The background is the amorphous carbon film of the TEM grid. (d) XRD patterns of un-annealed and S-annealed Bi_2S_3 thin films.

effect of annealing on microscopic conductivity and carrier lifetime.

3.4.2 Results and discussion

Transient photoconductivity, represented as a change in transmission of the main peak of the THz probe pulse, $-\Delta T/T$, following excitation of both films with 400 nm, 378 $\mu J/cm^2$ pulse, is shown in Fig. 3.16 (a). We find that peak photoinduced conductivity is more than twice higher in the S-annealed film as a result of a less prevalent fast trapping and recombination of photoinjected charge carriers on a timescale that is shorter than our instrumental response time of about 300 fs. Moreover, photoconductivity of un-annealed film is very short-lived and decays on sub-picosecond time scale due to both rapid carrier recombination inside the small Bi_2S_3 crystallites and fast trapping of photoexcited carriers in trap states at crystallite boundaries. Larger grain size, lower concentration of sulfur vacancies, and reduced number

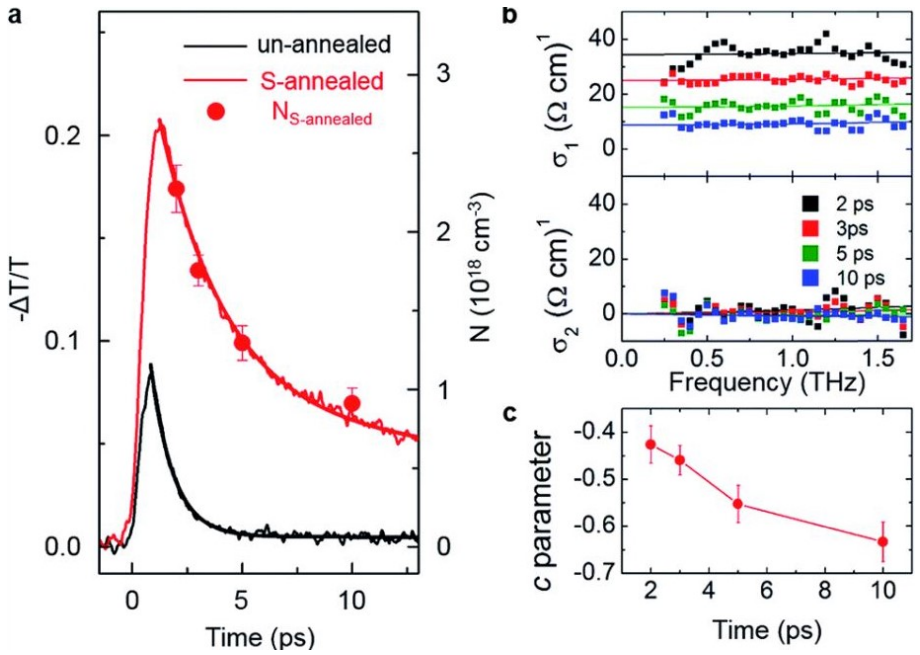

Figure 3.16: Time-resolved THz spectroscopy of un-annealed and S-annealed Bi_2S_3 thin films. (a) Transient photoconductivity (lines) and instantaneous photoexcited carrier density (symbols) for S-annealed film. Smooth lines represent fits of experimental transient photoconductivity to single- (un-annealed) and bi-exponential (S-annealed film) decays. (b) Real and imaginary components of transient photoconductivity at different times after optical excitation for S-annealed film. Symbols represent experimental data, and lines – fits of experimental data to the Drude–Smith conductivity. (c) Drude–Smith c parameter for S-annealed film.

of interface defects in S-annealed Bi_2S_3 film translates into a significantly longer lifetime of mobile carriers (Fig. 3.16 (a)). Photoconductivity in the S-annealed sample follows a bi-exponential decay with a fast ($\sim$ 3 ps) and a slower (30 ps) component. The fast decay time is dependent on excitation fluence, increasing from 2.6 ps to 4.4 ps as excitation is decreased six-fold to 63 $\mu J/cm^2$. This suggests that the process responsible for this fast photoconductivity decay is recombination of mobile carriers. On the other hand, the slower, 30 ps component is fluence-independent and represents trapping of carriers at sulfur vacancies and interface states that do not become saturated in the studied fluence range.

The complex-valued, frequency-resolved THz photoconductivity spectra as a function of time following the photoexcitation are shown in 3.16 (b). The real component of conductivity decreases with time while the imaginary one stays almost unchanged and close to

zero. We analyze this progression by fitting both real and imaginary conductivity to the Drude–Smith model (Chapter 2). Solid lines in Fig. 3.16 (b) are Drude–Smith fits to the experimental complex conductivity. Using the carrier effective mass, $m^* = 0.246m_e$ [142], we have extracted instantaneous photoexcited free carrier density, plotted as circles in Fig. 3.16 (a). We observe that the free carrier density follows the same trend as the bi-exponential decay of photoconductivity, indicating that trapping and recombination of mobile carriers is responsible for the observed transient reduction in photoconductivity while the intrinsic carrier mobility stays unchanged.

The Drude-Smith effective scattering time τ_{DS} (Chapter 2) is determined by both intrinsic, bulk scattering time and the average time between collisions with the grain boundaries $\tau_{boundary}$ as

$$\frac{1}{\tau_{DS}} = \frac{1}{\tau_{bulk}} + \frac{1}{\tau_{boundary}}. \tag{3.5}$$

Effective carrier scattering time τ_{DS} is unchanged over the first 10 ps and equal to 23 $\pm$ 5 fs, corresponding to the carrier mean free path of $\sim$3 nm. As the mean free path is significantly smaller than the $\sim$45 nm average grain size, contribution of grain boundary scattering to the effective relaxation time is negligible, and intrinsic, intra-grain mobility (μ_{int}) can be estimated as

$$\mu_{int} = \frac{e\tau_{bulk}}{m^*} \approx \frac{e\tau_{DS}}{m^*} \approx 165 cm^2/Vs \tag{3.6}$$

However, long-range, inter-grain mobility decreases as carriers, while free to move within the individual grains, become more localized inside those grains. This phenomenon is reflected in the time dependence of the c parameter, which changes from $\sim$ -0.43 $\pm$ 0.04 at 2 ps to -0.63 ± 0.04 at 10 ps after excitation, as has been observed in other polycrystalline systems [56, 71, 72, 143]. This occurs as the barrier heights experienced by the carriers at the grain boundaries increase over time. As carriers get trapped at inter-grain boundaries, the electrostatic field associated with trapped charges increases the height of the potential

barrier experienced by the free carriers. As a result, the long-range, dc-mobility of the film, $\mu_{dc} = (1 + c)\mu_{int}$ decreases as a function of time after excitation from 111 cm^2/Vs at 2 ps to 61 cm^2/Vs at 10 ps. Based on a carrier lifetime, t, of 30 ps and an inter-grain mobility (μ_{dc}) of 61 cm^2/Vs, the carrier diffusion length (LD) can be calculated as

$$L_D = \sqrt{\frac{kT\mu_{dc}t}{e}} \approx 68.6nm \tag{3.7}$$

This carrier diffusion length is similar to the light absorption depth at $\sim$ 70 nm, which suggests that simultaneously high light absorption and charge separation efficiencies can be achieved in the S-annealed Bi_2S_3 thin films, leading to high overall solar energy conversion efficiencies [144]. Low signal-to-noise ratios in the complex conductivity spectra did not permit accurate measurement of mobility for un-annealed Bi_2S_3 films.

3.4.3 Conclusions

We have used TRTS to elucidate the effects of annealing of Bi_2S_3 thin films in sulfur environments. Structurally, this process leads to more, larger crystallites that have less sulfur vacancies. TRTS shows that this improvement in structure significantly (more than 30-fold) increases the lifetime of photoexcited carriers. Over the initial 5-10 ps after photoexcitation, inter-crystallite transport of charges is possible. Device measurements are consistent with these improved optoelectronic properties, as solar energy conversion efficiency is increased four-fold.

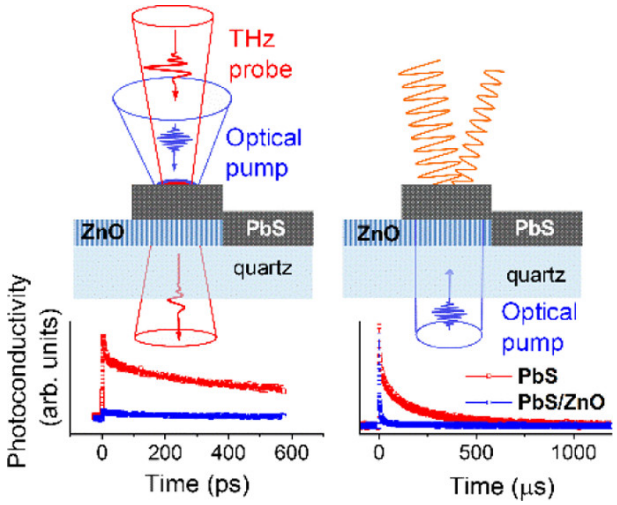

3.5 TRTS as a Probe of Dynamics of Photoexcited Carriers at Heterojunctions

Due to their band gaps in the visible and infrared ranges, the most attractive device applications of chalcogenides use them as light absorbers. This invariably requires extraction of optically injected carriers from chalcogenide absorbers to carrier transport structures. Thus, interfacial phenomena play a critical role in the device operation, and knowledge of carrier dynamics at hetero-interfaces between chalcogenides and candidate carrier transport materials is paramount. Here, we demonstrate how TRTS can be applied to probe carrier injection from a chalcogenide absorber (polycrystalline PbS film) to the candidate charge collector (ZnO). We have applied TRTS (Chapter 2) in combination with time-resolved microwave photoconductivity (TRMPC), a complimentary all-optical technique for probing photoconductivity over longer times scales compared to TRTS, to study the impact of the grain boundaries and interfaces on dynamics of photoexcited charge carriers within the PbS films and at PbS/ZnO interfaces [145]. Narrow band gap bulk-like PbS with high absorption in the infrared paired with a wide band gap metal oxide ZnO current collector holds promise for infrared photodetectors and photovoltaics. However, heterojunction interfaces play a crucial role in device performance, as they often harbor a variety of trap states and re-

combination centers. Surface states at PbS grain boundaries serve as efficient electron traps, and trap-mediated carrier recombination at PbS/ZnO interfaces limits the performance of PbS/ZnO heterojunction photovoltaics and other optoelectronic devices [146, 147, 148]. All-optical tools such as TRTS can provide critical information about the behavior of carriers at interfaces.

3.5.1 Introduction

Owing to its narrow bandgap of about 0.37 - 0.41 eV [146], lead sulfide (PbS) is attractive for infrared photodetectors and solar cells that can efficiently utilize the infrared range of the solar spectrum. Generation of multiple carriers for one absorbed photon in the visible and ultraviolet range has been observed in both bulk PbS and PbS quantum dots, bringing forth the possibility of PbS photovoltaics with efficiencies that exceed the Shockley-Queisser limit [149]. Carrier extraction in PbS optoelectronic devices can be achieved by forming p-n heterojunctions. Here, we have studied carrier dynamics at the the interfaces of a p-type PbS absorber and an n-type wide band gap transparent metal oxide semiconductor ZnO. In this case, the band alignment favors rapid injection of electrons from PbS into the oxide [150, 151]. It has been shown in recent studies using transient optical absorption and time-resolved photoluminescence that lifetimes of photoexcited carriers in PbS quantum dots are reduced in the vicinity of PbS/ZnO interfaces, suggesting carrier injection from quantum-confined states in PbS quantum dots into ZnO. Our focus in this study was on the ultrafast dynamics of photoexcited carriers in bulk-like, polycrystalline PbS and at the PbS/ZnO interfaces.

The average size of the polycrystalline domains in the investigated PbS films are about $\sim$ 150 nm, significantly larger than the 20 nm exciton Bohr radius[152]. Combined with weak exciton binding in PbS [153, 154, 155], this removes excitonic effects from consideration in the studied system at room temperature. Furthermore, PbS crystallites were not capped by organic or inorganic ligands, as the goal of this study is to elucidate the role of PbS grain

boundaries and PbS/ZnO interfaces on carrier dynamics. We compare transient photoconductivity in polycrystalline PbS films that are deposited either on quartz or on a ZnO film. We find that the lifetime of photoexcited carriers in the polycrystalline PbS film deposited on quartz is extremely long, reaching 1 ms, and the intrinsic carrier mobility within the crystallites is large, at $\sim 750 cm^2/Vs$. At the same time, inter-crystallite transport in the film is limited to a short $\sim 10ps$ time window after excitation. At longer times, inter-grain interfaces impede long-range conductivity. On the other hand, the population of photoexcited free carriers in the polycrystalline PbS film deposited on ZnO decays on timescales shorter than our experimental time resolution of $< 300fs$, consistent with previous reports based on transient optical absorption measurements. However, instead of being injected into the highly conductive ZnO layer, we find that the vast majority of those carriers recombine at the ZnO/PbS interface. This conclusion underscores the importance of interface engineering in PbS and other heterojunction optoelectronic devices.

3.5.2 Experimental Methods

Sample Preparation and Characterization

PbS films were deposited at room temperature using a chemical bath containing lead, sulfur precursors, and reducing agent ($NH_2OH \cdot HCl$) [156]. The concentration of $NH_2OH \cdot HCl$ has been adjusted to achieve a nearly single layer of $\sim 150nm$ cubic PbS grains.

Continuous, polycrystalline ZnO films were grown on a portion of a quartz substrate prior to PbS deposition, by a modification of an existing procedure from Zn precursor [157]. The resulting structure, schematically illustrated in Fig.3.17 (a), consists of two distinct regions, one with PbS deposited on ZnO, and another one with PbS grown directly on the quartz substrate. Scanning electron microscopy (SEM) images of ZnO and PbS films on quartz and on ZnO are shown in Fig.3.17 (c-d).

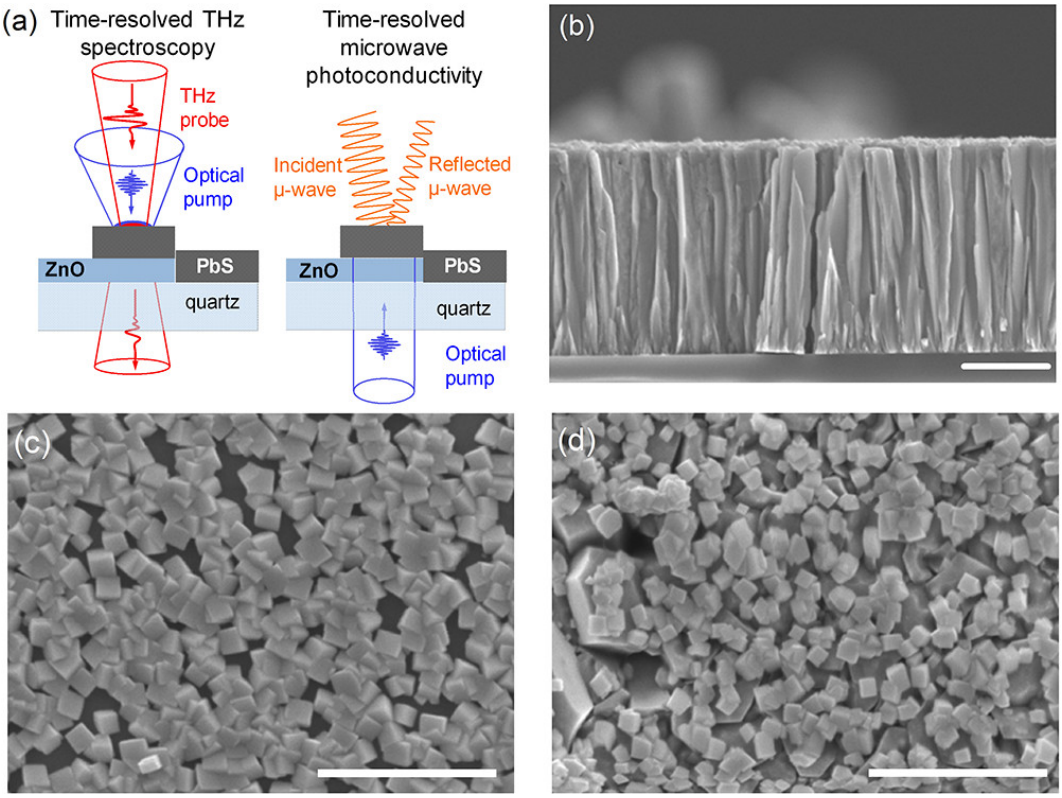

Figure 3.17: (a) Schematic of the sample structure and experimental geometry that allows us to investigate identical PbS layers grown on quartz and on a ZnO film. (b) Cross-sectional SEM image of the ZnO film. (c,d) Top-view SEM images of PbS nanocrystal film on quartz (c) and on the ZnO layer (d). Scale bar in (b), (c), and (d): $1\mu m$.

TRTS and TRMPC

TRTS measurements were used to study transient photoconductivity over the first ~ 200 ps after excitation. Polycrystalline PbS films on quartz and on ZnO were excited by $\sim 100fs$ duration, $800nm$ pulses. With a band gap of 3.5 eV, ZnO is transparent to 1.55 eV (800 nm) pump pulses, and the polycrystalline PbS film was found to absorb $\sim 75\%$ of the incident beam.

For quantifying the photoconductivity over longer, nanosecond-to-millisecond time scales, TRMPS was used [158]. The in-house-fabricated instrument utilized 38 GHz, K_a-band microwave radiation that radiated into free space at the end of a WR28 microwave waveguide, whose face was parallel to the optical bench that contained the instrument. The PbS-on-quartz and PbS-on-ZnO-on-quartz samples were placed on an insulating spacer directly above the waveguide such that the PbS faced the guide while the quartz faced upward toward the pulsed illumination source. A laser diode produced $\sim 10ns$ illumination pulses at 905 nm to photogenerate carriers in the PbS semiconductor as illuminated through the quartz as in Fig.3.17(a). The diode generated $\sim 10^{11}$ photons per pulse that illuminated a $\sim 0.05cm^2$ area as measured at a calibrated photodiode in a reverse-bias circuit (Thorlabs, FDS100-Cal), resulting in a photon flux of $\sim 2 \times 10^{12}$ photons cm^{-2} pulse^{-1} or $\sim 0.4\mu Jcm^{-2}pulse^{-1}$. A pulse rate of 20 Hz afforded sufficient time for all photogenerated carriers to recombine before a subsequent illumination pulse.

The absorptivity of polycrystalline PbS films at 905 nm is comparable to its absorptivity at 800 nm and yields nearly uniform photogeneration of charge carriers throughout the $\sim 150nm$ thick PbS grains. A finline detector with sub-ns responsivity collected the reflected microwave power, where transient changes in the reflected power are proportional to the density of free carriers in the semiconductor conduction band as generated by the diode illumination. Acquisition and digitization of the finline detector signal at a 100 MHz-bandwidth oscilloscope (PicoScope 2208B, Pico Technology, Tyler, Texas) establishes a $\sim 50ns$ time resolution of the microwave instrument. A custom LabVIEW-based program averaged oscilloscope data

for at least 1500 pulse acquisitions for each recorded sample.

3.5.3 Results and Discussion

Part I. Polycrystalline PbS on Quartz: Role of Grain Boundaries

Transient photoconductivity in a polycrystalline PbS film on a quartz substrate over short ($<$ 200 ps) and long ($\sim$ 2 ms) time scales is shown in Fig. 3.18. Early time dynamics were captured for 800 nm excitation fluence ranging from 25 to 255 $\mu J/cm^2$, corresponding to $\sim 10^{14}$ to 10^{15} photons/cm^2. We found that the photoconductivity exhibits biexponential decay with a fast in the picoseconds, and an additional long-lived component that decays sufficiently slowly relative to the 1 ms period between subsequent ultrafast pulses. Quantitatively, the time constant of the fastest decay component, shown in an inset to Fig. 3.18 (a), increases from $\sim$7 to $\sim$12 ps as the excitation fluence increases to 128 $\mu J/cm^2$, and remains $\sim$12 ps for higher fluences. After $\sim$100 ps, the photoconductivity in Fig. 3.18 (a) is nearly the same, regardless of excitation fluence and, correspondingly, regardless of photoinjected carrier density. With a significantly slower pulse repetition rate (20 Hz vs 1 kHz) and much lower pulse fluence (0.4 vs $\geq$ 25 $\mu J/cm^2$), the microwave experiment demonstrates that the lifetime of the photoexcited carriers is on the order of 1 ms Fig. 3.18 (b). The fluence dependence of the fast, 7–12 ps component of the transient photoconductivity dynamics suggests the presence of multiple trapping and recombination channels for photoexcited carriers, some of which exhibit saturation under increasing excitation. Our observation of a very long, $> 100\mu s$, lifetime of photoconductivity as revealed in Fig. 3.18 (b) is consistent with previous reports of electron traps that exist in PbS grains, which rapidly trap photoexcited electrons and leave holes free to conduct [159].

Insights into the mechanisms that govern photoexcited carrier dynamics can be gained by examining the time-evolution of frequency-resolved complex conductivity following photoexcitation with varying fluence (Fig. 3.19). Comparing the transient THz photoconductivity spectra of the polycrystalline PbS at different time delays after excitation with 25 and 255

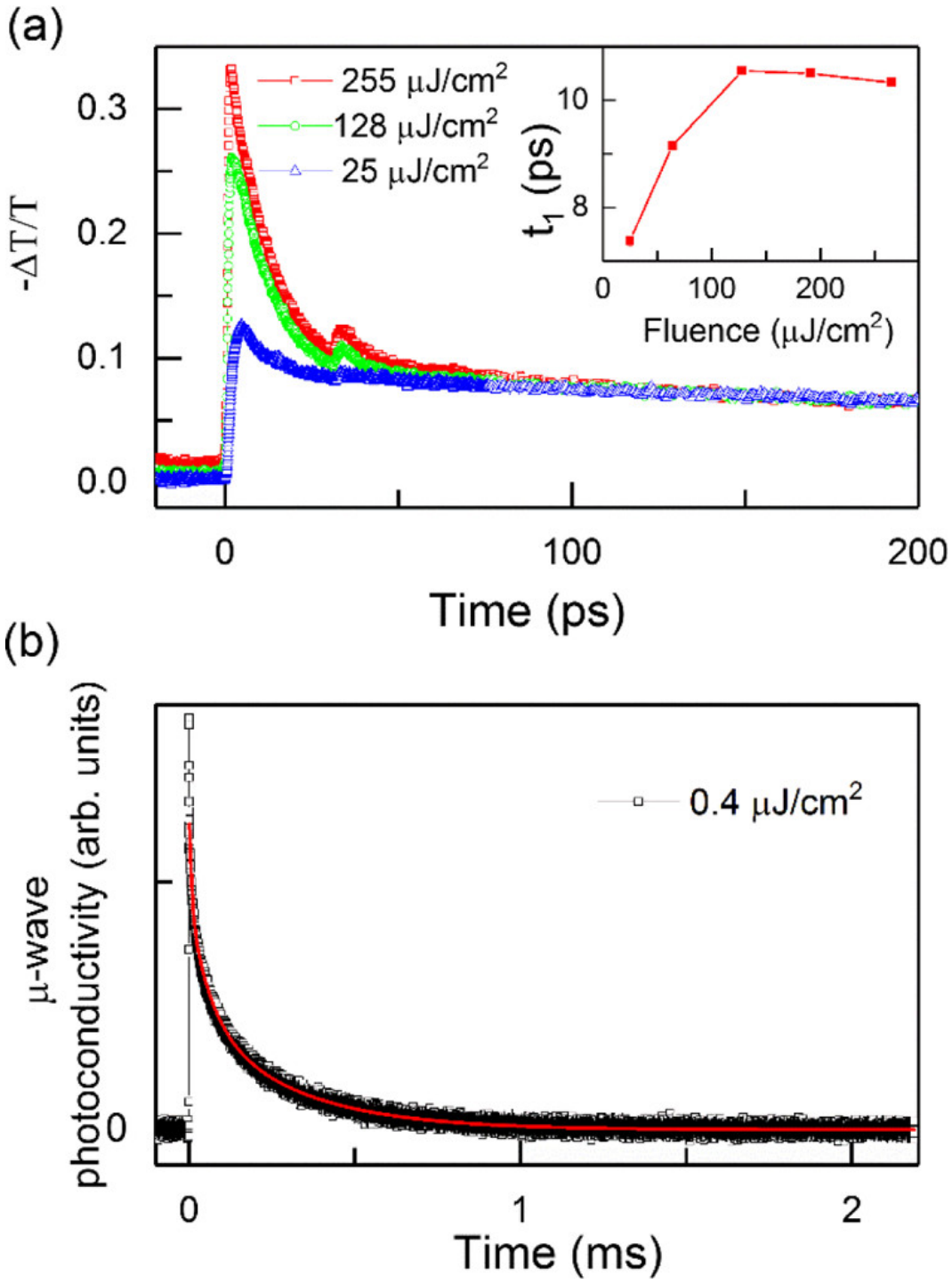

Figure 3.18: Time-resolved photoconductivity of PbS nanocrystalline films. (a) Picosecond dynamics of photoconductivity following photoexcitation with 800 nm, $\sim$ 100 fs pulses of varying fluence. Inset: fast decay time as a function of excitation fluence. (b) Nanosecond-to-millisecond photoconductivity dynamics following photoexcitation with 908 nm, $\sim$ 10 ns pulses.

$\mu J/cm^2$ fluence of the 800 nm pump, we observed a pronounced difference in the photoconductivity spectra for different fluence values at early times (5 ps) after photoexcitation. However, by 100 ps the spectra are indistinguishable, despite the order-of-magnitude difference in excitation fluence. Furthermore, as expected in a polycrystalline film, photoconductivity at all fluences and time delays exhibits strong suppression of real conductivity at low frequencies and negative imaginary conductivity in the experimental frequency range. We analyzed the spectra using the Drude–Smith model, Eq. 2.42.

Drude–Smith fitting parameters (N, c, and τ_{DS}) at different times after excitation as a function of excitation fluence are plotted in Fig. 3.19.

The density of photoexcited carriers at 5 ps after excitation ranges from $\sim 2 \times 10^{17}$ to $\sim 5 \times 10^{17}$ cm^{-3} depending on excitation fluence, which is nearly two orders of magnitude lower than the photoinjected carrier density that would be expected if each absorbed photon resulted in an electron-hole pair. This indicated that most of the carriers become trapped or recombine non-radiatively over the timescales that are shorter than our experimental resolution of ∼300 fs. After that, most photoexcited electrons are trapped, and the remaining holes exhibit long lifetimes, as discussed earlier. The c-parameter that is close to -1 in most spectra, with an exception of early times after excitation with high fluence, shows that most photoexcited carriers are localization within the individual grains. The early time (5 ps) c-parameter that reaches -0.9, and the corresponding non-zero long-range conductivity σ_{DC} at higher excitation fluences shows that some carriers can travel across intergrain boundaries.

This transient occurrence of long-range transport correlates with high ($> 3 \times 10^{17}$ cm^{-3}) carrier density and can be explained by a previously proposed model of PbS grains and grain boundaries [159] Fig. 3.19 (d). Positively charged defects at the boundaries result in an ∼80 meV energy barrier for holes, across which holes can travel by thermally activated transport or tunneling. At high excitation fluence, large initial carrier density increases the probability of electrons becoming trapped at the grain boundary defects, temporarily reducing the energy barrier for hole transport and resulting in increased long-range conductivity. As the boundary

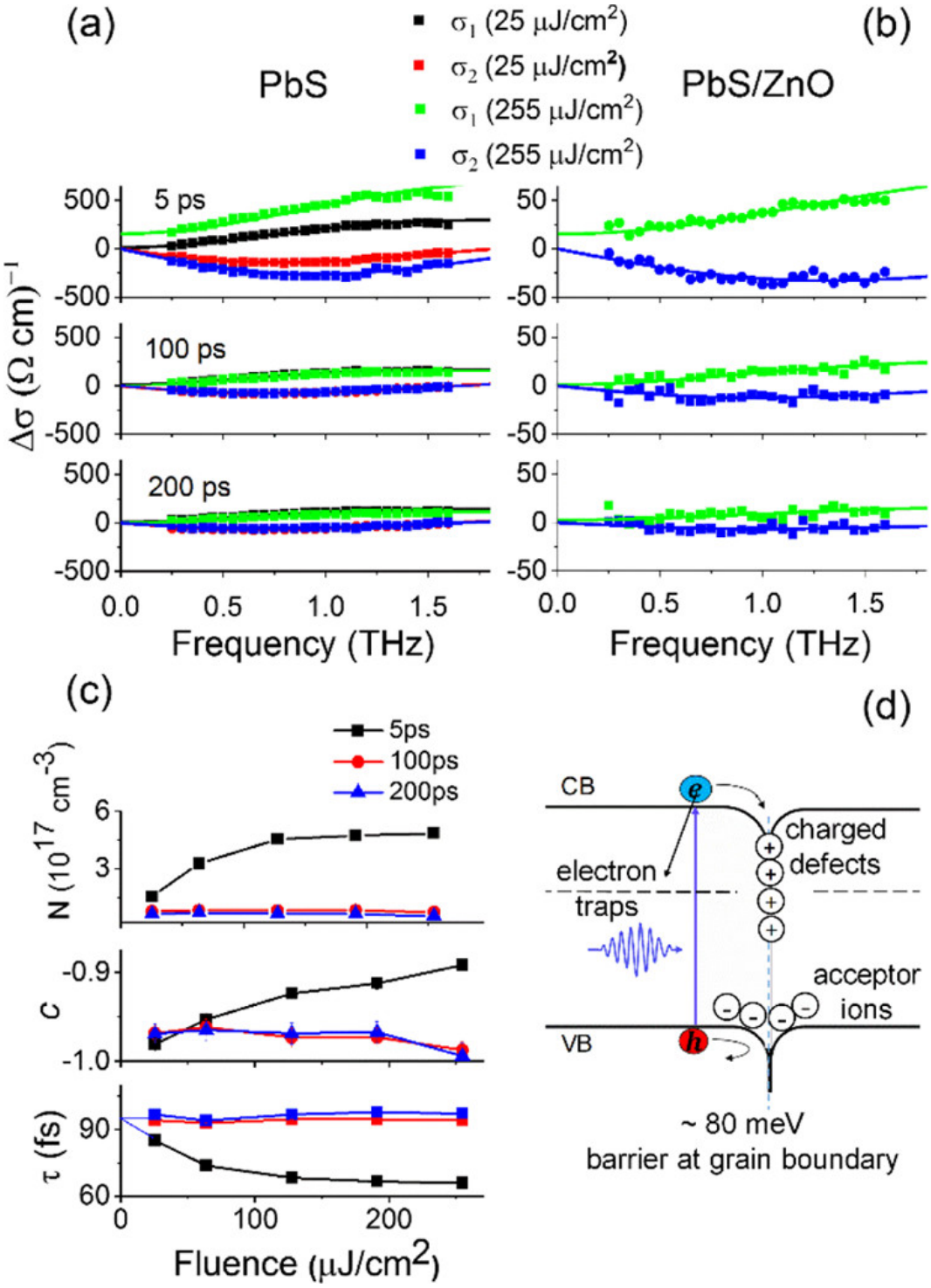

Figure 3.19: (a) Real (black and green) and imaginary (red and blue) photoconductivity for two different values of pump fluence in PbS on quartz; (b) real (green) and imaginary (blue) photoconductivity for high pump fluence in PbS on ZnO. The lines in (a,b) represent a global fit of real and imaginary components of the conductivity for each fluence and time delay value to the Drude–Smith model Eq. 2.42. (c) Drude–Smith fitting parameters as a function of the excitation fluence for different times after excitation. Dotted blue lines in the graph of τ_{DS} as a function of fluence show extrapolation of the scattering time to zero fluence. (d) Schematic energy level diagram at the interface between two PbS grains.

defect states are filled by ∼8-10 ps, the barriers are restored. Slowing of the fast (8 - 10 ps) decay components at higher excitation fluence suggests transient saturation of the electron traps in the PbS grains, which leaves more electrons to be trapped at grain boundaries and lower intergrain barriers for mobile holes. Transient conductivity at times >100 ps after excitation varies slowly and is independent of initial injected carrier density. When the density of free carriers falls to $\sim 0.8 \times 10^{17}$ cm^{-3}, the system reaches quasi-equilibrium, which persists for hundreds of microseconds. This carrier density corresponds to ∼300 carriers (holes) per PbS crystallite of 150 nm size, which can be used as an estimate of the electron trap density in the PbS grains. Slow decay of photoconductivity over hundreds of picoseconds and slower timescales then proceeds by recombination of trapped electrons and mobile holes.

High carrier density at early times after excitation, particularly with high optical fluences, also manifests in reduced τ_{DS} as carrier–carrier scattering contributes to scattering time as described by $\frac{1}{\tau_{DS}} = \frac{1}{\tau_{int}} + \frac{1}{\tau_{boundary}} + \frac{1}{\tau_{carrier-carrier}}$. Extrapolating τ_{DS} to zero fluence, as shown in the bottom graph of Fig. 3.19 (c), yields the lower limit to $\tau_{DS} = 97 \pm 10$ fs in the absence of carrier-carrier scattering. Using the average grain size of 150 nm and carrier thermal velocity of 107 cm/s to estimate contribution of grain boundary scattering, we find that the intrinsic mobility of carriers is $\approx 750 cm^2/Vs$, comparable to that in single crystalline PbS [160]. At the same time, long-range mobility is negligibly small at $\mu_{long-range} = \mu_{int}(1 + c)$ because of the grain boundaries.

Concluding, we found that room temperature chemical bath deposition results in polycrystalline PbS films that consist of cubic crystallites with high optical absorption and large $\sim 750 cm^2/Vs$ intrinsic carrier mobility but suppressed long-range, intergrain transport. Intergrain mobility can be transiently increased by photoexciting the film using high, $> 100 \mu J/cm^2$ fluence. However, the question remains: can photoexcited electrons be efficiently extracted from PbS crystallites into a wide band gap, conductive material like ZnO?

Part II. Polycrystalline PbS on ZnO: Role of the PbS/ZnO Interface

Earlier studies using transient optical absorption, time-resolved photoluminescence, and time-resolved surface photovoltage spectroscopy have demonstrated rapid decay of photoexctited carrier density over sub-picosecond timescales in PbS nanocrystals in the presence of ZnO owing to the band alignment that favors injection electrons from PbS quantum dots into ZnO. In the case of bulk-like PbS, Fermi level equilibration may either in injecting result in a noninjecting (1) or an injecting (2) junction, as illustrated schematically in Fig. 3.20 (a). In both cases, electrons in the conduction band of PbS can get trapped in interface defect states. Even in the case of injecting junction (2), interface trapping may be sufficiently rapid to prevent appreciable injection of mobile electrons into ZnO. The electrons trapped at PbS/ZnO interfaces are then expected to attract mobile holes and result in their rapid recombination. Here, we have leveraged the unique sensitivity of TRTS to free carriers to comparing transient THz photoconductivity of the polycrystalline PbS film on ZnO and on quartz in order to investigate whether the injection of free, conductive electrons into ZnO occurs following photoexcitation.

Both microsecond and ultrafast carrier dynamics reveal further insights into the recombination processes. The intensity-normalized TRMPS decays in Fig. 3.20 (b) demonstrate significantly shorter free carrier lifetimes for PbS on ZnO (blue symbols) as compared to PbS on quartz (red symbols). Fig. 3.20 (c) shows the THz photoconductivity decay dynamics in polycrystalline PbS film on quartz (red) and on ZnO (blue), with absolute values of $-\Delta T/T$ on the left, and normalized $-\Delta T$ on the right. The presence of ZnO decreases the peak photoconductivity by over an order of magnitude at all fluence values and speeds up carrier trapping. The small residual photoconductivity in the PbS/ZnO system after the first few picoseconds is due to the photocarriers in a small fraction of the PbS grains that are not in contact with ZnO, as can be seen from transient frequency-resolved THz conductivity spectra (Fig. 3.19 (b)). The complex conductivity in PbS/ZnO system is qualitatively the same as in polycrystalline PbS on quartz (Fig. 3.19 (a)), with fully suppressed long-range transport

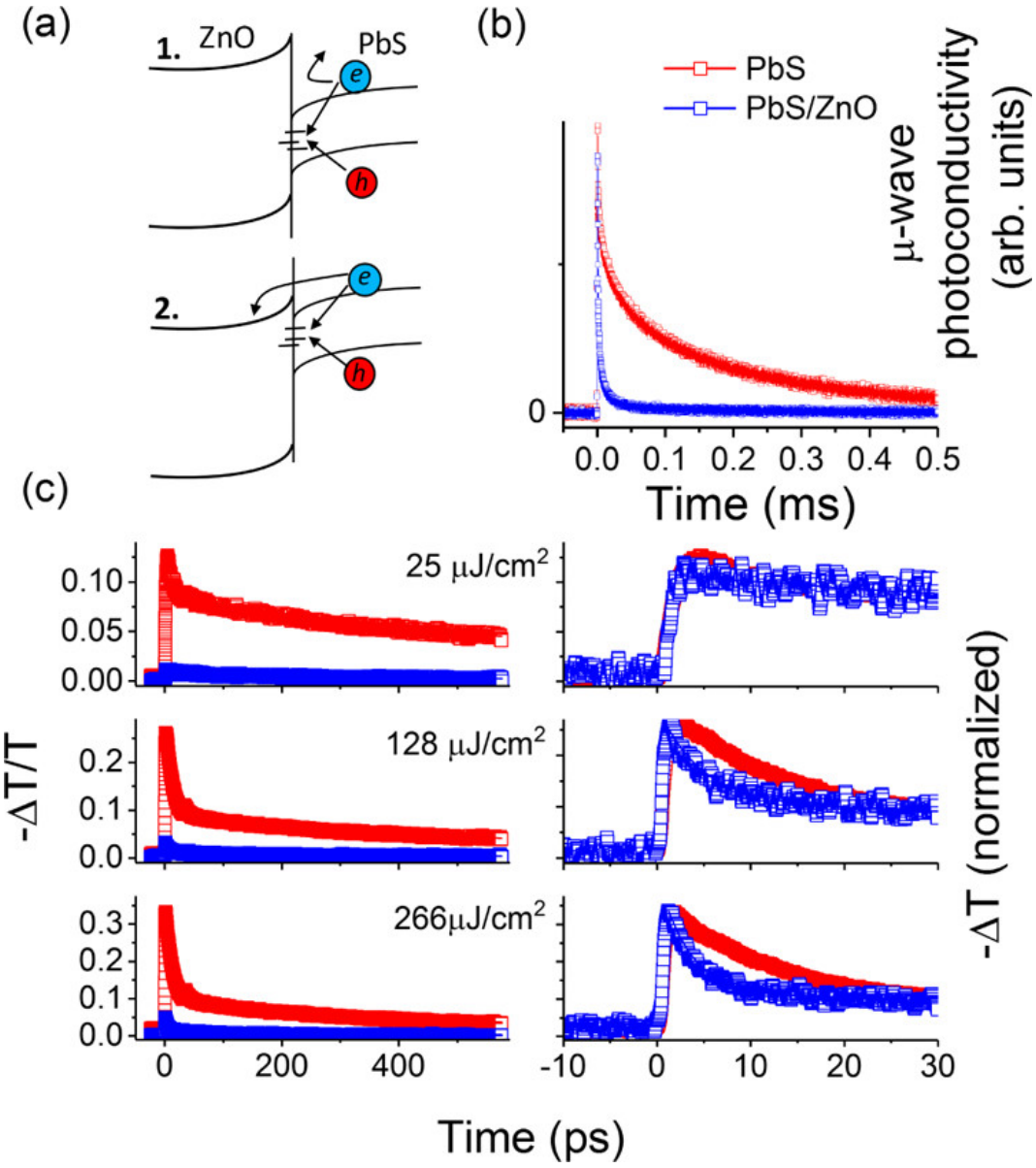

Figure 3.20: (a) Band diagram at PbS/ZnO interface (after Sun et al.[161] and Ehrler et al.[162]). (b) Normalized change in microwave conductivity for PbS-on-quartz (red symbols) and PbS-on-ZnO (blue symbols) samples for 0.5 ms following a 10 ns illumination pulse at 905 nm. (c) Left: time-resolved THz photoconductivity of PbS polycrystalline film on quartz (red) and PbS film on top of ZnO layer (blue) of 800 nm 100 fs pump pulse measured for different fluences. Normalized decays are shown on the right.

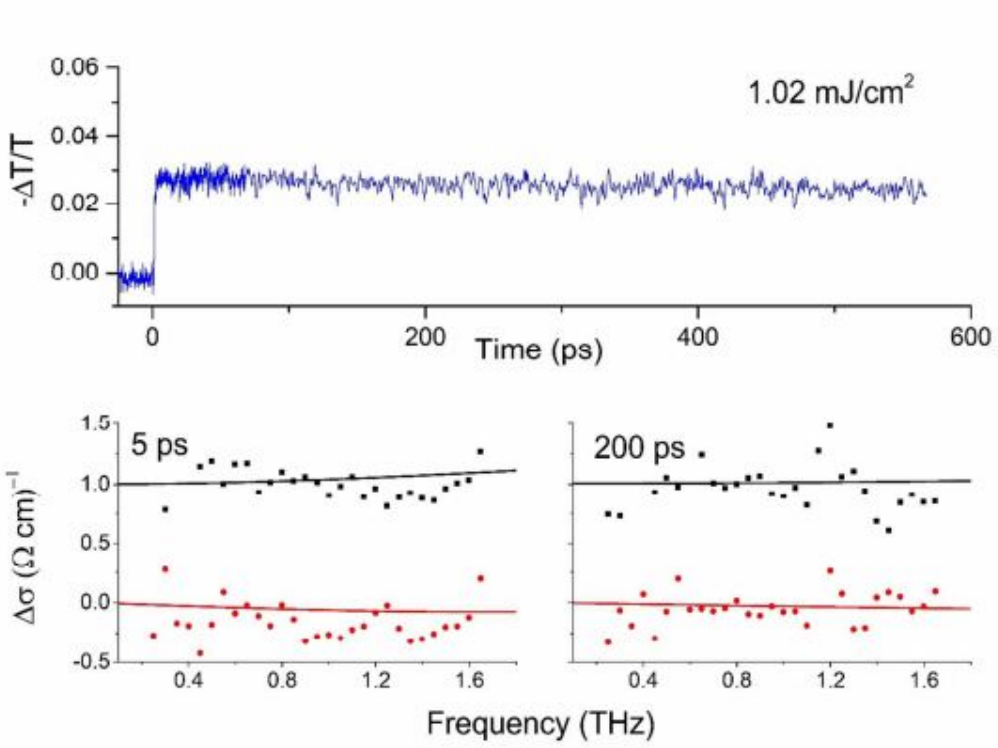

Figure 3.21: Transient photoconductivity in ZnO film.

at times $\geq$ 100 ps and small nonzero $\sigma(\omega = 0)$ at 5 ps, and differs only by the magnitude that is 10 times smaller because of the lower carrier density. Specifically, we do not observe injection of mobile carriers into the ZnO layer, which would result in significant long-range conductivity at longer times, as shown in the Fig. 3.21 where ZnO photoexcited with a 400 nm pulse.

While the band gap of bulk ZnO is 3.3 eV, photoexcitation of the ZnO film grown on a quartz substrate with a high fluence ($\sim 1 mJ/cm^2$) 400 nm (3.1 eV) pulses does result in a small but measurable photoconductivity due to absorption by the band tail states. Resulting lifetime of photoexcited carriers is very long, as no appreciable photoconductivity decay is observes in 550 ps after photoexcitation, and photoconductivity spectra at 5 ps and 200 ps yield a very short, $\sim$ 20 fs scattering time and c-parameter of -0.6 due to the presence of defects and grain boundaries in solution-deposited ZnO. Both the scattering time and localization parameter for carriers in ZnO differ significantly from the photoconductivity observed

in PbS/ZnO system, confirming the photoexcited electrons are trapped at the interface between PbS and ZnO rather than injected into ZnO and that this occurs over scales below our time resolution of ∼300 fs. As a result, highly mobile photoexcited holes are attracted to the PbS/ZnO interface, where they recombine with trapped electrons.

3.5.4 Conclusion

In summary, TRTS and TRMPC measurements of polycrystalline PbS films deposited on ZnO and on insulating quartz showed evidence of long-lived (∼ ms) photoexcited holes with high, $\sim 750 cm^2/Vs$ intrinsic mobility within individual crystallites but suppressed long-range, intergrain transport. We also found that PbS/ZnO interface states facilitate rapid trapping and recombination of carriers photoexcited in PbS, reducing the lifetime of mobile carriers by over an order of magnitude compared with the PbS film on quartz. We do not observe injection of mobile carriers into the ZnO layer over timescales of hundreds of picoseconds. Instead, the only mobile carriers in both systems are found within PbS crystallites, characterized by strong localization by PbS grain boundaries and intrinsic mobility of $\sim 750 cm^2/Vs$. This observation underscores the need for chemical passivation of PbS/ZnO interfaces to achieve efficient injection of photoexcited carriers into ZnO for application of room temperature CBD-grown polycrystalline PbS on ZnO in photovoltaics and photodetectors. Increase of efficiency of electron injection from PbS quantum dots into ZnO has been demonstrated using inorganic buffer layers [163], organic ligands [164], or self-assembled monolayers [165]. Future work is needed to establish whether similar approaches of using buffer layers to minimize interfacial recombination and enable transfer of photoexcited electrons from PbS into ZnO electrodes are also applicable to small band gap, polycrystalline PbS.

Chapter 4

Ultrafast Photocurrents in Group-IV Chalcogenides

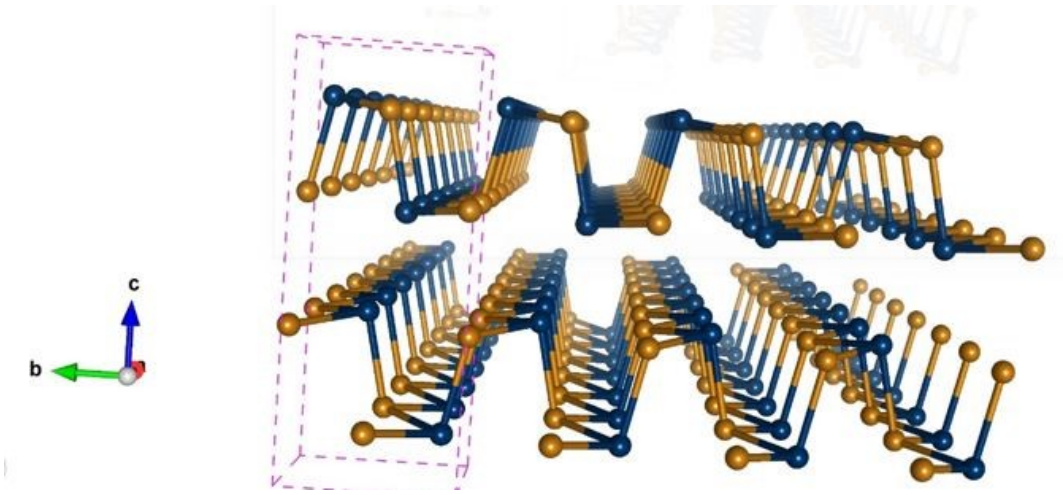

4.1 Ultrafast Zero-Bias Photocurrent in GeS and GeSe

Shift current is the prevailing mechanism behind bulk photovoltaic effect (BPVE), as excitation of an electron from the valence to the conduction band results in a spatial shift of the electron charge density on the order of a lattice constant and subsequent ballistic quantum coherent carrier transport [77, 166]. The possibility of a zero-bias photocurrent without the need for a p-n junction makes materials that exhibit strong BPVE attractive candidates for new types of solar cells with efficiencies not constrained by the Shockley-Queisser limit [167]. Hot shift current carriers can rapidly travel to electrodes where they can be collected, provided that required travel distance is comparable to their mean free path, which is estimated to be on the order of 10–100 nm. Large second-order electric susceptibilities responsible for nonlinear optical effects such as optical second harmonic generation, optical rectification and shift current [130] are particularly pronounced in ferroelectric materials. Lattice distortion that is responsible for a nonzero intrinsic, spontaneous polarization also results in a broken inversion symmetry [168]. As a result, ferroelectrics can exhibit shift current response to unpolarized excitation light, unlike nonpolar noncentrosymmetric materials that can generate shift currents only when excitation is linearly polarized [168, 169].

Recent theoretical investigation predict that monolayer 2D group-VI monochalcogenides are multiferroic and capable of generating significant shift currents [78, 102, 138, 170]. In-

plane electric polarization results from an elastic distortion of the lattice (Fig. 4.1a), as the top and the bottom atoms shift in the armchair direction [78, 100]. This breaks the inversion symmetry of the monolayer, and can enable second order nonlinear optical effects such as OR, a non-resonant effect, and a shift current, a resonant effect that is expected to dominate for above the band gap photoexcitation conditions [78]. Optical excitation results in an instantaneous spatial shift of electron density distribution along the S–Ge or Se-Ge bond, as shown in the Fig. 4.1 [78]. Using ab initio tight binding calculation within a two-band model, Cook et al. predicted that the shift current in monolayer GeS and GeSe is peaked for excitation energy directly above the bandgap [78]. Here we present experimental observation of ultrafast shift in group-IV monochalcogenides GeS and GeSe currents by detecting THz emission from these materials in response to above bandgap photoexcitation (Fig. 4.1). TES (Chapter 2.5) has also been previously applied to detect shift currents in GaAs, CdS, CdSe, Bi_2Se_3, and other materials. Shift current in response to excitation with ultrafast pulses gives rise to THz emission that varies as $\vec{E}_{shift} \propto \vec{J}_{shift}$ immediately above the surface of the photoexcited material [98] (Chapter 2.5.3).

As the samples we have studied are not monolayers but rather multilayer, bulk crystals, we attribute THz generation due to the shift current response in the surface layer. While the stacking sequence of the layers in this van der Waals material yields a centrosymmetric bulk structure that corresponds to the D_{2h} (mmm) point group (Fig. 4.1 a), inversion symmetry is broken at the surface, and a spontaneous surface polarization can exist in the armchair direction just as it does in a monolayer [171]. Excitation fluence, orientation, and excitation polarization dependence of the THz emission confirms that shift currents flow along the direction of surface layer spontaneous polarization.

Pronounced nonlinear optical effects in the visible range that can be tuned by strain and external fields made monolayer of group-IV monochalcogenides a promising platform for a variety of applications in lasers, electro-optic modulators, switches, and frequency conversion devices.

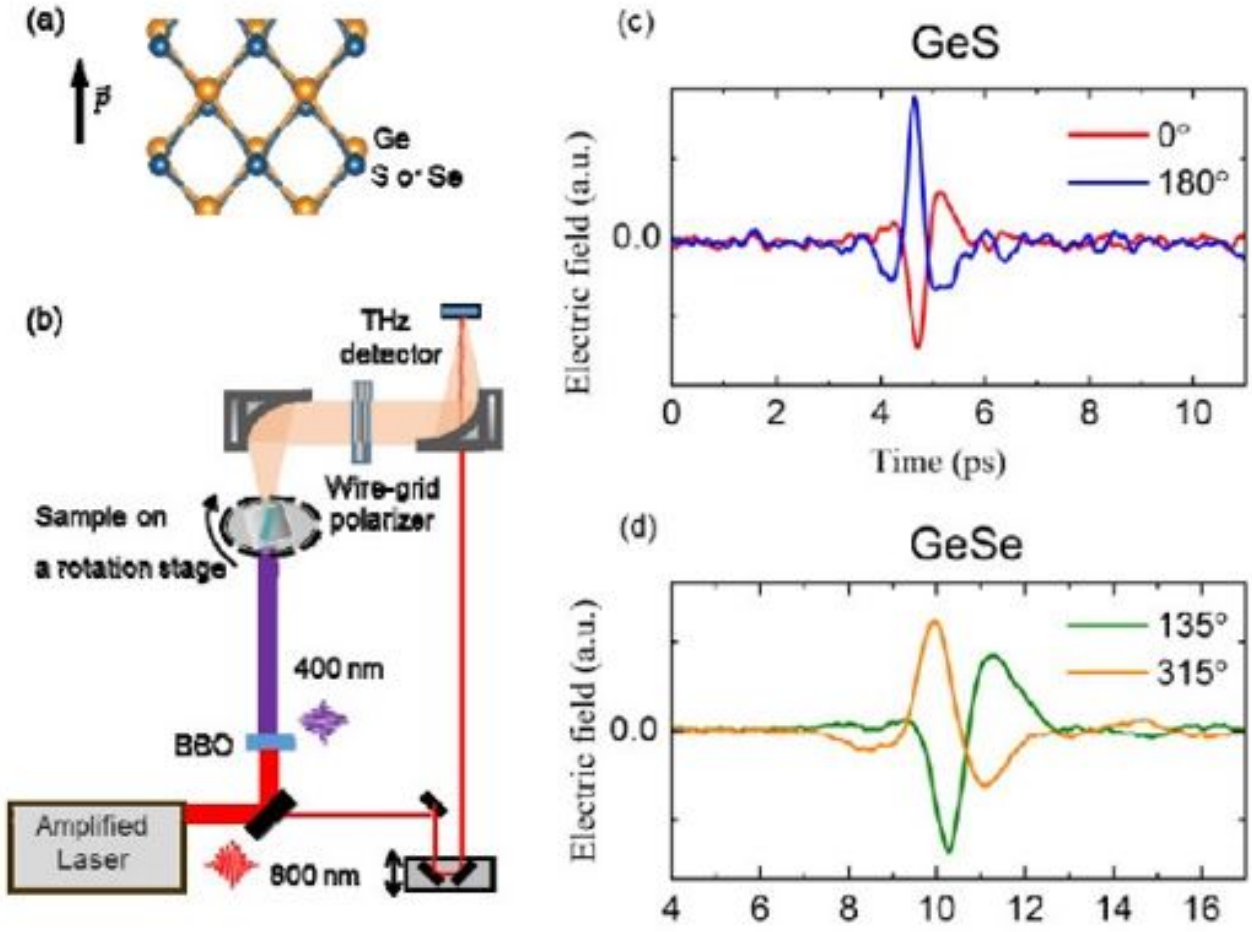

Figure 4.1: (a) A spontaneous electric polarization vector along the armchair direction in the surface layer of GeS or GeSe. b) TES experiment. THz waveforms taken at different sample orientations, indicating that rotating sample by 180^o reverses polarity of the emitted pulse in (c) GeS ($15\mu J/cm^2$ excitation) and (d) GeSe ($190\mu J/cm^2$ excitation)

4.1.1 Experimental methods

GeS nanosheets (space group: $Pnma$) are synthesized through the vapor-liquid-solid method using established procedures as illustrated in Fig. 3.13(a). Their multilayer thickness and large lateral dimensions makes these structures essentially bulk-like in the context of the phenomena discussed here. GeSe single crystals were synthesized using a chemical vapor transport growth technique using high purity Ge and Se pieces. A more detailed description of this growth can be found in the previous chapter (Chapter 3) and in the Refs [33, 34].

We have used TES to explore generation of THz radiation in multi-layer GeS and GeSe crystals in response to the above band gap excitation with ultrashort laser pulses. For the measurements, samples were excited at normal incidence with 400 nm or 800 nm, 100 fs laser pulses as illustrated schematically in Fig. 4.1. A pair of off-axis parabolic mirrors focused the emitted THz pulses onto a [110] $ZnTe$ crystal where they were coherently detected by free-space electro-optic sampling. The wire-grid polarizer ensured that only a vertically polarized component of the generated THz pulses was detected. Sample orientation was varied by rotation of a sample stage through an angle Θ_{sample}, and the direction of the linear polarization of the optical pump pulse relative to the THz detection was varied by using a half-wave plate (not shown). As discussed in the last section of Chapter 2, normal incidence geometry precludes us from detecting photocurrents due to the photo-Dember effect, built-in fields, or photon drag. Single color, linearly polarized excitation precludes injection current. Thus, emission in response to above band gap, linearly polarized excitation in the absence of external electrical bias suggest that its origin is shift current. Data shown in Fig. 4.1 (c) and (d) have been taken with the pump polarization unchanged and parallel to the THz detection. Rotating the sample by 180^o reverses the polarity of emission for both GeS and GeSe while the temporal shape of the waveform shows only minimal change. This demonstrates that the emission polarity is dictated by the symmetry breaking due to the intrinsic ferroelectric polarization and supports the surface shift current as a mechanism of THz generation in bulk GeS and GeSe.

4.1.2 Results and discussion

THz emission from GeS and GeSe can be analyzed using a model proposed by Braun et al. [98]. Within its framework, photoexcitation results in an instantaneous charge displacement $x_0 H(t)$, where x_0 is a spatial shift of electron density along the $S(Se) - Ge$ bond predicted to be $\sim 0.52\mathring{A}$ [78] and $H(t)$ is a unit step function. Transient shift current is then given by the convolution of the temporal derivative of this charge displacement with the pump intensity envelope $I_p(t)$: $J_{sh} \propto \frac{\partial}{\partial t}[H(t)e^{-t/\tau sh}]^* I_p$, where τsh is a phenomenological decay time that accounts for hot carrier relaxation.

Analysis of the excitation power and polarization dependence of the shift current provide further information beyond the dynamics. Amplitude of the shift current that is responsible for BPVE is expected to be linear in incident intensity and can be expressed as

$$J_a = \frac{c\epsilon_0}{2}\kappa^{abb} E_b(\omega) E_b(-\omega) \tag{4.1}$$

where J_a is current in the a direction, $E_b(\omega)$ is the electric field of the optical excitation at frequency ω polarized in the b direction, κ^{abb} is a photoresponsivity tensor, c the speed of light, and ϵ_0 the permittivity of free space. In GeS and GeSe, shift current flows in the plane of the sheet in the direction of displacement x, or in our case armchair direction (e.g, $J_a = J_x$), resulting in a strongly polarized THz emission. Given a significant structural anisotropy of the crystal lattice structure between the armchair and zigzag direction, the observed independence of the shift current on pump polarization is unexpected. Theory predicts that κ^{xxx} is large for above-gap excitation, while κ^{xyy} is near zero [78].

To confirm this hypothesis and demonstrate that the shift current magnitude direction and the corresponding amplitude and polarity of the emitted THz pulses are dictated primarily by the intrinsic polarization, we have explored how rotating the samples while maintaining an unchanged pump polarization affects the resulting THz transient seen at the detector. In both cases the peak of THz emission polarization has a cosine dependence on the angle that

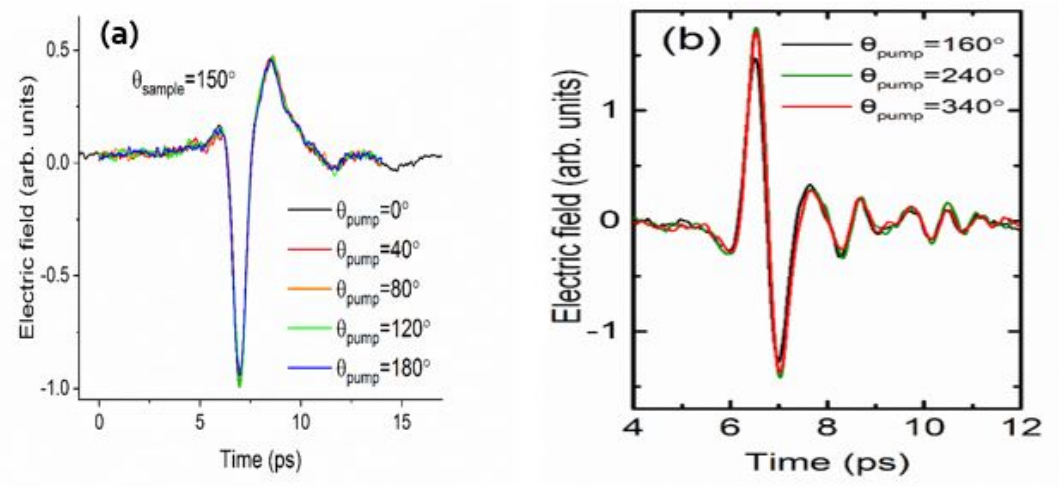

Figure 4.2: Selected THz waveforms excited by 400 nm pulses with different pump polarizations, (a) bulk GeSe and (b) GeS nanosheets.

the sample makes with respect to the detection direction. Overall emission is strongest when the sample is aligned along the detection direction. For any two waveforms taken with the sample rotated by 180^o, the polarity of the emission reverses while the amplitude shows only minimal change, as shown in Fig. 4.1 (c) and (d).

Since the band gaps for GeS nanosheets and bulk GeSe are $E_g \sim 1.6eV$ and $\sim 1.2eV$ respectively, THz emission in GeS is not observed after photoexcitation with 800 nm. However, in the case of GeSe, we observe THz generation after excitation with both 400 and 800 nm. Shift current resulting from excitation with ultrafast pulses gives rise to THz emission that varies as $\vec{E}_{shift} \propto \vec{J}_{shift}$ immediately above the surface, and again, reimaged onto the $ZnTe$ detector crystal with the help of the parabolic mirrors.

By varying the excitation pulse polarization while keeping the sample orientation unchanged relative to THz detection direction ($\Theta_{sample} = 0^o$) for both samples we found that the amplitude, shape and polarity of the emitted THz waveforms are insensitive to the linear polarization of the pump pulse (Fig. 4.2). This is in agreement with our prediction and indicates that shift current is dictated by the intrinsic polarization and symmetry breaking in the surface layer. While the GeS sample contains an array of nanosheets with different orientations, emissions by different nanosheets do not fully cancel out due to accidental preferential

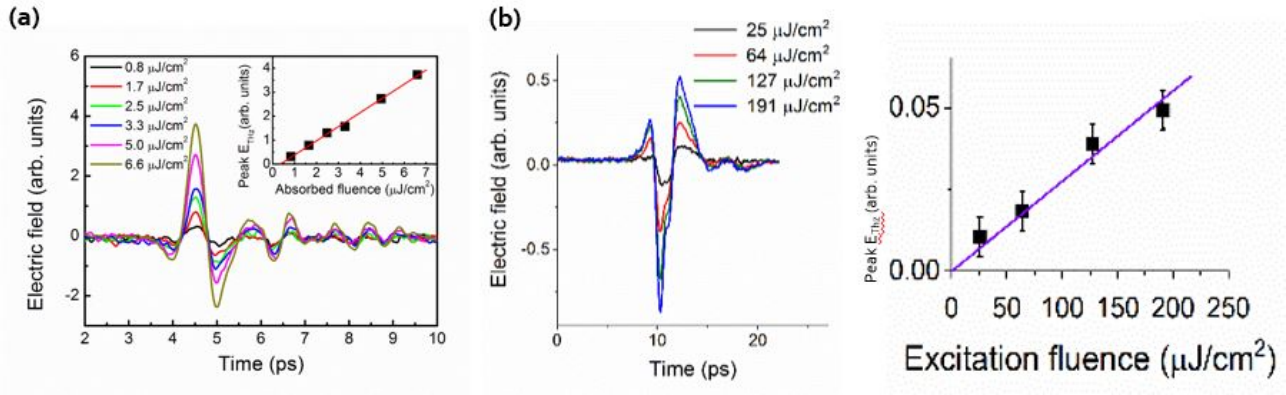

Figure 4.3: Excitation fluence dependence of THz generation in (a) GeS and (b) GeSe. Inset: Peak electric field as a function of absorbed fluence; red line, linear fit.

orientation of sheets within the 1.5 mm observation spot.

We have also studied the fluence dependence of THz emission from GeS and GeSe. From Eq. 4.1, we expect shift current to depend linearly on excitation fluence. Fig. 4.3 shows that the electric field of THz pulses emitted by both GeS and bulk GeSe is linearly dependent on absorbed fluence of 400 nm pulses, while the shape of THz waveforms is unchanged. The THz pulse peak value is shown in the inset, and the red line is a line fit to experimental data (black squares). Linear fluence dependence of the emitted THz pulse electric field, and therefore of transient current in the sample, is consistent with the shift current being the mechanism behind the observed effect.

Additional information can be gleaned from analyzing the bandwidth of the emitted THz pulses. As shown in the Fig. 4.4 (c), the detection bandwidth of a $ZnTe$ detector crystal is limited to $\sim$ 0.2 - 2.5 THz, and it acts as a band-pass filter, removing all frequencies outside the range. Modeling the shift current in GeS as was shown earlier [98], we predict the emission in response to the pump pulse of 100 fs duration extends to 10 THz. The observed bandwidth is limited by the detector crystal. However, in the case of GeSe crystal, GeSe emits nearly single-cycle THz pulses in response to both 800 nm (1.55 eV) or 400 nm (3.10 eV) excitation (Fig. 4.5) as both excitation energies are larger than $\sim$ 1.2 eV band gap. For both excitation energies, the observed bandwidth of THz emission is limited to $\sim$ 1 THz. The sample itself is a limiting factor in uncovering the true ultrafast transient behavior of the surface shift

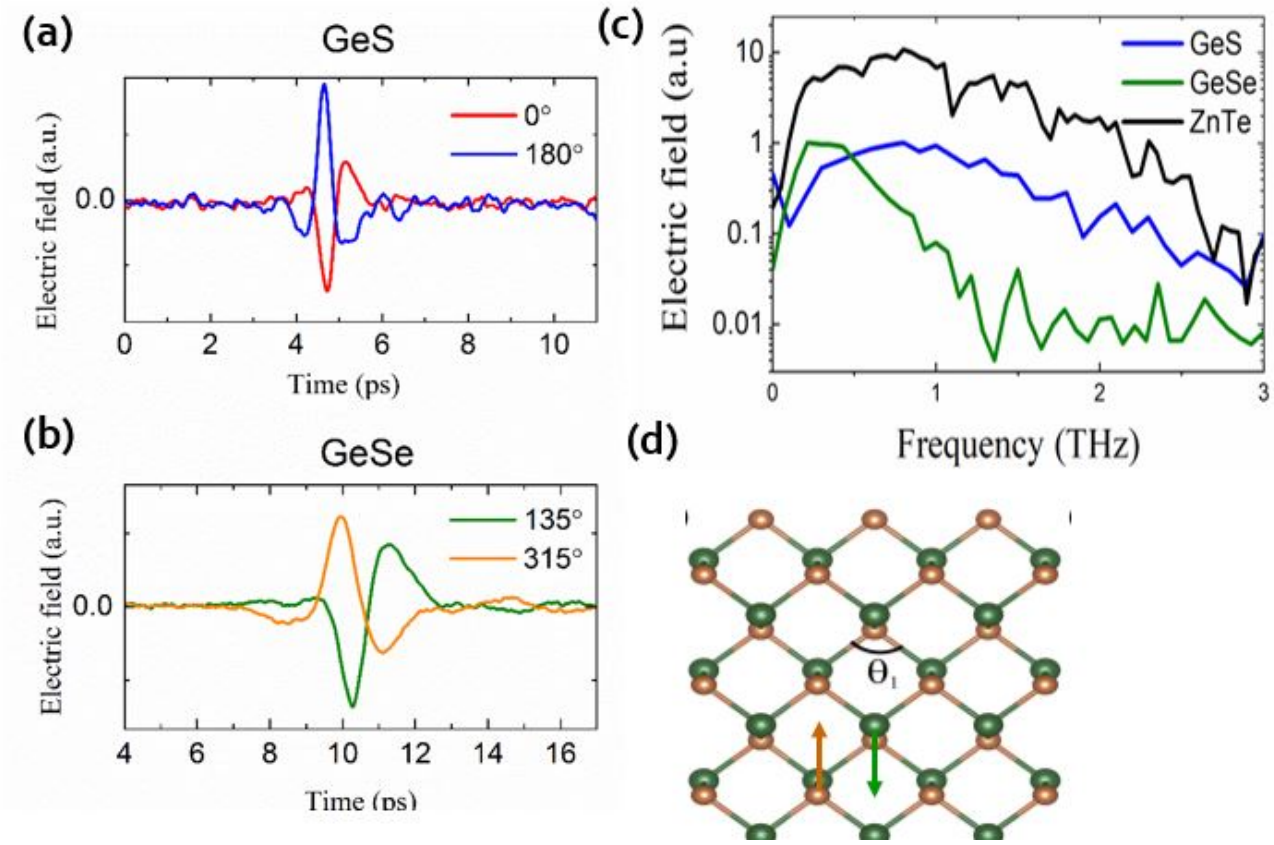

Figure 4.4: THz waveforms generated by photoexciting (a) GeS nanosheet and (b) GeSe crystal (c) the corresponding amplitude spectra for GeS (blue), GeSe (green) and ZnTe (black) (d) depicted B_{3u} phonon ($\sim$ 2.56 THz) for GeSe crystal.

currents from the THz pulses detected in the transmission geometry. GeSe crystal absorbed over 80% of incident THz radiation that was generated in a 1 mm thick [110] $ZnTe$ crystal, with absorbance increasing nearly five-fold between 0.2 to 1.8 THz. Strong THz absorption can be attributed to low frequency B_{3u} and B_{1u} infrared active phonons centered in the 2.5-2.6 THz range. B_{3u} phonons in particular are associated with opposite motion of Ge and Se along the armchair direction and couple strongly to the THz radiation polarized along this direction. As a result, GeSe crystal itself acts as a low pass filter, attenuating THz pulses emitted by the surface layer and broadening them to 1-2 ps in duration, as shown in the Fig. 4.5 (b).

We also observe that the magnitude of the detected THz pulses is significantly lower for 800 nm excitation compared to 400 nm excitation. This observation also supports the surface

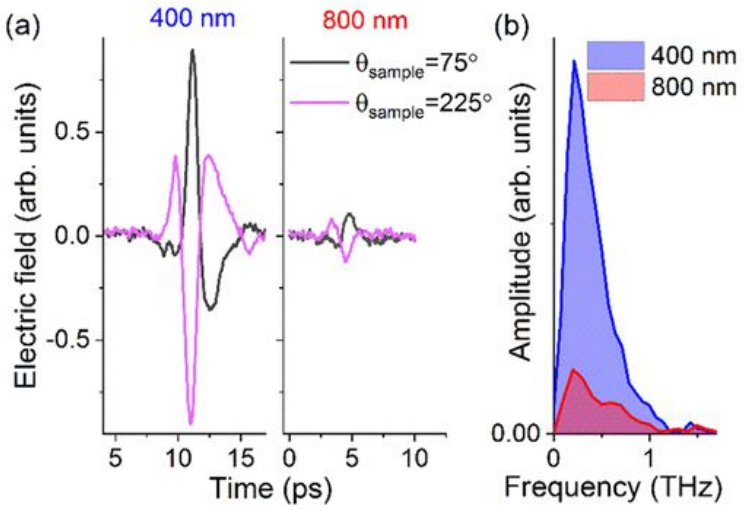

Figure 4.5: (a) THz waveforms emitted by the GeSe crystal as a result of excitation either with $\sim 190\mu J/cm^2$, 100 fs, 400 nm pulses (left panel) or with $\sim 130\mu J/cm^2$, 100 fs, 800 nm pulses (right panel), with $\Theta_{pump} = 0^o$ in both cases. Rotating the crystal by 180^o reverses polarity of the emitted pulse. (b) Amplitude spectra of the THz waveforms excited with 400 nm and 800 nm pulses taken with $\Theta_{sample} = 75^o$.

origin of the observed THz emission. Assuming that the shift current in the top surface layer of a GeSe bulk crystal is qualitatively similar to that in a monolayer, shift current magnitude is expected to peak strongly immediately above the band gap and then fall off at higher energies [102]. As the optical penetration length of both 400 nm and 800 nm is significantly shorter than the thickness of the crystal, the bottom surface does not contribute. We find that the spectrally integrated amplitude of the THz waveforms emitted following excitation with 800 nm (1.55 eV) is nearly 20% of that for 400 nm excitation (3.10 eV) (Fig. 4.5 (b)). Taking into account a $\sim$ 30% difference in excitation fluence, 400 nm pulses result in $\sim$ 3.5 times stronger emission for equivalent incident excitation fluence. However, the absorption coefficient is $\sim$ 10-fold higher at 400 nm compared to 800 nm ($\sim 0.078nm^{-1}$ vs $\sim 0.009nm^{-1}$ at 800 nm). Taking into account reflection losses ($\sim$ 47% for 400 nm and $\sim$ 41% for 800 nm), and using 0.25 nm as the thickness of a GeSe monolayer, we calculate that equal incident excitation fluence results in $\sim$ 7.7 times higher fluence or, equivalently, $\sim$ 3.85 times higher number of photons absorbed in the top-most GeSe layer. Assuming that each absorbed photon promotes one electron from the valence to the conduction band, it is not surprising

that we find the contribution to the THz emission of each photon absorbed in the surface layer to be approximately equal regardless of its wavelength. These observations are fully consistent with the surface shift as an origin of the THz emission. Fig. 4.5 (a) also shows that rotating the sample by 180^o while maintaining an unchanged pump polarization reverses the polarity of emission while the amplitude and temporal shape of the waveform show only minimal change. This observation unequivocally shows that the inversion symmetry breaking in the surface layer of GeSe dictates the emission polarity and supports the surface shift current as a mechanism of THz generation.

Fig. 4.6 provides a detailed analysis of THz emission dependence on sample orientation. While the amplitude of the THz emission is nearly an order of magnitude lower for 800 nm excitation, the waveforms for the two excitation wavelengths are qualitatively the same for every sample orientation. As Fig. 4.6 (a) and (d) demonstrate, the observed waveform shape for both 400 nm and 800 nm excitation is well-described by a sum of two simple single-cycle bipolar Gaussian waveforms (e.g., the first derivatives of the Gaussian pulses, Fig. 4.7).

This decomposition of THz emission into two single cycle transients at all sample orientations suggests the presence of two crystal grains within a 1.5 mm photoexcited area on the GeSe crystal, each characterized by a specific spontaneous polarization vector $\vec{P}$ that dictates the direction of the surface shift current. Fig. 4.8 (c) schematically illustrates the two grain as side-by-side as a result of a stacking fault; however, it is also possible that they fully or partially overlap, or that they originate from a rotational misalignment between GeSe layers within a crystal.

Each of the two transients is bipolar. Within the model described by Braun et al. [98], this indicates that momentum relaxation time is shorter than the pump pulse duration and does not affect the emitted waveform shape in a significant way. One of the single cycle waveforms (labeled as Wfm 1) has a Gaussian full width at half maximum (FWHM) of 1.0 ps $\pm$ 0.3 ps. Another one (Wfm 2) is delayed by 1.1 ps $\pm$0.2 ps and has a FWHM of 1.9 ps$\pm$0.6 ps. Delay in arrival time and longer duration of the second waveform indicate

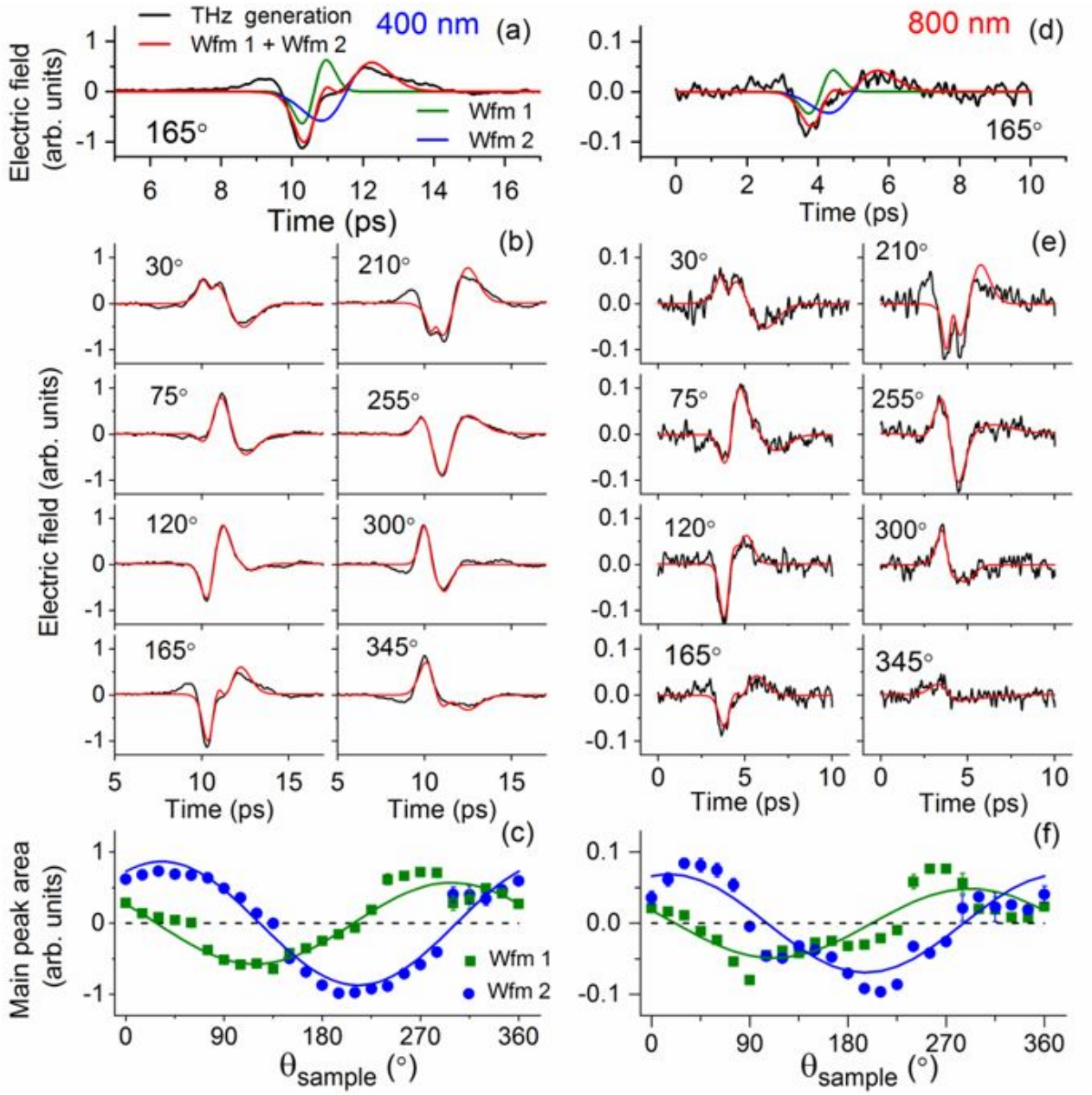

Figure 4.6: Dependence of THz emission excited with $\sim 190\mu J/cm^2$, 100 fs, 400 nm pulses (a-c) or with $\sim 130\mu J/cm^2$, 100 fs, 800 nm pulses (d-f), with $\Theta_{pump} = 0^o$ in both cases. (a) and (d) show examples of decomposition of the observed emission in two single cycle transients, waveform 1 (Wfm 1) and waveform 2 (Wfm 2), corresponding to two crystal grains with different intrinsic surface polarizations in the excitation spot, as illustrated schematically in Figure 2c. (b) and (e) show emitted waveforms (black curves) and model fits to two transients (red curves) at different sample orientations. (c) and (f) show area under the first peak of each of the two waveforms as a function of sample orientation. Symbols show the areas obtained from best model fits to the observed THz transients, and solid lines represent the fit of the data to a cosine function.

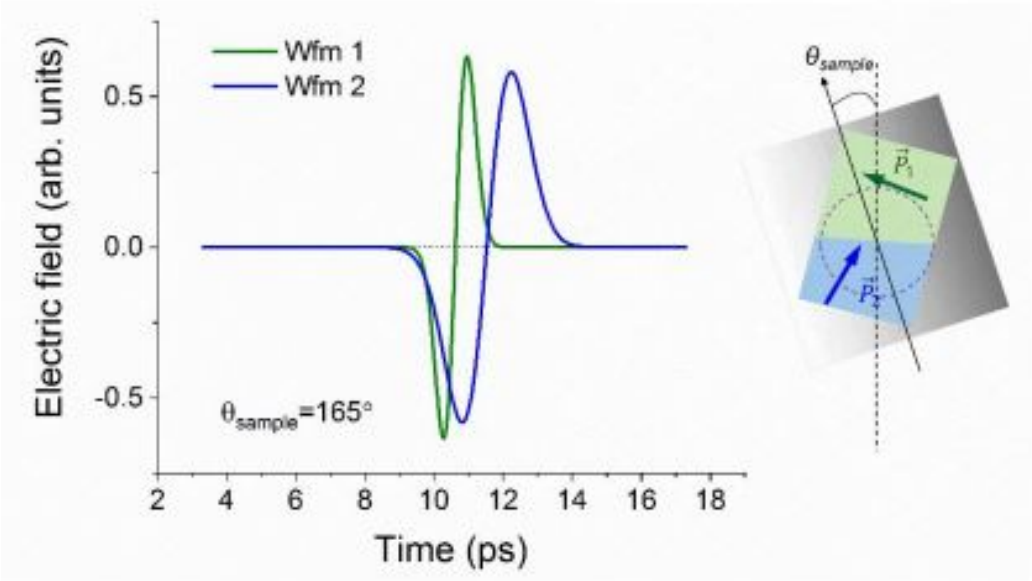

Figure 4.7: Model single cycle waveforms (Gaussian pulse derivatives) used to represent THz waveforms emitted by the surface shift current and transmitted through a few μm thick GeSe crystal. Each of the two waveforms represents emission by a shift current in a single crystalline grain, with the current direction determined by a spontaneous surface electric polarization in a specific grain, as illustrated in a schematic on the right. Based on the experimental observations, studied GeSe crystal had two distinct grains in a 1.5 mm diameter field of view, one with the polarization $\sim$ - 68^o relative to the detection axis, and another one - $\sim 30^o$.

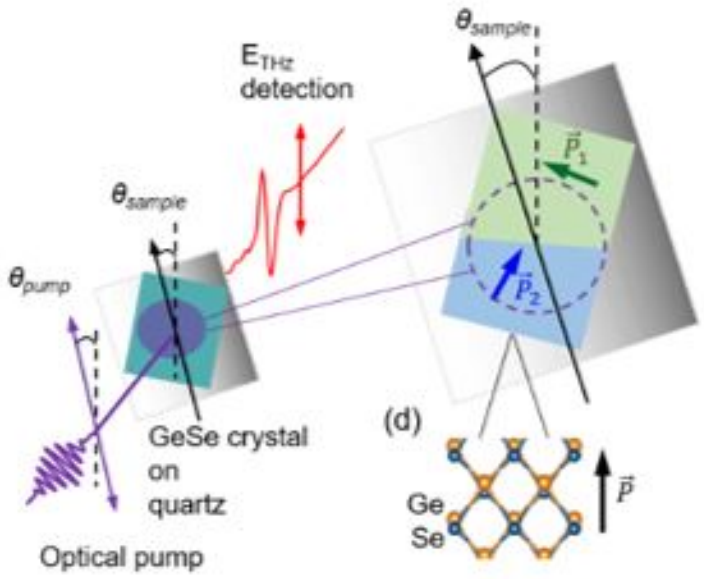

Figure 4.8: Illustration of the experimental geometry where sample orientation and linear polarization of an optical pump pulse are varied relative to the fixed polarization of the detected THz pulses. Schematic depiction of a GeSe crystal consisting of two crystal grain, each characterized by a spontaneous electric polarization vector along the armchair direction in the surface layer of GeSe.

that the thickness of the crystal grain that emits Wfm2 is larger. Fig. 4.6 (b) and (c) show model fits to experimental THz waveforms excited by 400 nm and 800 nm pulses. While simple Gaussian derivative pulses cannot account for a possible spectral chirp in each of the constituent pulses after propagation through the crystal, they adequately capture sample orientation dependence of emitted THz waveforms. Fig. 4.6 (c) and (f) plot the area under each of the model single cycle bipolar waveforms, with a sign that accounts for the polarity of the first peak of each waveform. For both waveforms, sined area follows a cosine dependence on the sample orientation. As we detect only one linearly polarized component of the emitted transient electric field, cosine dependence on sample orientation confirms that the shift current direction is determined by the intrinsic spontaneous surface polarization and associated with inversion symmetry breaking of each crystalline grain. Shift current flows along the spontaneous polarization and emits electromagnetic radiation with an electric field along this direction. Experimental waveforms represent a component of the emitted electromagnetic transient polarized along the detection axis. We find that for both 400 nm and 800 nm, waveform 1 has a positive maximum when the sample is rotated by 68° ± 4° from the (arbitrarily chosen) origin, while waveform 2 peaks at -30° ± 4°, with ∼ 98° between the polarization directions in the two grains. Those angles indicate the direction of the photoexcited shift current in each of the grains.

As discussed earlier, we hypothesize that the shift current flows in the armchair direction of GeSe lattice. We also expect strong THz absorption due the B_{3u} phonon which involves motion of Ge and Se atoms in opposite directions along the armchair direction. Indeed, as shown in Fig. 4.9, the incident THz pulse from a $ZnTe$ source is not only strongly attenuated but also split into two pulses delayed by ∼ 1.1 ps due to transmission through the two, a thinner and a thicker, grains in the 1.5 mm diameter THz spot size on the studied GeSe crystal (Fig. 4.9 (a)). Attenuation of the pulse transmitted through each grain is the strongest when it is polarized along the same direction as the THz pulses emitted by GeSe surface layer. For Θ_{sample} of 150^o or 330^o, spontaneous electric polarization of the thicker grain ($\vec{P}_2$) is

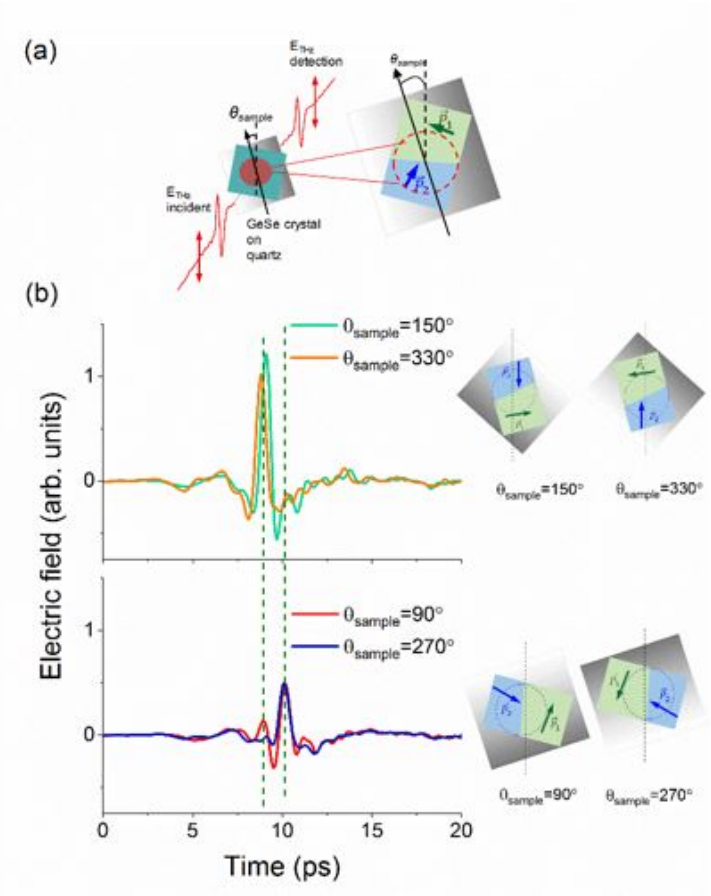

Figure 4.9: (a) Schematic diagram of measurement of absorption of incident THz pulses generated in a $ZnTe$ source by GeSe crystal as a function of GeSe orientation. (b) Transmission of a THz pulse through two grains with different thickness and orientations splits the incident pulse into two. When polarization of the incident THz pulse has a large component parallel to the spontaneous electric polarization in a grain, its absorption is significantly stronger.

approximately parallel to the incident THz polarization, and the second (delayed) peak is not present. At the same time, the polarization of the thinner grain has a large component that is perpendicular to the incident THz polarization, resulting in an incomplete attenuation of the first peak. We observe the opposite trends for sample orientations of 90^o and 270^o where the first peak is almost fully attenuated while a small fraction of the second peak remains after propagation through the crystal. These results confirm that polarization of the THz pulses emitted by the surface shift current in GeSe coincides with the direction of strongest attenuation by the infrared active phonons, underscoring that thinner crystals will result in a much brighter THz source.

4.1.3 Conclusion

In summary, we have presented experimental evidence of shift current generation in GeS nanosheets and bulk GeSe in response to above band gap excitation, supporting recent theoretical predictions of the shift current in these materials due to a spontaneous ferroelectric polarization that breaks inversion symmetry in the monolayer [78]. While the stacking sequence of the layers in this van der Waals material results in the inversion symmetry in the bulk, this symmetry is broken at the surface. We find that photoexcitation of GeS nanosheets with 400 nm pulses at normal incidence leads to emission of nearly single-cycle THz pulses without external bias voltage. In the case of GeSe crystals, radiation of nearly single-cycle THz pulses appears in response to either 800 nm (1.55 eV) or 400 nm (3.10 eV) excitation. Stronger THz emission in response to 400 nm excitation compared to the fluence of 800 nm excitation stems from stronger absorption of 400 nm light by GeSe which leads to the higher excitation of a surface layer. Excitation fluence, sample orientation and excitation polarization dependence of the THz emission confirm that shift current flowing along the spontaneous polarization of the surface layer is responsible for the observed emission in both cases. Highly efficient shift current in response to photoexcitation on the both short- and long-wave edges of the visible spectrum suggest applications of these layered materials in solar cells based on

the bulk photovoltaic effect. Efficient THz emission that is potentially tunable by strain can also be harnessed in the new nonlinear photonic devices, sensors and THz sources.

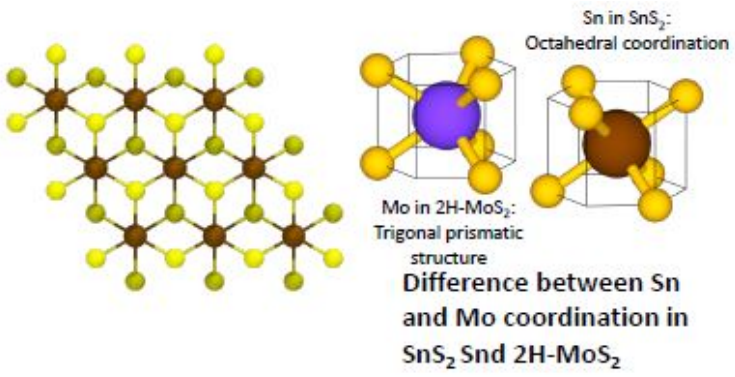

4.2 THz emission in SnS_2 single crystals

We have earlier discussed 2D SnS_2 as a promising for optoelectronic and solar energy conversion applications (Chapter 3.2). In this section, we focus on the TES experiments investigating potential excitation of ultrafast photocurrents in single crystalline SnS_2. Like in GeS and GeSe, THz emission in this material appear to be a function of crystal orientation. Observed only for above the bandgap excitation, it suggests that its origin is also a shift current. This observation is surprising due to inversion symmetry of unexcited SnS_2 even in a monolayer limit. We hypothesize that excitation of an in-plane phonon mode by the photoexcitation dynamically breaks this symmetry and results in THz emission. A detailed theoretical investigation of the impact of possible impulsive excitation of in-plane phonons, and the influence of these coherent lattice oscillations on the shift current, is still outstanding. However, we present here the results of experimental studies that can provide important inputs and checkpoints for theory of nonlinear effects in SnS_2.

4.2.1 Experimental methods

Synthesis of SnS_2 single crystals has been discussed in Chapter 3.2, and detailed procedures can be found in Giri et al [106].

TES measurements were carried out in the same geometry discussed earlier in this Chapter. SnS_2 samples were excited at normal incidence with 100-400 $\mu J/cm^2$, 400 nm pulses, as

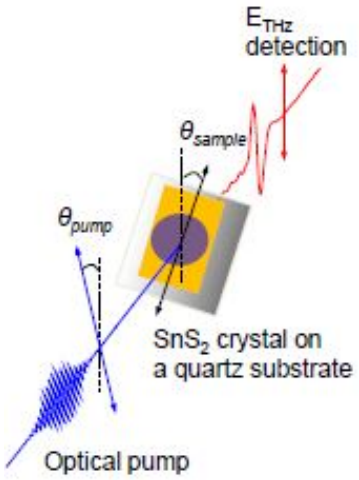

Figure 4.10: Scheme of the sample photoexcitation.

shown in Fig. 4.10.

4.2.2 Results and discussions

Above bandgap photoexcitation of SnS_2 crystals results in transient photoconductivity and emission of THz pulses, as shown in the Fig. 4.11, where on top of the decays additional waveform that correspond to the THz generation can be seen. THz emission by SnS_2 crystals is dependent on sample orientation while transient photoconductivity is not. Transient photoconductivity dynamics were obtained in previous Chapter 3.2 by subtracting THz generation by the sample from TRTS decay. More detailed information about transient conductivity of SnS_2 single crystals can be found in the Chapter 3.2. Here, we focus on THz emission that has been observed in multiple (over 10) studied SnS_2 crystals in response to excitation with 400 nm pulses.

THz generation exhibits clear three-fold symmetry with respect to sample rotation, as shown in the Fig. 4.12. The solid line in Fig. 4.12 (c) on the left is a fit of THz signal peak amplitude to $A\cos(3\Theta_{sample} + \Theta_0)$. The observed bandwidth of the emitted pulses is likely limited by the bandwidth of the $ZnTe$ detector (0.2-2.5 THz), indicating that processes responsible for the THz emission occur on a sub-picosecond timescale.

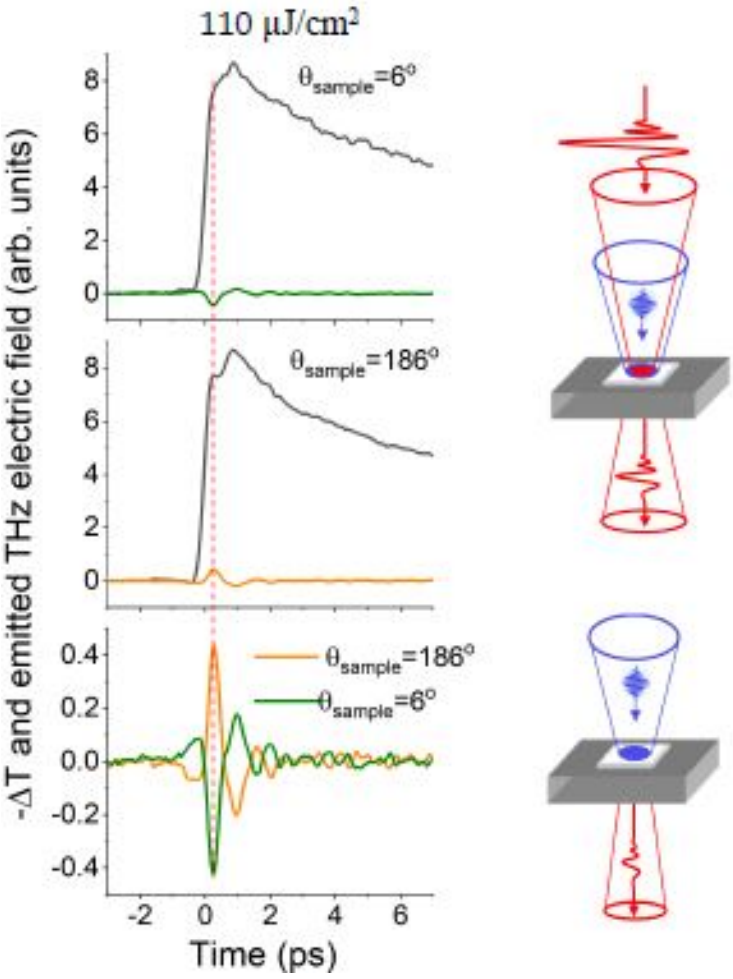

Figure 4.11: Transient photoconductivity and emission of THz pulses.

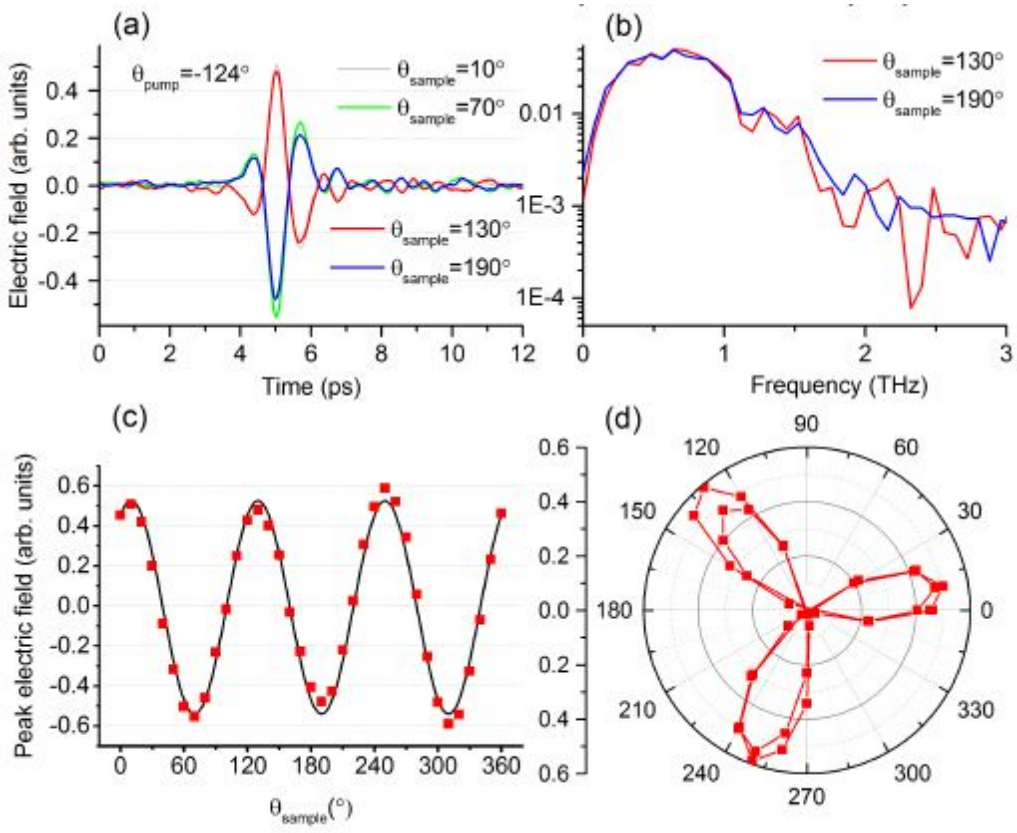

Figure 4.12: THz emission of SnS_2 crystal with the response to sample orientation. Optical pump polarization is fixed.

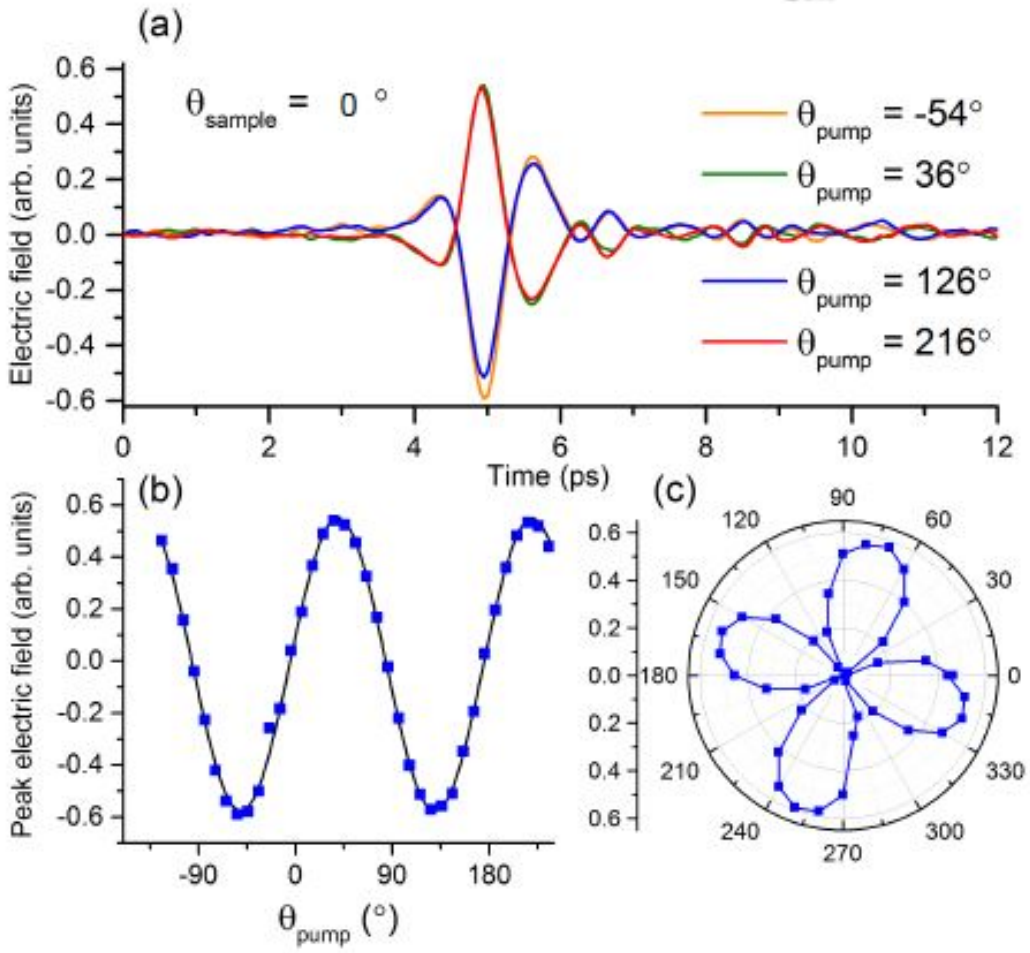

Figure 4.13: THz emission of SnS_2 crystal with the response to optical pump polarization orientation. Sample orientation is fixed.

THz generation exhibits four-fold symmetry with respect to pump polarization, as shown in the Fig. 4.13. Four-fold symmetry instead of three-fold symmetry is a result of detection of only one (vertical) component of the emitted THz radiation, as has been discussed in reports of THz as well as second harmonic generation from MoS_2 monolayers and surfaces [172].

What can be the mechanism of THz generation of SnS_2 single crystals? Since it is observed in response to above bandgap excitation (400 nm) but not below bandgap excitation, a transient current rather that a transient polarization acts as a source of electromagnetic pulse emission. As discussed earlier in Chapter 2.5 and Chapter 4.1, experiments carried out at normal incidence without external bias rule out the photo-Dember effect, built-in

surface depletion fields, or photon drag. Uniform illumination with a spot size larger than the focus of THz-collecting optics eliminated laser-induced Seebeck effect, and single-color, linear polarization of excitation excludes injection current. Moreover, a three-fold symmetry of emission as shown in Figure 4.12 is compatible with the crystal lattice structure and suggests that we are observing either ultrafast photocurrents flowing in a direction from sulfur atom to tin along the bonds (shift currents) or THz emission by a coherently excited infrared-active in-plane phonon mode [173, 174].

In either case, coherent lattice dynamics are likely to play a pivotal role. Shift current is a second-order nonlinear effect and is therefore prohibited in centrosymmetric materials. SnS_2 (space group $P3m1$) has inversion symmetry in both bulk as well as monolayer form, unlike, for example, MoS_2 where monolayers are non-centrosymmetric. In order to explain experimental results, we hypothesize that linearly polarized photoexcitation results in a dynamic, transient breaking of inversion symmetry by coherent excitation of a specific phonon mode. Photoexcitation with femtosecond pulses have been shown to excite coherent lattice oscillations in a variety of materials such as crystalline Te, $GaAs$, Bi_2Te_3, etc [175, 176, 177, 178, 179]. A coherent phonon then results in a transient inversion symmetry breaking. THz emission in this case can occur either as a direct result of emission by a phonon mode [173, 174], or due to a shift current excited by a $\sim$ 100 fs optical pulse during the half-period of a phonon. A candidate phonon mode in SnS_2 is an infrared-acive E_u mode at $\sim$ 6.1 THz [175], but other modes, including those not at a Brillouin zone center, can contribute. Elucidation of the exact mechanism and development of a model that captures its properties requires a first principles dynamical calculation of phonon structure, and this work is on-going.

Understanding the mechanism behind THz emission in SnS_2 without external bias will pave the way to novel applications in solar energy conversion and ultrafast electro-optical devices.

Chapter 5

Conclusion and future work

This thesis has outlined experiments that advanced the use of the time resolved THz spectroscopy and THz emission spectroscopy techniques. We have reported on our use of these tools to study chalcogenide semiconductors, which are of interest from both a technological and experimental point of view. These materials are characterized by high carrier mobility and band gaps in the visible to near-infrared range, and are well suited for efficient solar energy conversion applications. They can be produced using inexpensive, high throughput deposition methods, and do not suffer from the environmental toxicity and instability that plague conventional perovskite solar cells. Chalcogenides include a wide range of sulfides and selenides, such as GeS, GeSe, SnSe, SnS_2, Bi_2S_3, and Bi_2Se_3 [34, 180, 181, 182, 183, 184, 185].

Over the course of this work, we have reported on time-resolved THz spectroscopy studies of 2D chalcogenides $(Bi_{1-x}In_x)_2Se_3$, SnS_2, and GeS, as well as polycrystaline systems of Bi_2S_3, PbS, and PbS/ZnO.

In the case of $(Bi_{1-x}In_x)_2Se_3$, which undergoes transformation from a topological to a band insulator for $x > 0.06$, we have used time-resolved THz spectroscopy to investigate photoexcited carrier dynamics. In Bi_2Se_3, we have measured the time it takes an optically excited carrier to undergo transition from bulk conduction band states into high mobility topological surface states, as well as the mobility of optically excited carriers in the two distinct sets of Dirac surface states at different energies in the conduction band. In the case of $(Bi_{0.75}In_{0.25})_2Se_3$ and $(Bi_{0.5}In_{0.5})_2Se_3$, which are insulating without photoexcitation, transport of photoexcited free carriers is affected by their twin domain boundaries and disorder. We have also demonstrated that the mobility and lifetime of the photoexcited carriers in

$(Bi_{1-x}In_x)_2Se_3$ films can be tuned by its indium content, enabling tailoring of band insulators that have desired optoelectronic properties and are fully structurally compatible with the topological insulator Bi_2Se_3 for applications in high-speed photonic devices based on topological insulator/band insulator heterostructures [107].

In SnS_2, TRTS allowed us to access intrinsic carrier mobility in vertical SnS_2 nanoflake arrays. We found that the intrinsic carrier mobility within the nanoflakes is exceptionally high, 330 cm^2/Vs, and is comparable to the mobility observed in a single crystal SnS_2 at 800 cm^2/Vs [186]. Similarly, we have investigated photoexcited carrier dynamics in nanoribbons of GeS, a 2D semiconductor with high carrier mobility and a moderate band gap of $\sim$ 1.5 eV. Ongoing efforts are dedicated to investigating the influence of zero-valent metal intercalation on the photoconductivity of GeS. Our preliminary results show that intercalation of Cu, Au, or Sn impacts the free carrier lifetime and carrier scattering time, highlighting the potential of zero-valent metal intercalation for engineering the optoelectronic properties of GeS nanostructures for application in high-speed electronic devices.

In addition to layered chalcogenides, we studied quasi-3D chalcogenide systems such as nano- and polycrystalline Bi_2S_3 and PbS. In Bi_2S_3, we have shown that annealing nanocrystalline films increases photoexcited carrier lifetimes and diffusion lengths, showing a pathway to optimization of its properties for solar energy conversion [105]. In polycrystalline PbS, carrier lifetime and mobility was found to be high within the grains, but injection of carriers from the individual grains to ZnO, a charge collector, is suppressed by interface trap states. This observation underscores the need for chemical passivation of PbS/ZnO interfaces to achieve efficient injection of photoexcited carriers into ZnO. Future work will focus on using buffer layers to minimize interfacial recombination and enable the transfer of photoexcited electrons from PbS into ZnO electrodes [104].

We also used TRTS spectroscopy to study ultrafast photoexcited carrier dynamics in a number of non-chalcogenide materials. Those results were not included in this thesis, but can be found in several journal publications and conference proceedings. Specifically, we

have studied the properties of reduced graphene oxide films for electromagnetic interference shielding in the GHz and THz range, finding that their performance can be engineered by intercalation of metals such as Zn, Ni or Fe. Another candidate conductive 2D material with potential for electromagnetic interference shielding over a broad spectral range is an emerging class of 2D transition metal carbides, MXenes. We have reported on the equilibrium and non-equilibrium free carrier dynamics of $Ti_3C_2T_x$, gleaned from THz spectroscopic studies for the first time. $Ti_3C_2T_x$ showed high ($\sim 2 \times 10^{21} cm^{-3}$) intrinsic charge carrier density and relatively high ($\sim 34 cm^2/Vs$) mobility of carriers with an exceptionally large ($\sim 46000 cm^{-1}$) absorption in the THz range, suggesting that $Ti_3C_2T_x$ is well suited for both THz detection and electromagnetic interference shielding. We also demonstrated that $Ti_3C_2T_x$ conductivity and THz transmission can be manipulated by photoexcitation, as absorption of near-infrared, 800 nm pulses is found to cause transient suppression of the conductivity that recovers over hundreds of picoseconds. The possibility of control over THz transmission and conductivity by photoexcitation suggests the promise for application of $Ti_3C_2T_x$ MXenes in THz modulation devices and variable electromagnetic shielding [187]. We have also applied TRTS to organic semiconductors and elucidated photoexcited carrier transport in these materials, which hold much promise for low cost, lightweight, flexible/stretchable organic semiconductor structures that can harness solar energy [188].

Finally, this thesis reports on our investigations of ultrafast photocurrents in germanium monochalcogenides GeS and GeSe using THz emission spectroscopy (TES). We presented the first experimental evidence of emission of THz pulses in response to above band gap photoexcitation of a GeS nanosheets and bulk GeSe crystals [33, 82]. Optical excitation in these materials results in an instantaneous spatial shift of electron density distribution, giving rise to shift current, a mechanism behind the bulk photovoltaic effect. While the stacking sequence of the layers in both GeS and GeSe results in inversion symmetry in bulk, this symmetry is broken on the surface. Excitation fluence, sample orientation, and excitation polarization dependence of the THz emission confirm that shift current flowing along the

spontaneous polarization of the surface layer is responsible for the observed emission in both cases. Highly efficient shift current in response to photoexcitation on both the short- and long-wave edges of the visible spectrum suggest applications of these layered materials in solar cells based on the bulk photovoltaic effect [33, 82].

Using TES, we have also discovered that single crystalline SnS_2 exhibits robust THz emission, whose origin we believe to be a shift current resulting from transient symmetry breaking by a linearly polarized excitation. Ongoing efforts focus on investigating ultrafast dynamics of charge carriers and lattice excitations in this unique material, with the goal of uncovering the mechanisms that drive THz emission.

The information gained from these studies comes at a crucial moment and will guide a new generation of photovoltaics, nonlinear photonic devices and alternative THz sources.

Bibliography

[1] Chaoliang Tan, Xiehong Cao, Xue-Jun Wu, Qiyuan He, Jian Yang, Xiao Zhang, Junze Chen, Wei Zhao, Shikui Han, Gwang-Hyeon Nam, et al. Recent advances in ultrathin two-dimensional nanomaterials. *Chemical reviews*, 117(9):6225–6331, 2017. 2

[2] Hua Zhang. Ultrathin two-dimensional nanomaterials. *ACS Nano*, 9(10):9451–9469, 2015. 2

[3] Jason B Baxter and Glenn W Guglietta. Terahertz spectroscopy. *Analytical chemistry*, 83(12):4342–4368, 2011. 5

[4] Masayoshi Tonouchi. Cutting-edge terahertz technology. *Nature photonics*, 1(2):97–105, 2007. 4

[5] Ch Fattinger and D Grischkowsky. Terahertz beams. *Applied Physics Letters*, 54(6):490–492, 1989. 4

[6] D Grischkowsky, Søren Keiding, Martin Van Exter, and Ch Fattinger. Far-infrared time-domain spectroscopy with terahertz beams of dielectrics and semiconductors. *JOSA B*, 7(10):2006–2015, 1990. 4

[7] Bradley Ferguson and Xi-Cheng Zhang. Materials for terahertz science and technology. *Nature materials*, 1(1):26–33, 2002. 4

[8] Edward Philip John Parrott, Yiwen Sun, and Emma Pickwell-MacPherson. Terahertz spectroscopy: Its future role in medical diagnoses. *Journal of Molecular Structure*, 1006(1-3):66–76, 2011. 4

[9] John F Federici, Brian Schulkin, Feng Huang, Dale Gary, Robert Barat, Filipe Oliveira,

and David Zimdars. Thz imaging and sensing for security applications—explosives, weapons and drugs. *Semiconductor Science and Technology*, 20(7):S266, 2005. 4

[10] Sunil K Mathanker, Paul R Weckler, and Ning Wang. Terahertz (thz) applications in food and agriculture: A review. *Transactions of the ASABE*, 56(3):1213–1226, 2013. 4

[11] CH Lui, AJ Frenzel, DV Pilon, Y-H Lee, X Ling, GM Akselrod, J Kong, and N Gedik. Trion-induced negative photoconductivity in monolayer mos 2. *Physical review letters*, 113(16):166801, 2014. 4

[12] Zuanming Jin, Dominik Gehrig, Clare Dyer-Smith, Edwin J Heilweil, Frederic Laquai, Mischa Bonn, and Dmitry Turchinovich. Ultrafast terahertz photoconductivity of photovoltaic polymer-fullerene blends: A comparative study correlated with photovoltaic device performance. *The journal of physical chemistry letters*, 5(21):3662–3668, 2014. 4

[13] Tobias Kampfrath, Alexander Sell, Gregor Klatt, Alexej Pashkin, Sebastian Mahrlein, Thomas Dekorsy, Martin Wolf, Manfred Fiebig, Alfred Leitenstorfer, and Rupert Huber. Coherent terahertz control of antiferromagnetic spin waves. *Nature Photonics*, 5(1):31–34, 2011. 4

[14] Sebastian Baierl, Matthias Hohenleutner, Tobias Kampfrath, AK Zvezdin, Alexey V Kimel, Rupert Huber, and RV Mikhaylovskiy. Nonlinear spin control by terahertz-driven anisotropy fields. *Nature Photonics*, 10(11):715, 2016. 4

[15] KT Butler, BJ Dringoli, L Zhou, PM Rao, Aron Walsh, and LV Titova. Ultrafast carrier dynamics in bivo 4 thin film photoanode material: interplay between free carriers, trapped carriers and low-frequency lattice vibrations. *Journal of Materials Chemistry A*, 4(47):18516–18523, 2016. 4

[16] Rupert Huber, F Tauser, A Brodschelm, M Bichler, G Abstreiter, and A Leitenstorfer.

How many-particle interactions develop after ultrafast excitation of an electron–hole plasma. *Nature*, 414(6861):286–289, 2001. 4

[17] M Schall, M Walther, and P Uhd Jepsen. Fundamental and second-order phonon processes in cdte and znte. *Physical Review B*, 64(9):094301, 2001. 4, 22

[18] RHM Groeneveld and D Grischkowskyt. Picosecond time-resolved far-infrared experiments on carriers and excitons in gaas–algaas multiple quantum wells. *JOSA B*, 11(12):2502–2507, 1994. 4

[19] Robert A Kaindl, Marc A Carnahan, Joseph Orenstein, Daniel S Chemla, Hans M Christen, Hong-Ying Zhai, Mariappan Paranthaman, and Doug H Lowndes. Far-infrared optical conductivity gap in superconducting mgb 2 films. *Physical review letters*, 88(2):027003, 2001. 4

[20] David H Auston, Kin P Cheung, and Peter R Smith. Picosecond photoconducting hertzian dipoles. *Applied physics letters*, 45(3):284–286, 1984. 6

[21] YC Shen, PC Upadhya, EH Linfield, HE Beere, and AG Davies. Ultrabroadband terahertz radiation from low-temperature-grown gaas photoconductive emitters. *Applied physics letters*, 83(15):3117–3119, 2003. 7

[22] P Uhd Jepsen, David G Cooke, and Martin Koch. Terahertz spectroscopy and imaging–modern techniques and applications. *Laser & Photonics Reviews*, 5(1):124–166, 2011. 9, 22

[23] Frank Träger. *Springer handbook of lasers and optics*. Springer Science & Business Media, 2012. 9

[24] Patrick Steglich, Christian Mai, Claus Villringer, and Andreas Mai. Direct observation and simultaneous use of linear and quadratic electro-optical effects. *Journal of Physics D: Applied Physics*, 53(12):125106, 2020. 9

[25] Yun-Shik Lee. *Principles of terahertz science and technology*, volume 170. Springer Science & Business Media, 2009. 9, 10

[26] Paul CM Planken, Han-Kwang Nienhuys, Huib J Bakker, and Tom Wenckebach. Measurement and calculation of the orientation dependence of terahertz pulse detection in znte. *JOSA B*, 18(3):313–317, 2001. 9

[27] A Rice, Y Jin, XF Ma, X-C Zhang, D Bliss, J Larkin, and M Alexander. Terahertz optical rectification from¡ 110¿ zinc-blende crystals. *Applied physics letters*, 64(11):1324–1326, 1994. 9

[28] Q Wu and X-C Zhang. 7 terahertz broadband gap electro-optic sensor. *Applied Physics Letters*, 70(14):1784–1786, 1997. 9

[29] Rupert Huber, A Brodschelm, F Tauser, and A Leitenstorfer. Generation and field-resolved detection of femtosecond electromagnetic pulses tunable up to 41 thz. *Applied Physics Letters*, 76(22):3191–3193, 2000. 9

[30] C Kübler, Rupert Huber, S Tübel, and A Leitenstorfer. Ultrabroadband detection of multi-terahertz field transients with gase electro-optic sensors: Approaching the near infrared. *Applied physics letters*, 85(16):3360–3362, 2004. 9

[31] X-C Zhang, XF Ma, Y Jin, T-M Lu, EP Boden, PD Phelps, KR Stewart, and CP Yakymyshyn. Terahertz optical rectification from a nonlinear organic crystal. *Applied Physics Letters*, 61(26):3080–3082, 1992. 9

[32] Arno Schneider, Max Neis, Marcel Stillhart, Blanca Ruiz, Rizwan UA Khan, and Peter Günter. Generation of terahertz pulses through optical rectification in organic dast crystals: theory and experiment. *JOSA B*, 23(9):1822–1835, 2006. 9

[33] Kateryna Kushnir, Mengjing Wang, Patrick D. Fitzgerald, Kristie J. Koski, and Lyubov V. Titova. Ultrafast zero-bias photocurrent in ges nanosheets: Promise for photovoltaics. *ACS Energy Letters*, 2(6):1429–1434, 2017. 9, 45, 78, 106, 128, 129

[34] Kateryna Kushnir, Ying Qin, Yuxia Shen, Guangjiang Li, Benjamin M. Fregoso, Sefaattin Tongay, and Lyubov V. Titova. Ultrafast zero-bias surface photocurrent in germanium selenide: Promise for terahertz devices and photovoltaics. *ACS Applied Materials and Interfaces*, 11(5):5492–5498, 2019. 9, 106, 126

[35] Mark Bieler. Thz generation from resonant excitation of semiconductor nanostructures: Investigation of second-order nonlinear optical effects. *IEEE Journal of Selected Topics in Quantum Electronics*, 14(2):458–469, 2008. 10, 50

[36] JE Sipe and AI Shkrebtii. Second-order optical response in semiconductors. *Physical Review B*, 61(8):5337, 2000. 10, 44, 48

[37] KH Yang, PL Richards, and YR Shen. Generation of far-infrared radiation by picosecond light pulses in linbo3. *Applied Physics Letters*, 19(9):320–323, 1971. 10

[38] A Méndez, G De la Paliza, A Garcia-Cabanes, and JM Cabrera. Comparison of the electro-optic coefficient r33 in well-defined phases of proton exchanged linbo3 waveguides. *Applied Physics B*, 73(5):485–488, 2001. 10

[39] Janos Hebling, Ka-Lo Yeh, Matthias C Hoffmann, Balazs Bartal, and Keith A Nelson. Generation of high-power terahertz pulses by tilted-pulse-front excitation and their application possibilities. *JOSA B*, 25(7):B6–B19, 2008. 10

[40] Janos Hebling, Gabor Almasi, Ida Z Kozma, and Jürgen Kuhl. Velocity matching by pulse front tilting for large-area thz-pulse generation. *Optics Express*, 10(21):1161–1166, 2002. 10

[41] H Hirori, A Doi, F Blanchard, and K Tanaka. Single-cycle terahertz pulses with amplitudes exceeding 1 mv/cm generated by optical rectification in linbo 3. *Applied Physics Letters*, 98(9):091106, 2011. 10

[42] Jianming Dai, Jingle Liu, and Xi-Cheng Zhang. Terahertz wave air photonics: terahertz wave generation and detection with laser-induced gas plasma. *IEEE Journal of selected topics in Quantum Electronics*, 17(1):183–190, 2010. 11

[43] DJ Cook and RM Hochstrasser. Intense terahertz pulses by four-wave rectification in air. *Optics letters*, 25(16):1210–1212, 2000. 11

[44] Markus Kress, Torsten Löffler, Susanne Eden, Mark Thomson, and Hartmut G Roskos. Terahertz-pulse generation by photoionization of air with laser pulses composed of both fundamental and second-harmonic waves. *Optics letters*, 29(10):1120–1122, 2004. 11

[45] Paul B Corkum. Plasma perspective on strong field multiphoton ionization. *Physical review letters*, 71(13):1994, 1993. 11

[46] Jianming Dai, Xu Xie, and X-C Zhang. Detection of broadband terahertz waves with a laser-induced plasma in gases. *Physical review letters*, 97(10):103903, 2006. 12

[47] HG Roskos, MD Thomson, M Kreß, Löffler, and T. Broadband thz emission from gas plasmas induced by femtosecond optical pulses: From fundamentals to applications. *Laser & photonics reviews*, 1(4):349–368, 2007. 12

[48] Tom Seifert, S Jaiswal, U Martens, J Hannegan, Lukas Braun, Pablo Maldonado, F Freimuth, A Kronenberg, J Henrizi, I Radu, et al. Efficient metallic spintronic emitters of ultrabroadband terahertz radiation. *Nature photonics*, 10(7):483–488, 2016. 13, 45, 47

[49] Xi-Cheng Zhang and Jingzhou Xu. *Introduction to THz wave photonics*, volume 29. Springer, 2010. 14

[50] Withawat Withayachumnankul and Mira Naftaly. Fundamentals of measurement in terahertz time-domain spectroscopy. *Journal of Infrared, Millimeter, and Terahertz Waves*, 35(8):610–637, 2014. 16, 20

[51] Peter Uhd Jepsen. Phase retrieval in terahertz time-domain measurements: a "how to" tutorial. *Journal of Infrared, Millimeter, and Terahertz Waves*, 40(4):395–411, 2019. 16

[52] Ioachim Pupeza, Rafal Wilk, and Martin Koch. Highly accurate optical material parameter determination with thz time-domain spectroscopy. *Optics express*, 15(7):4335–4350, 2007. 16

[53] *Probing Organic Semiconductors with Terahertz Pulses*, pages 367–428. 22, 28, 35, 42, 63

[54] Charles A Schmuttenmaer. Exploring dynamics in the far-infrared with terahertz spectroscopy. *Chemical reviews*, 104(4):1759–1780, 2004. 22

[55] MC Nuss, DH Auston, and F Capasso. Direct subpicosecond measurement of carrier mobility of photoexcited electrons in gallium arsenide. *Physical review letters*, 58(22):2355, 1987. 22

[56] Jason B Baxter and Charles A Schmuttenmaer. Conductivity of zno nanowires, nanoparticles, and thin films using time-resolved terahertz spectroscopy. *The Journal of Physical Chemistry B*, 110(50):25229–25239, 2006. 22, 86

[57] Patrick Parkinson, Hannah J Joyce, Qiang Gao, Hark Hoe Tan, Xin Zhang, Jin Zou, Chennupati Jagadish, Laura M Herz, and Michael B Johnston. Carrier lifetime and mobility enhancement in nearly defect-free core- shell nanowires measured using time-resolved terahertz spectroscopy. *Nano letters*, 9(9):3349–3353, 2009. 22

[58] Matthew C Beard, Gordon M Turner, and Charles A Schmuttenmaer. Size-dependent photoconductivity in cdse nanoparticles as measured by time-resolved terahertz spectroscopy. *Nano letters*, 2(9):983–987, 2002. 22, 44

[59] DG Cooke, AN MacDonald, A Hryciw, J Wang, Q Li, A Meldrum, and FA Hegmann. Transient terahertz conductivity in photoexcited silicon nanocrystal films. *Physical Review B*, 73(19):193311, 2006. 22, 42

[60] O Ostroverkhova, DG Cooke, S Shcherbyna, RF Egerton, FA Hegmann, RR Tykwinski, and JE Anthony. Bandlike transport in pentacene and functionalized pentacene thin films revealed by subpicosecond transient photoconductivity measurements. *Physical Review B*, 71(3):035204, 2005. 22

[61] O Ostroverkhova, DG Cooke, FA Hegmann, JE Anthony, Vitaly Podzorov, ME Gershenson, OD Jurchescu, and TTM Palstra. Ultrafast carrier dynamics in pentacene, functionalized pentacene, tetracene, and rubrene single crystals. *Applied physics letters*, 88(16):162101, 2006. 22

[62] Matthias Beck, Maximilian Klammer, S Lang, Paul Leiderer, Viktor V Kabanov, GN Gol'Tsman, and Jure Demsar. Energy-gap dynamics of superconducting nbn thin films studied by time-resolved terahertz spectroscopy. *Physical Review Letters*, 107(17):177007, 2011. 22

[63] Matthew C Beard, Gordon M Turner, and Charles A Schmuttenmaer. Measuring intramolecular charge transfer via coherent generation of thz radiation. *The Journal of Physical Chemistry A*, 106(6):878–883, 2002. 22

[64] Petr Kužel and Jan Petzelt. Time-resolved terahertz transmission spectroscopy of dielectrics. *Ferroelectrics*, 239(1):79–86, 2000. 22

[65] James T Kindt and Charles A Schmuttenmaer. Theory for determination of the low-frequency time-dependent response function in liquids using time-resolved terahertz pulse spectroscopy. *The Journal of chemical physics*, 110(17):8589–8596, 1999. 22

[66] Matthew C. Beard, Gordon M. Turner, and Charles A. Schmuttenmaer. Subpicosecond

carrier dynamics in low-temperature grown gaas as measured by time-resolved terahertz spectroscopy. *Journal of Applied Physics*, 90(12):5915–5923, 2001. 27

[67] Frank A Hegmann and Kristine PH Lui. Optical pump-terahertz probe investigation of carrier relaxation in radiation-damaged silicon-on-sapphire. In *Ultrafast Phenomena in Semiconductors VI*, volume 4643, pages 31–41. International Society for Optics and Photonics, 2002. 30

[68] Mark Lundstrom. *Fundamentals of carrier transport*. Cambridge university press, 2009. 32, 33

[69] Harald Ibach and Hans Lueth. Solid-state physics. an introduction to principles of materials science. 4. ext. upd. and enl. 2009. 34

[70] NV Smith. Classical generalization of the drude formula for the optical conductivity. *Physical Review B*, 64(15):155106, 2001. 42

[71] Lyubov V. Titova, Tyler L. Cocker, David G. Cooke, Xiongyao Wang, Al Meldrum, and Frank A. Hegmann. Ultrafast percolative transport dynamics in silicon nanocrystal films. *Physical Review B*, 83(8):085403, 2011. PRB. 42, 63, 86

[72] Lyubov V. Titova, Tyler L. Cocker, Sijia Xu, Jean-Marc Baribeau, Xiaohua Wu, David J. Lockwood, and Frank A. Hegmann. Ultrafast carrier dynamics and the role of grain boundaries in polycrystalline silicon thin films grown by molecular beam epitaxy. *Semiconductor Science and Technology*, 31(10):105017, 2016. 42, 86

[73] Tyler L Cocker, Devin Baillie, Miles Buruma, Lyubov V Titova, Richard D Sydora, Frank Marsiglio, and Frank A Hegmann. Microscopic origin of the drude-smith model. *Physical Review B*, 96(20):205439, 2017. 42

[74] James M. Schleicher, Shayne M. Harrel, and Charles A. Schmuttenmaer. Effect of spin-polarized electrons on terahertz emission from photoexcited gaas. *Journal of Applied Physics*, 105(11):113116, 2009. 44

[75] N Laman, M Bieler, and HM Van Driel. Ultrafast shift and injection currents observed in wurtzite semiconductors via emitted terahertz radiation. *Journal of applied physics*, 98(10):103507, 2005. 44, 50

[76] Tobias Kampfrath, Marco Battiato, Pablo Maldonado, G Eilers, J Notzold, Sebastian Mahrlein, V Zbarsky, Frank Freimuth, Yuriy Mokrousov, Stefan Blugel, et al. Terahertz spin current pulses controlled by magnetic heterostructures. *Nature nanotechnology*, 8(4):256–260, 2013. 44, 48

[77] F Nastos and JE Sipe. Optical rectification and current injection in unbiased semiconductors. *Physical Review B*, 82(23):235204, 2010. 44, 103

[78] Ashley M Cook, Benjamin M Fregoso, Fernando De Juan, Sinisa Coh, and Joel E Moore. Design principles for shift current photovoltaics. *Nature communications*, 8(1):1–9, 2017. 44, 51, 78, 79, 103, 104, 107, 118

[79] Woo-Jung Lee, Jin Won Ma, Jung Min Bae, Kwang-Sik Jeong, Mann-Ho Cho, Chul Kang, and Jung-Sub Wi. Strongly enhanced thz emission caused by localized surface charges in semiconducting germanium nanowires. *Scientific reports*, 3(1):1–9, 2013. 44

[80] VN Trukhin, AS Buyskikh, NA Kaliteevskaya, AD Bourauleuv, LL Samoilov, Yu B Samsonenko, GE Cirlin, MA Kaliteevski, and AJ Gallant. Terahertz generation by gaas nanowires. *Applied Physics Letters*, 103(7):072108, 2013. 44

[81] Kouhei Takahashi, Tsutomu Kanno, Akihiro Sakai, Hiromasa Tamaki, Hideo Kusada, and Yuka Yamada. Terahertz radiation via ultrafast manipulation of thermoelectric conversion in thermoelectric thin films. *Advanced Optical Materials*, 2(5):428–434, 2014. 45

[82] Kateryna Kushnir, Ying Qin, Yuxia Shen, Guangjiang Li, Benjamin M Fregoso, Sefaattin Tongay, and Lyubov V Titova. Ultrafast zero-bias surface photocurrent in

germanium selenide: Promise for terahertz devices and photovoltaics. *ACS applied materials & interfaces*, 11(5):5492–5498, 2019. 45, 128, 129

[83] Tom S Seifert, Samridh Jaiswal, Joseph Barker, Sebastian T Weber, Ilya Razdolski, Joel Cramer, Oliver Gueckstock, Sebastian F Maehrlein, Lukas Nadvornik, Shun Watanabe, et al. Femtosecond formation dynamics of the spin seebeck effect revealed by terahertz spectroscopy. *Nature communications*, 9(1):1–11, 2018. 45, 47

[84] Garik Torosyan, Sascha Keller, Laura Scheuer, Rene Beigang, and Evangelos Th Papaioannou. Optimized spintronic terahertz emitters based on epitaxial grown fe/pt layer structures. *Scientific reports*, 8(1):1–9, 2018. 45, 47

[85] Tom Seifert, S Jaiswal, Mohsen Sajadi, G Jakob, S Winnerl, Martin Wolf, M Kläui, and Tobias Kampfrath. Ultrabroadband single-cycle terahertz pulses with peak fields of 300 kv cm- 1 from a metallic spintronic emitter. *Applied Physics Letters*, 110(25):252402, 2017. 45, 47, 48

[86] Ping Gu, Masahiko Tani, Shunsuke Kono, Kiyomi Sakai, and X-C Zhang. Study of terahertz radiation from inas and insb. *Journal of Applied Physics*, 91(9):5533–5537, 2002. 47, 48

[87] Antanas Reklaitis. Terahertz emission from inas induced by photo-dember effect: Hydrodynamic analysis and monte carlo simulations. *Journal of Applied Physics*, 108(5):053102, 2010. 47, 48

[88] L Zhu, Y Huang, Z Yao, B Quan, Longhui Zhang, J Li, C Gu, X Xu, and Z Ren. Enhanced polarization-sensitive terahertz emission from vertically grown graphene by a dynamical photon drag effect. *Nanoscale*, 9(29):10301–10311, 2017. 47, 82

[89] Petr A Obraztsov, Tommi Kaplas, Sergey V Garnov, Makoto Kuwata-Gonokami, Alexander N Obraztsov, and Yuri P Svirko. All-optical control of ultrafast photocurrents in unbiased graphene. *Scientific reports*, 4(1):1–6, 2014. 47

[90] Petr A Obraztsov, Natsuki Kanda, Kuniaki Konishi, Makoto Kuwata-Gonokami, Sergey V Garnov, Alexander N Obraztsov, and Yuri P Svirko. Photon-drag-induced terahertz emission from graphene. *Physical Review B*, 90(24):241416, 2014. 47, 48

[91] MV Entin, LI Magarill, and DL Shepelyansky. Theory of resonant photon drag in monolayer graphene. *Physical Review B*, 81(16):165441, 2010. 48

[92] R Kersting, Karl Unterrainer, G Strasser, HF Kauffmann, and E Gornik. Few-cycle thz emission from cold plasma oscillations. *Physical Review Letters*, 79(16):3038, 1997. 48

[93] E Yablonovitch, JP Heritage, DE Aspnes, and Y Yafet. Virtual photoconductivity. *Physical review letters*, 63(9):976, 1989. 48

[94] BB Hu, X-C Zhang, and DH Auston. Terahertz radiation induced by subband-gap femtosecond optical excitation of gaas. *Physical review letters*, 67(19):2709, 1991. 48

[95] AV Kuznetsov and CJ Stanton. Ultrafast optical generation of carriers in a dc electric field: Transient localization and photocurrent. *Physical Review B*, 48(15):10828, 1993. 48

[96] Nakanishi Hidetoshi, Fujiwara Shogo, Takayama Kazuhisa, Kawayama Iwao, Murakami Hironaru, and Tonouchi Masayoshi. Imaging of a polycrystalline silicon solar cell using a laser terahertz emission microscope. *Applied Physics Express*, 5(11):112301, 2012. 48

[97] Yuji Sakai, Iwao Kawayama, Hidetoshi Nakanishi, and Masayoshi Tonouchi. Visualization of gan surface potential using terahertz emission enhanced by local defects. *Scientific Reports*, 5:13860, 2015. 48

[98] Lukas Braun, Gregor Mussler, Andrzej Hruban, Marcin Konczykowski, Thomas Schumann, Martin Wolf, Markus Münzenberg, Luca Perfetti, and Tobias Kampfrath. Ultrafast photocurrents at the surface of the three-dimensional topological insulator bi 2 se 3. *Nature communications*, 7(1):1–9, 2016. 48, 51, 104, 107, 109, 112

[99] Hui Zhao, Eric J Loren, Arthur L Smirl, and HM van Driel. Dynamics of charge currents ballistically injected in gaas by quantum interference. *Journal of Applied Physics*, 103(5):053510, 2008. 50

[100] Ruixiang Fei, Wei Kang, and Li Yang. Ferroelectricity and phase transitions in monolayer group-iv monochalcogenides. *Physical review letters*, 117(9):097601, 2016. 51, 104

[101] Suman Raj Panday and Benjamin M Fregoso. Strong second harmonic generation in two-dimensional ferroelectric iv-monochalcogenides. *Journal of Physics: Condensed Matter*, 29(43):43LT01, 2017. 51, 79

[102] Tonatiuh Rangel, Benjamin M Fregoso, Bernardo S Mendoza, Takahiro Morimoto, Joel E Moore, and Jeffrey B Neaton. Large bulk photovoltaic effect and spontaneous polarization of single-layer monochalcogenides. *Physical review letters*, 119(6):067402, 2017. 51, 79, 103, 111

[103] Yong Wang, Theresa P Ginley, and Stephanie Law. Growth of high-quality bi2se3 topological insulators using (bi1-xinx) 2se3 buffer layers. *Journal of Vacuum Science & Technology B, Nanotechnology and Microelectronics: Materials, Processing, Measurement, and Phenomena*, 36(2):02D101, 2018. 51, 53, 55, 63

[104] Kateryna Kushnir, Kefan Chen, Lite Zhou, Binod Giri, Ronald L Grimm, Pratap M Rao, and Lyubov V Titova. Dynamics of photoexcited carriers in polycrystalline pbs and at pbs/zno heterojunctions: Influence of grain boundaries and interfaces. *The Journal of Physical Chemistry C*, 122(22):11682–11688, 2018. 51, 63, 127

[105] Zhehao Zhu, Satish Kumar Iyemperumal, Kateryna Kushnir, Alexander D Carl, Lite Zhou, Drew R Brodeur, Ronald L Grimm, Lyubov V Titova, N Aaron Deskins, and Pratap M Rao. Enhancing the solar energy conversion efficiency of solution-deposited

bi 2 s 3 thin films by annealing in sulfur vapor at elevated temperature. *Sustainable Energy & Fuels*, 1(10):2134–2144, 2017. 51, 63, 83, 127

[106] Binod Giri, Maryam Masroor, Tao Yan, Kateryna Kushnir, Alexander D Carl, Curtis Doiron, Haochuan Zhang, Yanyan Zhao, Arthur McClelland, Geoffrey A Tompsett, et al. Balancing light absorption and charge transport in vertical sns2 nanoflake photoanodes with stepped layers and large intrinsic mobility. *Advanced Energy Materials*, 9(31):1901236, 2019. 51, 69, 70, 71, 72, 73, 74, 120

[107] Teng Shi, Kateryna Kushnir, Zhengtianye Wang, Stephanie Law, and Lyubov V Titova. Photoexcited free carrier dynamics in bi2se3,(bi0. 75in0. 25) 2se3, and (bi0. 50in0. 50) 2se3: from topological to band insulator. *ACS Photonics*, 7(10):2778–2786, 2020. 51, 54, 55, 56, 58, 59, 61, 64, 65, 66, 127

[108] Joel E Moore. The birth of topological insulators. *Nature*, 464(7286):194–198, 2010. 52

[109] Yuqi Xia, Dong Qian, David Hsieh, L Wray, Arijeet Pal, Hsin Lin, Arun Bansil, DHYS Grauer, Yew San Hor, Robert Joseph Cava, et al. Observation of a large-gap topological-insulator class with a single dirac cone on the surface. *Nature physics*, 5(6):398–402, 2009. 52, 53

[110] Liang Wu, M Brahlek, R Valdés Aguilar, AV Stier, CM Morris, Y Lubashevsky, LS Bilbro, N Bansal, Seongshik Oh, and NP Armitage. A sudden collapse in the transport lifetime across the topological phase transition in (bi 1- x in x) 2 se 3. *Nature Physics*, 9(7):410–414, 2013. 52, 55, 57

[111] Jonathan A Sobota, S-L Yang, Alexander F Kemper, JJ Lee, Felix T Schmitt, Wei Li, Robert G Moore, James G Analytis, Ian R Fisher, Patrick S Kirchmann, et al. Direct optical coupling to an unoccupied dirac surface state in the topological insulator bi 2 se 3. *Physical review letters*, 111(13):136802, 2013. 53

[112] Louis Veyrat, Fabrice Iacovella, Joseph Dufouleur, Christian Nowka, Hannes Funke, Ming Yang, Walter Escoffier, Michel Goiran, Barbara Eichler, Oliver G Schmidt, et al. Band bending inversion in bi2se3 nanostructures. *Nano Letters*, 15(11):7503–7507, 2015. 53

[113] Byung Cheol Park, Tae-Hyeon Kim, Kyung Ik Sim, Boyoun Kang, Jeong Won Kim, Beongki Cho, Kwang-Ho Jeong, Mann-Ho Cho, and Jae Hoon Kim. Terahertz single conductance quantum and topological phase transitions in topological insulator bi 2 se 3 ultrathin films. *Nature communications*, 6(1):1–8, 2015. 53

[114] Jiajun Zhu, Fang Liu, Shengqiang Zhou, C Franke, S Wimmer, VV Volobuev, G Springholz, A Pashkin, H Schneider, and M Helm. Lattice vibrations and electrical transport in (bi1- x in x) 2se3 films. *Applied Physics Letters*, 109(20):202103, 2016. 53

[115] Sangwan Sim, Nikesh Koirala, Matthew Brahlek, Ji Ho Sung, Jun Park, Soonyoung Cha, Moon-Ho Jo, Seongshik Oh, and Hyunyong Choi. Tunable fano quantum-interference dynamics using a topological phase transition in (b i 1- x i n x) 2 s e 3. *Physical Review B*, 91(23):235438, 2015. 53

[116] Nadezda V Tarakina, S Schreyeck, M Luysberg, S Grauer, C Schumacher, G Karczewski, K Brunner, C Gould, H Buhmann, RE Dunin-Borkowski, et al. Suppressing twin formation in bi2se3 thin films. *Advanced materials interfaces*, 1(5):1400134, 2014. 55

[117] Sangwan Sim, Matthew Brahlek, Nikesh Koirala, Soonyoung Cha, Seongshik Oh, and Hyunyong Choi. Ultrafast terahertz dynamics of hot dirac-electron surface scattering in the topological insulator bi 2 se 3. *Physical Review B*, 89(16):165137, 2014. 55

[118] Hadas Soifer, Alexandre Gauthier, Alexander F Kemper, Costel R Rotundu, S-L Yang, Hongyu Xiong, Donghui Lu, Makoto Hashimoto, Patrick S Kirchmann, Jonathan A

Sobota, et al. Band-resolved imaging of photocurrent in a topological insulator. *Physical review letters*, 122(16):167401, 2019. 58

[119] SG Patil and RH Tredgold. Electrical and photoconductive properties of sns2 crystals. *Journal of Physics D: Applied Physics*, 4(5):718, 1971. 68

[120] B Thangaraju and P Kaliannan. Spray pyrolytic deposition and characterization of sns and sns2 thin films. *Journal of Physics D: Applied Physics*, 33(9):1054, 2000. 68

[121] Aamir Shafique, Abdus Samad, and Young-Han Shin. Ultra low lattice thermal conductivity and high carrier mobility of monolayer sns 2 and snse 2: a first principles study. *Physical Chemistry Chemical Physics*, 19(31):20677–20683, 2017. 68

[122] Lee A Burton, Thomas J Whittles, David Hesp, Wojciech M Linhart, Jonathan M Skelton, Bo Hou, Richard F Webster, Graeme O'Dowd, Christian Reece, David Cherns, et al. Electronic and optical properties of single crystal sns 2: an earth-abundant disulfide photocatalyst. *Journal of Materials Chemistry A*, 4(4):1312–1318, 2016. 68

[123] Jiangtian Li and Nianqiang Wu. Semiconductor-based photocatalysts and photoelectrochemical cells for solar fuel generation: a review. *Catalysis Science & Technology*, 5(3):1360–1384, 2015. 69

[124] A Voznyi, V Kosyak, A Opanasyuk, N Tirkusova, L Grase, A Medvids, and G Mezinskis. Structural and electrical properties of sns2 thin films. *Materials Chemistry and Physics*, 173:52–61, 2016. 69

[125] Joseph M Gonzalez and Ivan I Oleynik. Layer-dependent properties of sns 2 and snse 2 two-dimensional materials. *Physical Review B*, 94(12):125443, 2016. 75

[126] W Albers, C Haas, HJ Vink, and JD Wasscher. Investigations on sns. *Journal of Applied Physics*, 32(10):2220–2225, 1961. 78

[127] H Wiedemeier and PA Siemers. The thermal expansion of ges and gete. *Zeitschrift für anorganische und allgemeine Chemie*, 431(1):299–304, 1977. 78

[128] T Grandke and L Ley. Angular-resolved uv photoemission and the band structure of ges. *Physical Review B*, 16(2):832, 1977. 78

[129] Lidia C Gomes, A Carvalho, and AH Castro Neto. Enhanced piezoelectricity and modified dielectric screening of two-dimensional group-iv monochalcogenides. *Physical Review B*, 92(21):214103, 2015. 78

[130] L Makinistian and EA Albanesi. First-principles calculations of the band gap and optical properties of germanium sulfide. *Physical Review B*, 74(4):045206, 2006. 78, 103

[131] Ruixiang Fei, Wenbin Li, Ju Li, and Li Yang. Giant piezoelectricity of monolayer group iv monochalcogenides: Snse, sns, gese, and ges. *Applied Physics Letters*, 107(17):173104, 2015. 78

[132] Hua Wang and Xiaofeng Qian. Two-dimensional multiferroics in monolayer group iv monochalcogenides. *2D Materials*, 4(1):015042, 2017. 78

[133] AS Rodin, Lidia C Gomes, Alexandra Carvalho, and AH Castro Neto. Valley physics in tin (ii) sulfide. *Physical Review B*, 93(4):045431, 2016. 78

[134] Blair R Tuttle, Saeed M Alhassan, and Sokrates T Pantelides. Large excitonic effects in group-iv sulfide monolayers. *Physical Review B*, 92(23):235405, 2015. 78

[135] Feng Li, Xiuhong Liu, Yu Wang, and Yafei Li. Germanium monosulfide monolayer: a novel two-dimensional semiconductor with a high carrier mobility. *Journal of Materials Chemistry C*, 4(11):2155–2159, 2016. 79, 80

[136] Hua Wang and Xiaofeng Qian. Giant optical second harmonic generation in two-dimensional multiferroics. *Nano letters*, 17(8):5027–5034, 2017. 79

[137] Mehrshad Mehboudi, Benjamin M Fregoso, Yurong Yang, Wenjuan Zhu, Arend Van Der Zande, Jaime Ferrer, L Bellaiche, Pradeep Kumar, and Salvador Barraza-Lopez. Structural phase transition and material properties of few-layer monochalcogenides. *Physical review letters*, 117(24):246802, 2016. 79

[138] Benjamin M. Fregoso, Takahiro Morimoto, and Joel E. Moore. Quantitative relationship between polarization differences and the zone-averaged shift photocurrent. *Physical Review B*, 96(7):075421, 2017. PRB. 79, 103

[139] Kristie J Koski, Judy J Cha, Bryan W Reed, Colin D Wessells, Desheng Kong, and Yi Cui. High-density chemical intercalation of zero-valent copper into bi2se3 nanoribbons. *Journal of the American Chemical Society*, 134(18):7584–7587, 2012. 79

[140] Asif Ali Tahir, Muhammad Ali Ehsan, Muhammad Mazhar, KG Upul Wijayantha, Matthias Zeller, and AD Hunter. Photoelectrochemical and photoresponsive properties of bi2s3 nanotube and nanoparticle thin films. *Chemistry of Materials*, 22(17):5084–5092, 2010. 82

[141] Qingyi Zeng, Jing Bai, Jinhua Li, Yunpo Li, Xuejin Li, and Baoxue Zhou. Combined nanostructured bi2s3/tna photoanode and pt/sipvc photocathode for efficient self-biasing photoelectrochemical hydrogen and electricity generation. *Nano Energy*, 9:152–160, 2014. 82

[142] Donglin Guo, Chenguo Hu, and Cuiling Zhang. First-principles study on doping and temperature dependence of thermoelectric property of bi2s3 thermoelectric material. *Materials Research Bulletin*, 48(5):1984–1988, 2013. 86

[143] Lyubov V Titova, Tyler L Cocker, Xiongyao Wang, Al Meldrum, and Frank A Hegmann. Ultrafast carrier dynamics in silicon nanocrystal films. *ECS Transactions*, 45(5):21, 2012. 86

[144] Riley E Brandt, Vladan Stevanović, David S Ginley, and Tonio Buonassisi. Identifying defect-tolerant semiconductors with high minority-carrier lifetimes: beyond hybrid lead halide perovskites. *Mrs Communications*, 5(2):265–275, 2015. 87

[145] Kateryna Kushnir, Kefan Chen, Lite Zhou, Binod Giri, Ronald L. Grimm, Pratap M. Rao, and Lyubov V. Titova. Dynamics of photoexcited carriers in polycrystalline pbs and at pbs/zno heterojunctions: Influence of grain boundaries and interfaces. *The Journal of Physical Chemistry C*, 122(22):11682–11688, 2018. 88

[146] Ronen Gertman, Anna Osherov, Yuval Golan, and Iris Visoly-Fisher. Chemical bath deposited pbs thin films on zno nanowires for photovoltaic applications. *Thin solid films*, 550:149–155, 2014. 89

[147] Samim Sardar, Prasenjit Kar, Soumik Sarkar, Peter Lemmens, and SK Pal. Interfacial carrier dynamics in pbs-zno light harvesting assemblies and their potential implication in photovoltaic/photocatalysis application. *Solar Energy Materials and Solar Cells*, 134:400–406, 2015. 89

[148] Patrick R Brown, Richard R Lunt, Ni Zhao, Timothy P Osedach, Darcy D Wanger, Liang-Yi Chang, Moungi G Bawendi, and Vladimir Bulovic. Improved current extraction from zno/pbs quantum dot heterojunction photovoltaics using a moo3 interfacial layer. *Nano letters*, 11(7):2955–2961, 2011. 89

[149] JJH Pijpers, R Ulbricht, KJ Tielrooij, A Osherov, Y Golan, C Delerue, G Allan, and M Bonn. Assessment of carrier-multiplication efficiency in bulk pbse and pbs. *Nature Physics*, 5(11):811–814, 2009. 89

[150] Y Cheng, MDC Whitaker, R Makkia, S Cocklin, VR Whiteside, LA Bumm, E Adcock-Smith, KP Roberts, P Hari, and IR Sellers. Role of defects and surface states in the carrier transport and nonlinearity of the diode characteristics in pbs/zno quantum dot solar cells. *ACS applied materials & interfaces*, 9(15):13269–13277, 2017. 89

[151] Zhi Zheng, Lin Gan, Jianbing Zhang, Fuwei Zhuge, and Tianyou Zhai. An enhanced uv–vis–nir an d flexible photodetector based on electrospun zno nanowire array/pbs quantum dots film heterostructure. *Advanced Science*, 4(3):1600316, 2017. 89

[152] Gregory D Scholes and Garry Rumbles. Excitons in nanoscale systems: fundamentals and applications. *Annual ReView of nano research*, pages 103–157, 2008. 89

[153] Aaron G Midgett, Joseph M Luther, John T Stewart, Danielle K Smith, Lazaro A Padilha, Victor I Klimov, Arthur J Nozik, and Matthew C Beard. Size and composition dependent multiple exciton generation efficiency in pbs, pbse, and pbs x se1–x alloyed quantum dots. *Nano letters*, 13(7):3078–3085, 2013. 89

[154] John T Stewart, Lazaro A Padilha, M Mumtaz Qazilbash, Jeffrey M Pietryga, Aaron G Midgett, Joseph M Luther, Matthew C Beard, Arthur J Nozik, and Victor I Klimov. Comparison of carrier multiplication yields in pbs and pbse nanocrystals: the role of competing energy-loss processes. *Nano letters*, 12(2):622–628, 2012. 89

[155] Y Wang, A Suna, W Mahler, and R Kasowski. Pbs in polymers. from molecules to bulk solids. *The Journal of chemical physics*, 87(12):7315–7322, 1987. 89

[156] Structural Seghaier, N Kamoun, R Brini, and AB Amara. Structural and optical properties of pbs thin films deposited by chemical bath deposition. *Materials Chemistry and Physics*, 97(1):71–80, 2006. 90

[157] Matt Law, Lori E Greene, Justin C Johnson, Richard Saykally, and Peidong Yang. Nanowire dye-sensitized solar cells. *Nature materials*, 4(6):455–459, 2005. 90

[158] E Yablonovitch and TJ Gmitter. A contactless minority lifetime probe of heterostructures, surfaces, interfaces and bulk wafers. *Solid-state electronics*, 35(3):261–267, 1992. 92

[159] Svein Espevik, Chen-ho Wu, and Richard H Bube. Mechanism of photoconductivity in chemically deposited lead sulfide layers. *Journal of applied physics*, 42(9):3513–3529, 1971. 93, 95

[160] Robert S Allgaier and Wayne W Scanlon. Mobility of electrons and holes in pbs, pbse, and pbte between room temperature and 4.2 k. *Physical Review*, 111(4):1029, 1958. 97

[161] Jie Sun, Yuanzhi Li, Yi Yang, Jilin Bai, and Xiujian Zhao. Effect of the interface on uv-vis-ir photodetection performance of pbs/zno nanocomposite photocatalysts. *Applied Surface Science*, 358:498–505, 2015. 99

[162] Bruno Ehrler, Kevin P Musselman, Marcus L Bohm, Frederik SF Morgenstern, Yana Vaynzof, Brian J Walker, Judith L MacManus-Driscoll, and Neil C Greenham. Preventing interfacial recombination in colloidal quantum dot solar cells by doping the metal oxide. *Acs Nano*, 7(5):4210–4220, 2013. 99

[163] Xiaoliang Zhang and Erik MJ Johansson. Reduction of charge recombination in pbs colloidal quantum dot solar cells at the quantum dot/zno interface by inserting a mgzno buffer layer. *Journal of Materials Chemistry A*, 5(1):303–310, 2017. 101

[164] Alexander H Ip, Susanna M Thon, Sjoerd Hoogland, Oleksandr Voznyy, David Zhitomirsky, Ratan Debnath, Larissa Levina, Lisa R Rollny, Graham H Carey, Armin Fischer, et al. Hybrid passivated colloidal quantum dot solids. *Nature nanotechnology*, 7(9):577–582, 2012. 101

[165] Gi-Hwan Kim, F Pelayo Garcia de Arquer, Yung Jin Yoon, Xinzheng Lan, Mengxia Liu, Oleksandr Voznyy, Zhenyu Yang, Fengjia Fan, Alexander H Ip, Pongsakorn Kanjanaboos, et al. High-efficiency colloidal quantum dot photovoltaics via robust self-assembled monolayers. *Nano letters*, 15(11):7691–7696, 2015. 101

[166] Keith T Butler, Jarvist M Frost, and Aron Walsh. Ferroelectric materials for solar

energy conversion: photoferroics revisited. *Energy & Environmental Science*, 8(3):838–848, 2015. 103

[167] Steve M Young and Andrew M Rappe. First principles calculation of the shift current photovoltaic effect in ferroelectrics. *Physical review letters*, 109(11):116601, 2012. 103

[168] Liang Z Tan, Fan Zheng, Steve M Young, Fenggong Wang, Shi Liu, and Andrew M Rappe. Shift current bulk photovoltaic effect in polar materials—hybrid and oxide perovskites and beyond. *Npj Computational Materials*, 2(1):1–12, 2016. 103

[169] Fenggong Wang, Ilya Grinberg, Lai Jiang, Steve M Young, Peter K Davies, and Andrew M Rappe. Materials design of visible-light ferroelectric photovoltaics from first principles. *Ferroelectrics*, 483(1):1–12, 2015. 103

[170] Lyubov V Titova, Benjamin M Fregoso, and Ronald L Grimm. Group-iv monochalcogenides ges, gese, sns, snse. In *Chalcogenide*, pages 119–151. Elsevier, 2020. 103

[171] Ruixiang Fei, Wenbin Li, Ju Li, and Li Yang. Giant piezoelectricity of monolayer group iv monochalcogenides: Snse, sns, gese, and ges. 107(17):173104, 2015. 104

[172] Ehren M Mannebach, Karel-Alexander N Duerloo, Lenson A Pellouchoud, Meng-Ju Sher, Sanghee Nah, Yi-Hong Kuo, Yifei Yu, Ann F Marshall, Linyou Cao, Evan J Reed, et al. Ultrafast electronic and structural response of monolayer mos2 under intense photoexcitation conditions. *ACS nano*, 8(10):10734–10742, 2014. 124

[173] Thomas Dekorsy, Holger Auer, Christian Waschke, Huib J Bakker, Hartmut G Roskos, Heinrich Kurz, Veit Wagner, and Peter Grosse. Emission of submillimeter electromagnetic waves by coherent phonons. *Physical review letters*, 74(5):738, 1995. 125

[174] Thomas Dekorsy, Holger Auer, Huib J Bakker, Hartmut G Roskos, and Heinrich Kurz. Thz electromagnetic emission by coherent infrared-active phonons. *Physical Review B*, 53(7):4005, 1996. 125

[175] Federico Brivio, Jarvist M Frost, Jonathan M Skelton, Adam J Jackson, Oliver J Weber, Mark T Weller, Alejandro R Goni, Aurélien MA Leguy, Piers RF Barnes, and Aron Walsh. Lattice dynamics and vibrational spectra of the orthorhombic, tetragonal, and cubic phases of methylammonium lead iodide. *Physical Review B*, 92(14):144308, 2015. 125

[176] Muneaki Hase, Masayuki Katsuragawa, Anca Monia Constantinescu, and Hrvoje Petek. Coherent phonon-induced optical modulation in semiconductors at terahertz frequencies. *New Journal of Physics*, 15(5):055018, 2013. 125

[177] YM Chang, L Xu, and HWK Tom. Observation of coherent surface optical phonon oscillations by time-resolved surface second-harmonic generation. *Physical review letters*, 78(24):4649, 1997. 125

[178] GC Cho, W Kutt, and H Kurz. Subpicosecond time-resolved coherent-phonon oscillations in gaas. *Physical review letters*, 65(6):764, 1990. 125

[179] Anton Y Bykov, Tatiana V Murzina, Nicolas Olivier, Gregory A Wurtz, and Anatoly V Zayats. Coherent lattice dynamics in topological insulator bi 2 te 3 probed with time-resolved optical second-harmonic generation. *Physical Review B*, 92(6):064305, 2015. 125

[180] Ashley M. Cook, Benjamin M Fregoso, Fernando de Juan, Sinisa Coh, and Joel E. Moore. Design principles for shift current photovoltaics. *Nature communications*, 8:14176–14176, 2017. 28120823[pmid] PMC5288499[pmcid] ncomms14176[PII] Nat Commun. 126

[181] Ruixiang Fei, Wei Kang, and Li Yang. Ferroelectricity and phase transitions in monolayer group-iv monochalcogenides. *Physical Review Letters*, 117(9):097601, 2016. PRL. 126

[182] Suman Raj Panday and Benjamin M. Fregoso. Strong second harmonic generation in two-dimensional ferroelectric iv-monochalcogenides. *Journal of Physics: Condensed Matter*, 29(43):43LT01, 2017. 126

[183] Tonatiuh Rangel, Benjamin M. Fregoso, Bernardo S. Mendoza, Takahiro Morimoto, Joel E. Moore, and Jeffrey B. Neaton. Large bulk photovoltaic effect and spontaneous polarization of single-layer monochalcogenides. *Physical Review Letters*, 119(6):067402, 2017. PRL. 126

[184] Laura Sharp, David Soltz, and B. A. Parkinson. Growth and characterization of tin disulfide single crystals. *Crystal Growth and Design*, 6(6):1523–1527, 2006. 126

[185] Lukas Braun, Gregor Mussler, Andrzej Hruban, Marcin Konczykowski, Thomas Schumann, Martin Wolf, Markus Münzenberg, Luca Perfetti, and Tobias Kampfrath. Ultrafast photocurrents at the surface of the three-dimensional topological insulator bi2se3. *Nature Communications*, 7:13259, 2016. 126

[186] Binod Giri, Maryam Masroor, Tao Yan, Kateryna Kushnir, Alexander D. Carl, Curtis Doiron, Haochuan Zhang, Yanyan Zhao, Arthur McClelland, Geoffrey A. Tompsett, Dunwei Wang, Ronald L. Grimm, Lyubov V. Titova, and Pratap M. Rao. Balancing light absorption and charge transport in vertical sns2 nanoflake photoanodes with stepped layers and large intrinsic mobility. 9(31):1901236, 2019. 127

[187] Guangjiang Li, Kateryna Kushnir, Yongchang Dong, Sergii Chertopalov, Apparao M Rao, Vadym N Mochalin, Ramakrishna Podila, and Lyubov V Titova. Equilibrium and non-equilibrium free carrier dynamics in 2d ti3c2tx mxenes: Thz spectroscopy study. *2D Materials*, 5(3):035043, 2018. 128

[188] DO Oyewole, OK Oyewole, K Kushnir, T Shi, OV Oyelade, SA Adeniji, B Agyei-Tuffour, K Evans-Lutterodt, LV Titova, and WO Soboyejo. Pressure and thermal

annealing effects on the photoconversion efficiency of polymer solar cells. *AIP Advances*, 11(4):045304, 2021. 128

Appendix A

Code to analyze THz-TDS data, thin film approximation

The following Matlab code is used to calculate the basic parameters such as refractive index and absorption coefficient as well as intrinsic conductivity of the material. In this code you need to input reference waveform and sample waveform. Here shown a data obtained for Si wafer, which could also be used as your reference point.

```
clc; clear; close;

%Parameters for your data (physical):
        %Thickness of sample 1 should be thicker sample
                thickness = 0.1;                                %(millimeters)


%Parameters for your data (technical):
%Where your files are (relative or absolute addresses are fine)
                defaultPath = '../Raw Data/';

%The spacing character used in the file to separate entries
                fileDelimiter = ',';                    %(default is tab, \t )

%The columns in the file that have each set of information
                colTime = 1;                                    %time in picoseconds
                colData = 2;                                    %signed E field



%Open file selection boxes (sample&substrate)
try
        if ~isempty(successfulLoad) && successfulLoad && ~askForFiles
                getFiles = false;
        else
                getFiles = true;
        end
catch
        getFiles = true;
end
if getFiles
        successfulLoad = false;
        clc;
        fprintf('wf_substrate file');
        [dataC1Name, dataC1Path] = uigetfile('*','Select the file with your substrate data\n'
,defaultPath);
        clc;
        fprintf('wf_sample file ');
        [dataC2Name, dataC2Path] = uigetfile('*','Select the file with your sample data\n',de
faultPath);
        %throwing error
    if isequal(dataC1Name,0) || isequal(dataC1Path, 0) ||...
                        isequal(dataC1Name, '') || isequal(dataC1Path, '') ||...
                        isequal(dataC2Name,0) || isequal(dataC2Path, 0) ||...
                        isequal(dataC2Name, '') || isequal(dataC2Path, '')
                clear dataC1Name dataC2Name dataC1Path dataC2Path;
                clc;
                error('File selection failed. Are you sure you selected both files?');
        else
                clc;
                fprintf('Opening ''%s''\n   and ''%s''\n',dataC1Name,dataC2Name);
                successfulLoad = true;
        end
else
        clc;
```

```
        fprintf('Using ''%s''\n  and ''%s''\n',dataC1Name,dataC2Name);
end
clear askForFiles;

%Read the selected file and extract pertinent data
rawS1Data = dlmread(strcat(dataC1Path,dataC1Name),fileDelimiter);
rawS2Data = dlmread(strcat(dataC2Path,dataC2Name),fileDelimiter);
T1 = rawS1Data( :, colTime);
T2 = rawS2Data( :, colTime);
E1 = rawS1Data( :, colData);
E2 = rawS2Data( :, colData);
clear colTime colData


%Plot waveform S1 and S2 the electric field versus time graphs
try
        figure(fig1)
        hold off
catch
        fig1 = figure('Name','E Field versus Time');
end
plot(T1.*0.05,E1,'Color',[0,0,1])
hold on
plot(T2*0.05,E2,'Color',[1,0,0])
xlabel('Time (ps)')
ylabel('Electric Field (arb. units)')
title('Electric Field versus Time, for S1 and S2')
legend('E_{ref}','E_{sample}')
fprintf('''Figure 1: Electric Field versus Time'' has been rendered.\n');
drawnow;

%FFT
dt = 0.05; % Step in ps ( is 50fs topticas resolution)
%N_add1 = 2*length(T_S1);   %zero based, add more 0, which doesn't change the signal but mean
s a lot for phase
N_add1 = 0;
N1 = 600+N_add1;  % Length of signal sample1
S1_fft = fft(E1,N1)/N1;
dw1 = 1/(dt*N1);%step of frequency in THz
w_max1 = dw1*(N1-2); %max freq range
w1 = 0:dw1:w_max1/2;
E1_fft = abs(S1_fft(1:N1/2));

%N_add2 = 2*length(T_S2);   %zero based, add more 0, which doesn't change the signal but mean
s a lot for phase
N_add2 = 0;
N2 = 600+N_add2;  % Length of signal sample2
S2_fft = fft(E2,N2)/N2;
dw2 = 1/(dt*N2);%step of frequency in THz
w_max2 = dw2*(N2-2); %max freq range
w2 = 0:dw2:w_max2/2;
E2_fft = abs(S2_fft(1:N2/2));


try
        figure(fig2)
        hold off
```

```
catch
        fig2 = figure('Name','FFT E Field versus Frequency');
end
plot(w1(1:200),E1_fft(1:200),'Color',[0,0,1])
hold on
plot(w2(1:200),E2_fft(1:200),'Color',[1,0,0])
xlabel('Frequency (THz)')
ylabel('FFT Electric Field (au)')
title('FFT Electric Field versus Frequency, for S1 and S2')
legend('subsrtate','sample')
fprintf('''Figure 2: FFT Electric Field versus Frequency'' has been rendered.\n');
drawnow;

%Phase unwrapping
phs1 = angle(S1_fft(1:N1/2));
phs2 = angle(S2_fft(1:N2/2));


try
        figure(fig3)
        hold off
catch
        fig3 = figure('Name','Phase versus Frequency');
end
plot(w1(1:200),phs1(1:200),'Color',[0,0,1])
hold on
plot(w2(1:200),phs2(1:200),'Color',[1,0,0])
xlabel('Frequency (THz)')
ylabel('Phase (au)')
title('Phase versus Frequency, for subsrtate and sample')
legend('subsrtate','sample')
fprintf('''Figure 3: Phase versus Frequency'' has been rendered.\n');
drawnow;


%phs1_unwr = unwrap(angle(S1_fft(1:N1/2+1))); % default tolerance is pi. Ref: help unwrap
%phs2_unwr = unwrap(angle(S2_fft(1:N2/2+1)));

% default tolerance. Ref: help unwrap
tol = pi;
phs1_unwr = unwrap(angle(S1_fft(1:N1/2)),tol);
phs2_unwr = unwrap(angle(S2_fft(1:N2/2)),tol);


try
        figure(fig4)
        hold off
catch
        fig4 = figure('Name','Phase versus Frequency');
end
plot(w1(1:200),phs1_unwr(1:200),'Color',[0,0,1])
hold on
plot(w2(1:200),phs2_unwr(1:200),'Color',[1,0,0])
xlabel('Frequency (THz)')
ylabel('Unwrapped Phase (au)')
title('Unwrapped Phase versus Frequency, for S1 and S2')
legend('subsrtate','sample')
```

```
fprintf('''Figure 4: Unwrapped Phase versus Frequency'' has been rendered.\n');
drawnow;

%************************************************************************
w = 8; %max phase which gives readable data!!!
%************************************************************************
%************************************************************************
%           Mira Naftaly method
%************************************************************************
k = 5;
p1 = phs1_unwr;
p2 = phs2_unwr;
% Replace the first 20 elements with 'NaN':
p1(1:k) = NaN;
p2(1:k) = NaN;
% Create empty elements for the 'NaN' elements:
p1(isnan(p1)) = [];
p2(isnan(p2)) = [];
% Extrapolate to fill the empty elements:
p1_extrap = interp1(p1, -(k-1):0, 'linear', 'extrap');
p2_extrap = interp1(p2, -(k-1):0, 'linear', 'extrap');

Phs1_extrap = phs1_unwr;
Phs1_extrap(1:k) = p1_extrap;

Phs2_extrap = phs2_unwr;
Phs2_extrap(1:k) = p2_extrap;

Phs1_f = Phs1_extrap - Phs1_extrap(1);
Phs2_f = Phs2_extrap - Phs2_extrap(1);
try
        figure(fig7)
        hold off
catch
        fig7 = figure('Name','Phase extrapolated with shift versus Frequency');
end
plot(w1,Phs1_f(1:length(w1),1),'Color',[0,0,1])
hold on
plot(w1,Phs2_f(1:length(w1),1),'Color',[1,0,0])
xlabel('Frequency (THz)')
ylabel('Unwrapped Phase extrapolated with shift(au)')
title('Unwrapped Phase extrapolatedwith shift versus Frequency, for S1 and S2')
legend('S1','S2')
fprintf('''Figure 7: Unwrapped Phase Fit extrapolated with shift versus Frequency'' has been
rendered.\n');
drawnow;

%************************************************************************
%
%Now we will calculate N=n+ik and alpha
%
%************************************************************************

c = 0.299792458; %speed of light in mm/ps
d = thickness; %thickness difference in mm
n_0 = 1; %refractive index of substrate
%phase = abs(Phs1_f- Phs2_f).';
```

```
phase = abs(phs1_unwr - phs2_unwr).';
N = c./(2*pi*w1*d).* phase + n_0;
Alpha = -2/d .* log((N.'+n_0).^2/4./N.'.*abs(E2_fft) ./abs(E1_fft));

try
        figure(fig8)
        hold off
catch
        fig8 = figure('Name','Refractive index versus Frequency');
end
plot(w1,N,'Color',[0,0,1])
xlabel('Frequency (THz)')
ylabel('n, refractive index')
%title('Refractive index versus Frequency')
legend('Silicon')
fprintf('''Figure 8: Refractive index versus Frequency'' has been rendered.\n');
drawnow;


try
        figure(fig9)
        hold off
catch
        fig9 = figure('Name','Absorption versus Frequency');
end
plot(w1,Alpha,'Color',[1,0,0])
xlabel('Frequency (THz)')
ylabel('Absorption')
title('Absorption versus Frequency, cm^{-1}')
legend('material')
fprintf('''Figure 9: Absorption versus Frequency'' has been rendered.\n');
drawnow;

%%%%%%%%%%%%%%%%%%%%%%%%%%%%%%%%%%%%%%%%%%%%%%%%%%%%%%%%%%%%%%%%%%%%%%%%%%%%%%%
%Conductivity UNITS keep in mind!!!
%%%%%%%%%%%%%%%%%%%%%%%%%%%%%%%%%%%%%%%%%%%%%%%%%%%%%%%%%%%%%%%%%%%%%%%%%%%%%%%
eps0 = 8.85* 10^(-2); %pico F/cm
Sigma1 = eps0*Alpha.'.*N.*c;
Sigma2 = eps0*2*pi*w1.*(1 - N.^2- (c*Alpha.'./(4*pi*w1)).^2);

try
        figure(fig10)
        hold off
catch
        fig10 = figure('Name','Conductivity');
end
plot(w1(1:100),Sigma1(1:100),'Color',[0,0,1])
hold on
plot(w2(1:100),Sigma2(1:100),'Color',[1,0,0])
xlabel('Frequency (THz)')
ylabel('Conductance (1/Ohm cm)')
title('Conductivity versus Frequency')
legend('sigma1','sigma2')
fprintf('''Figure 10: Conductivity versus Frequency'' has been rendered.\n');
drawnow;

%%%%%%%%%%%%%%%%%%%%%%%%%%%%%%%%%%%%%%%%%%%%%%%%%%%%%%%%%%%%%%%%%%%%%%%%%%%%%%%
```

```
%saving data in a file
%%%%%%%%%%%%%%%%%%%%%%%%%%%%%%%%%%%%%%%%%%%%%%%%%%%%%%%%%%%%%%%%%%%%%%%%%%%%%%%%
%N_tab = table(w1(1:length(w1),1),N);
%Alpha_tab = table(w1(1:length(w1),1),Alpha(1:length(w1)));
%match = '\d+uL';
%fName = regexp(dataC2Name,match,'match');
%writetable(Alpha_tab,fName{1});
%writetable(N_tab,fName{1});
%writetable(Alpha_tab);
%writetable(N_tab);

%fprint(fName,w1,Sigma1,Sigma2)
%Omega = w1';
%s1 = Sigma1';
%s2 = Sigma2';
```

```
wf_substrate filewf_sample file Opening 'wf_air.csv'
   and 'wf_Si.csv'
'Figure 1: Electric Field versus Time' has been rendered.
'Figure 2: FFT Electric Field versus Frequency' has been rendered.
'Figure 3: Phase versus Frequency' has been rendered.
'Figure 4: Unwrapped Phase versus Frequency' has been rendered.
'Figure 7: Unwrapped Phase Fit extrapolated with shift versus Frequency' has been rendered.
'Figure 8: Refractive index versus Frequency' has been rendered.
'Figure 9: Absorption versus Frequency' has been rendered.
'Figure 10: Conductivity versus Frequency' has been rendered.
```

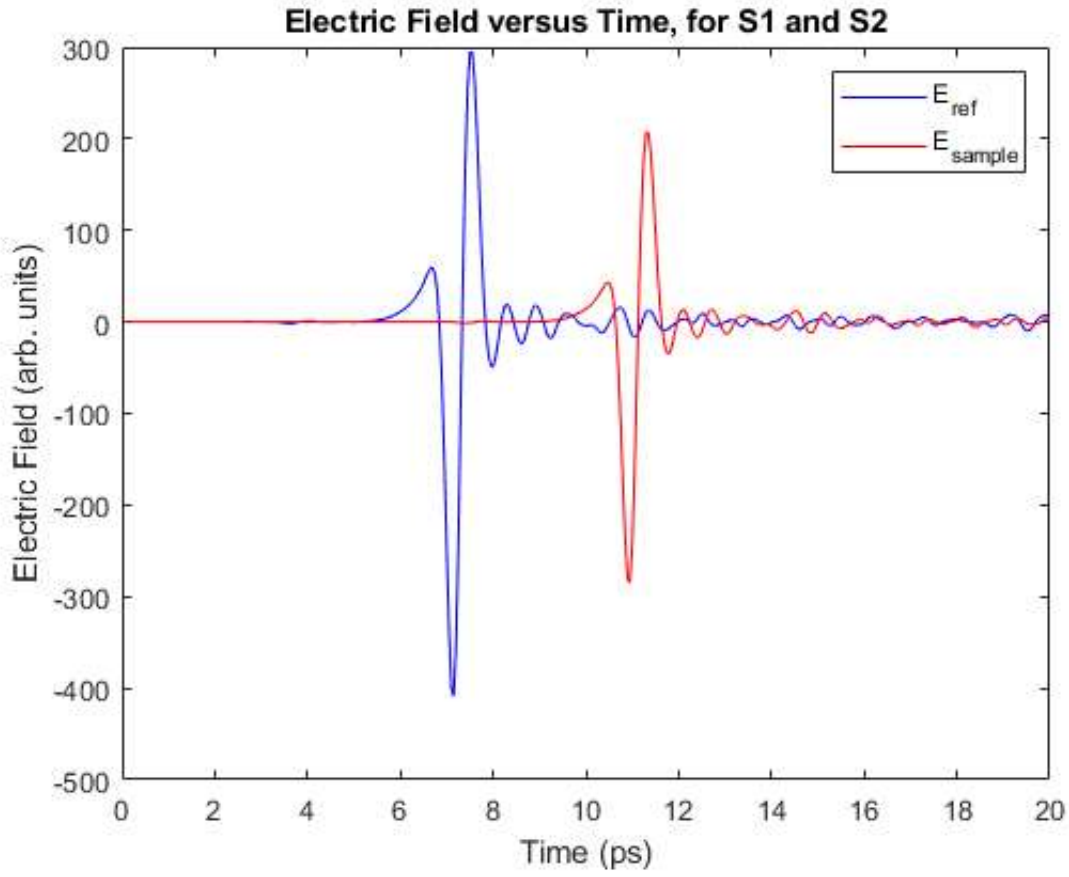

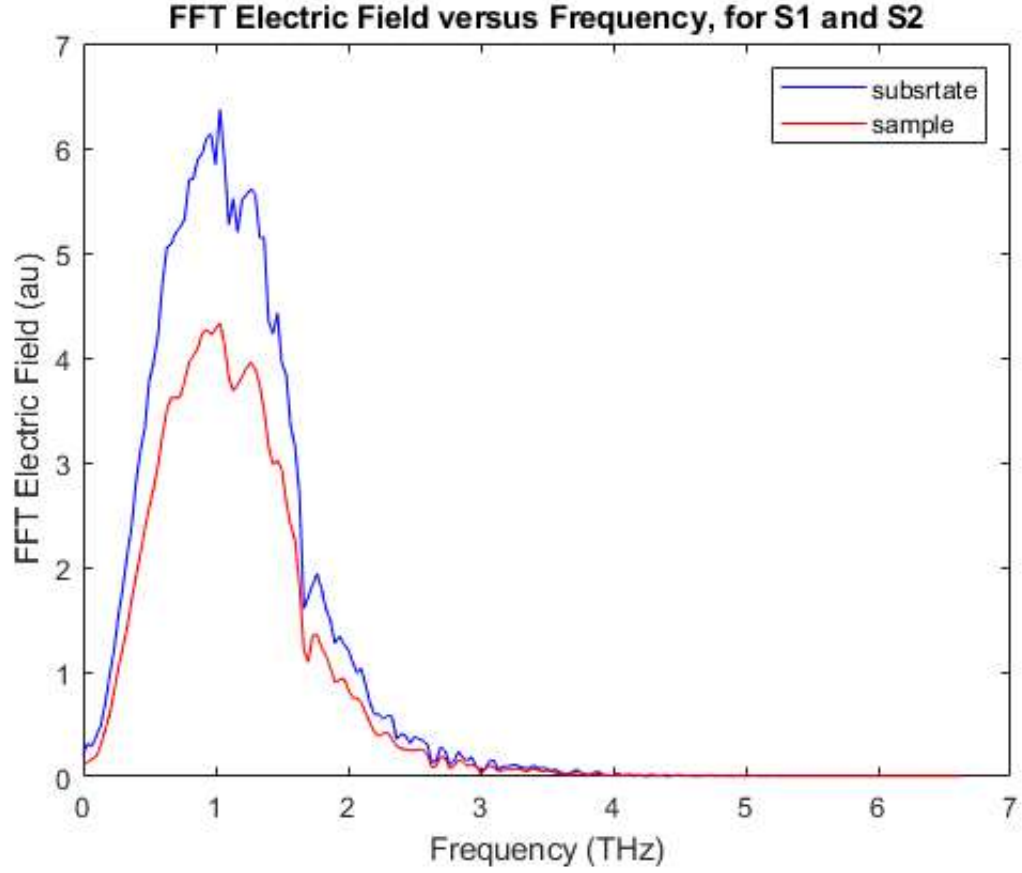
FFT Electric Field versus Frequency, for S1 and S2
subsrtate
sample
FFT Electric Field (au)
Frequency (THz)
0
1
2
3
4
5
6
7

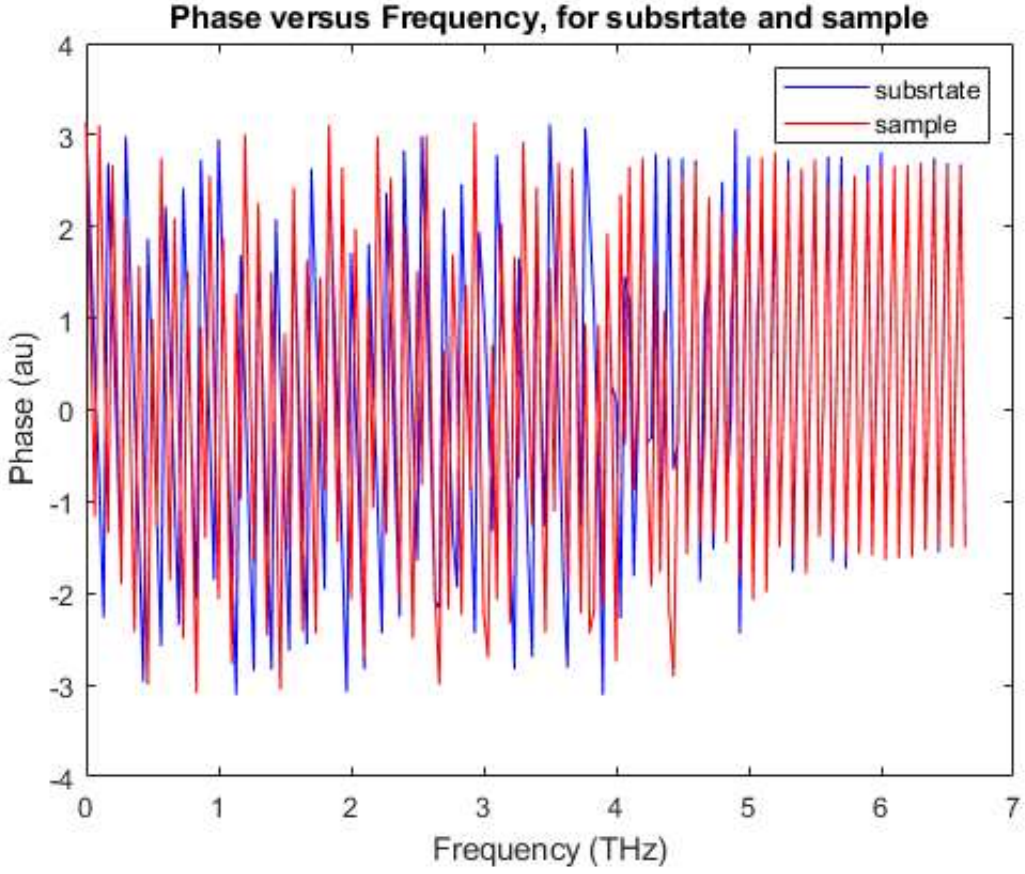
Phase versus Frequency, for subsrtate and sample
subsrtate
sample
Phase (au)
Frequency (THz)
-4
-3
-2
-1
0
1
2
3
4
0
1
2
3
4
5
6
7

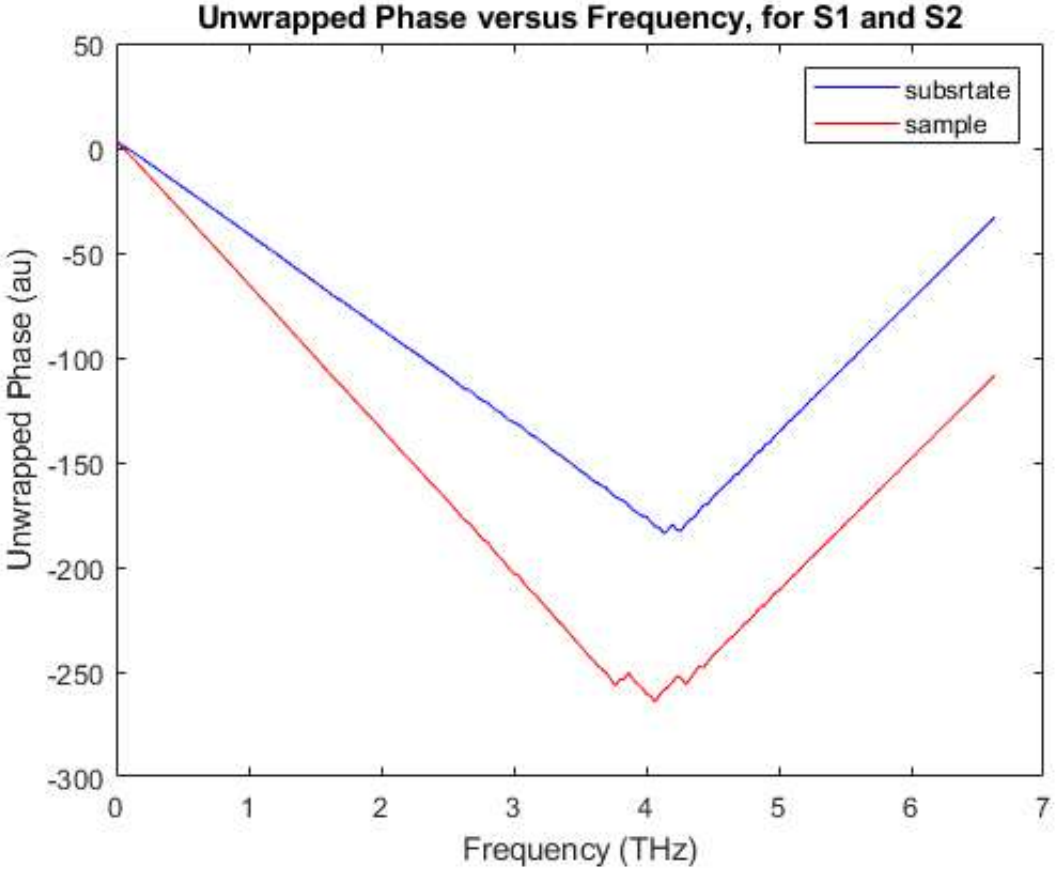
Unwrapped Phase versus Frequency, for S1 and S2
subsrtate
sample
Unwrapped Phase (au)
Frequency (THz)
50
0
-50
-100
-150
-200
-250
-300
0
1
2
3
4
5
6
7

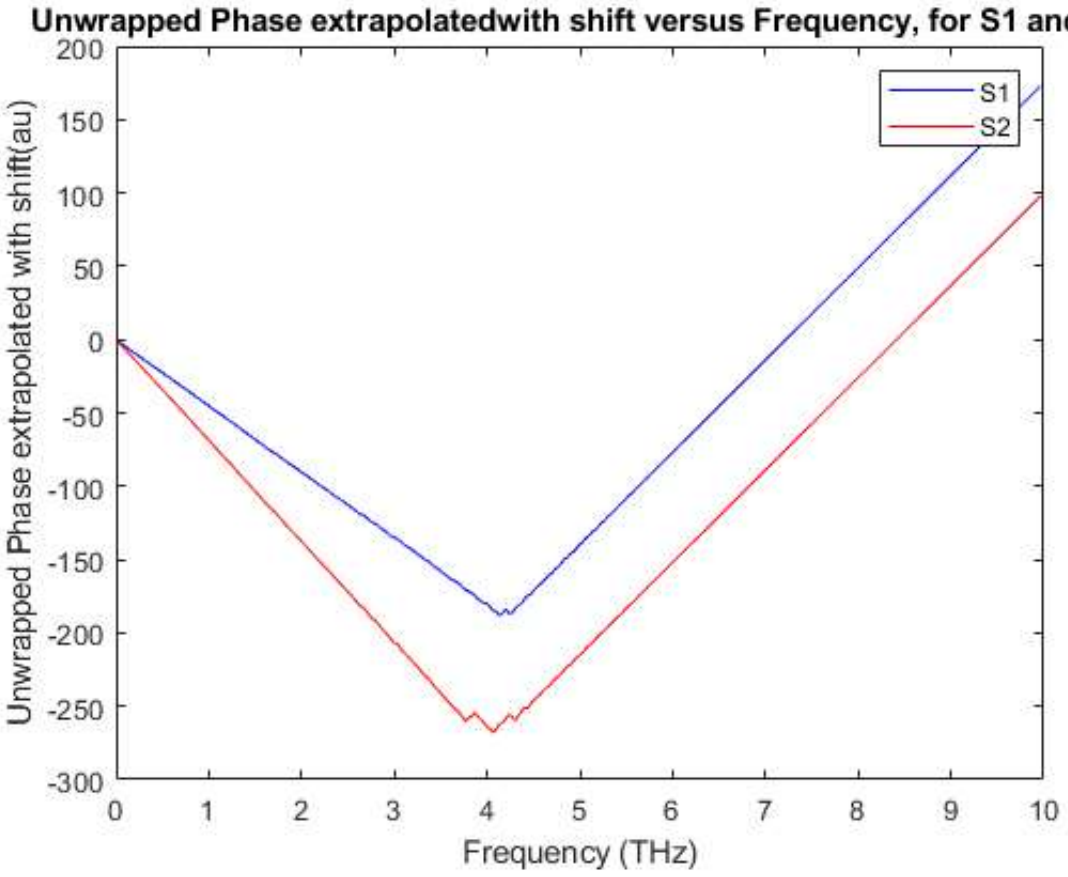
Unwrapped Phase extrapolatedwith shift versus Frequency, for S1 and S2
S1
S2
Unwrapped Phase extrapolated with shift(au)
Frequency (THz)
200
150
100
50
0
-50
-100
-150
-200
-250
-300
0
1
2
3
4
5
6
7
8
9
10

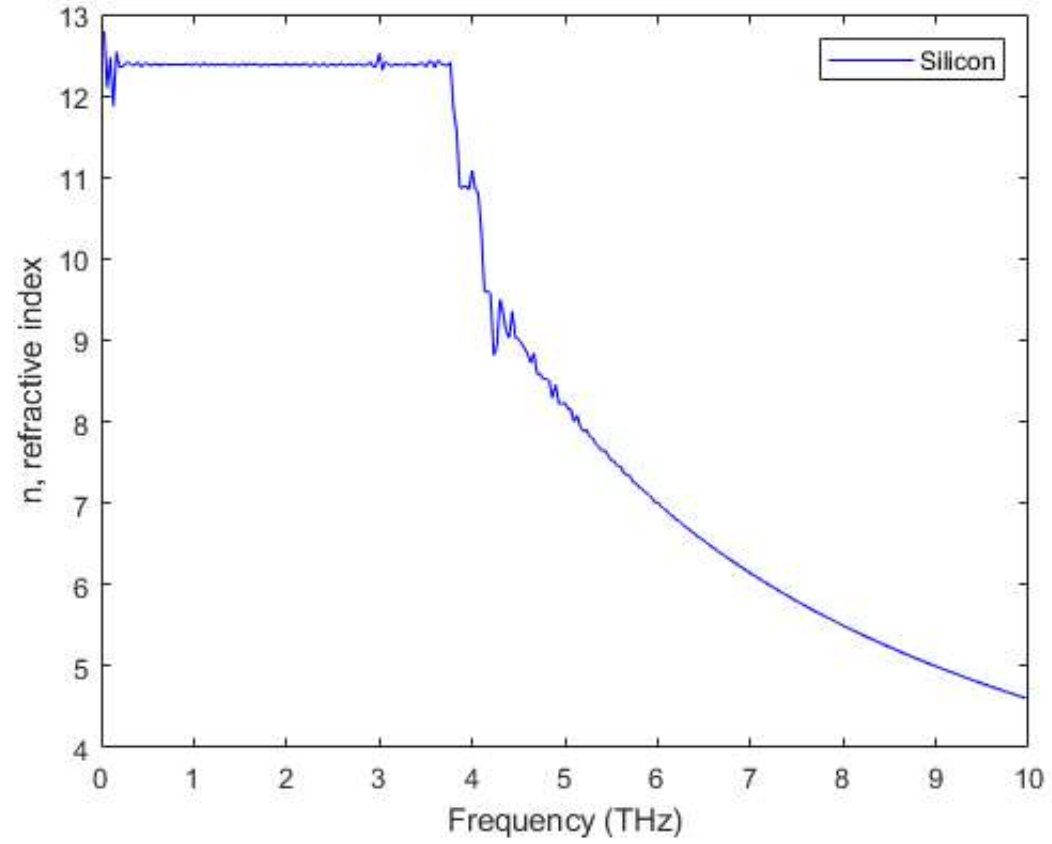
Silicon
n, refractive index
Frequency (THz)
13
12
11
10
9
8
7
6
5
4
0
1
2
3
4
5
6
7
8
9
10

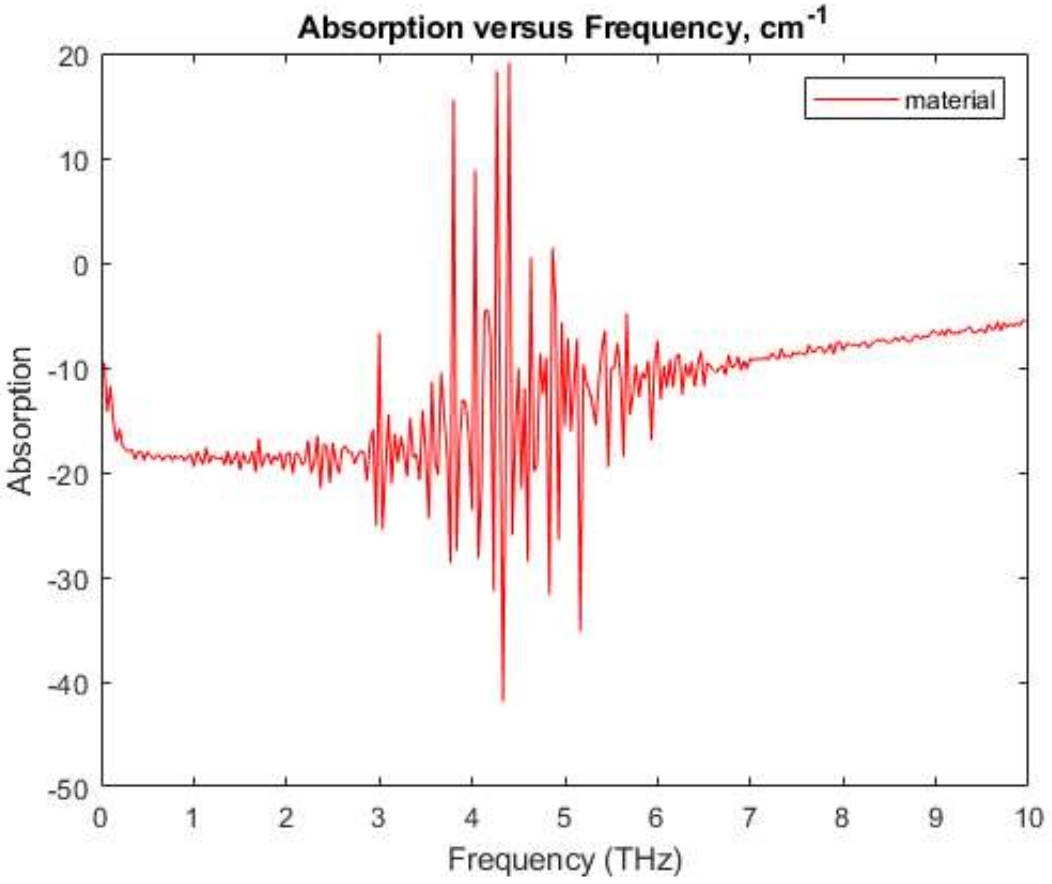
Absorption versus Frequency, cm-1
material
Absorption
Frequency (THz)
20
10
0
-10
-20
-30
-40
-50
0
1
2
3
4
5
6
7
8
9
10

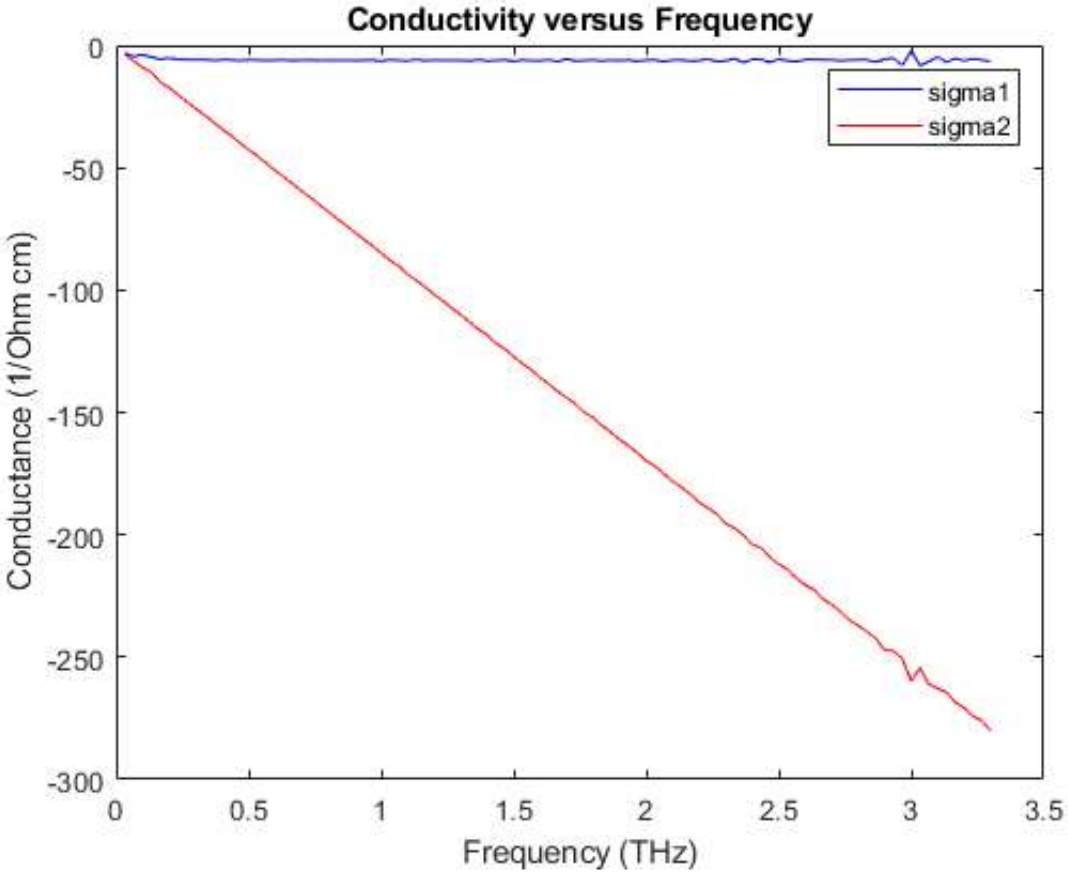

Published with MATLAB® R2018b